



TECHNISCHE
UNIVERSITÄT
WIEN
Vienna | Austria



DIPLOMARBEIT

A comparison of the biomechanical behaviour of simple artificial, composite, and 3D FDM printed human femoral bones

ausgeführt zum Zwecke der Erlangung des akademischen Grades einer Diplom-Ingenieurin
(Dipl.-Ing. oder DI), eingereicht an der TU Wien, Fakultät für Maschinenwesen und
Betriebswissenschaften,

Katharina Nägl

01225879

Migazziplatz 8-9/2/2

1120 Wien

unter der Leitung von

Univ.Prof. Dipl.-Ing. Dr. techn. Dieter H. Pahr
Institut für Leichtbau und Struktur-Biomechanik

.....

Datum

.....

Unterschrift

Abstract

Artificial bones established themselves in medicine to train and refine complicated and routine surgery procedures in orthopaedics, but they are also used to validate finite element analysis (FEA) models. The major advantage of such bones is that the necessity for human donor tissue is limited and the possibility of repeating experiments in a standardised way. The disadvantage of commercial artificial bones is the choice of geometry and structure, but also the relatively high costs. Consequently, there is a demand for a low-cost alternative product with comparable mechanical properties which allow for patient-specific applications.

In this work, four different artificial bones (Orthobone_Standard, Orthobone, SYNBONE[®] und SAWBONE[®]) from three different companies (3B Scientific GmbH, SYNBONE AG and A Pacific Research Company) were analysed and tested in terms of geometry, inner structure and mechanical properties. Initially, 3D surface scans and micro computed tomography (μ -CT) were performed to obtain a digital representation of the samples. Followed by a segmentation of the obtained μ -CT images to generate separate STL files of the cortex and spongiosa. The obtained files were then used to manufacture the bones using Fused Deposition Modelling (FDM). Subsequently the 3D printed samples were tested mechanically and compared to the performance of the purchased bones. The stiffness and ultimate force of the bones (artificial and printed) were of particular interest.

In this context it was determined that the bones of the printed sample group Orthobone_Standard, Orthobone and SYNBONE[®] showed higher stiffness and ultimate force compared with their artificial analogues. Only higher fracture loads were observed for commercial SAWBONE[®] if compared to 3D printed samples. This result was due to the fact, that the SAWBONE[®] consists of a composite material and for the FDM printed bone only polylactide (PLA) was used.

This thesis shows that it is possible to produce FDM printed analogues to the available artificial bones on the market. With them being not only cheaper and faster to manufacture, but also showing better or similar mechanical behaviour. In the future, printed bones will offer a wide range of clinical, patient specific applications.

Zusammenfassung

Künstliche Knochen finden immer häufiger Anwendung um diverse operative Techniken zu üben und zu verfeinern da sie die Notwendigkeit von Organspenden minimieren und die Möglichkeit bieten, Experimente standardisiert zu wiederholen. Der Nachteile von kommerziell erhältlichen Knochen ist eine limitierte Auswahl an Geometrie und Struktur bei teils sehr hohen Kosten. Aus diesem Grund besteht der Bedarf an möglichst kostengünstigen Ersatzprodukten die aber trotzdem vergleichbare mechanische Eigenschaften aufweisen und Patienten spezifisch hergestellt werden können.

Daher wurden vier künstliche Knochen (Orthobone_Standard, Orthobone, SYNBONE® und SAWBONE®) von drei unterschiedlichen Herstellern (3B Scientific GmbH, SYNBONE AG and A Pacific Research Company) hinsichtlich ihrer Geometrie und inneren Struktur untersucht, sowie mechanische Tests durchgeführt. Dies geschah anhand von 3D Oberflächenscans und der Aufnahme von Micro Computertomographie (μ -CT) Bilder. In weiterer Folge wurde eine Segmentierung der erhaltenen μ -CTs durchgeführt und sowohl die Kortex als auch die Spongiosa als STL Dateien extrahiert um die Knochen mittels Fused Deposition Modeling (FDM) 3D zu drucken. Die 3D gedruckten Femora wurden dann analog zu ihrem künstlichen Gegenstück mittels Kompressionstest mechanisch vermessen. Besonders von Interesse war dabei ihr Verhalten bezüglich Steifigkeit und maximal Kraft bis zum Versagen.

Dabei war festzustellen, dass alle gedruckten Knochen der Gruppe Orthobone_Standard, Orthobone und SYNBONE® höhere Steifigkeit und maximal Kraft aufwiesen als deren kommerziell erhältlichen Analoge. Nur bei der Variante SAWBONE® war die aufgewendete Kraft beim Bruch, sowie die Steifigkeit, höher im Vergleich zum 3D gedruckten Analog. Dies war darin geschuldet, dass es sich hierbei um einen Komposit-Knochen handelt und die Knochen welche mittels FDM hergestellt wurden nur aus Polymilchsäure (PLA) bestanden.

Diese Arbeit zeigt, dass es möglich ist künstliche Oberschenkelknochen mittels 3D Druck kostengünstig und schnell zu produzieren, welche in ihren mechanischen Eigenschaften kommerziell erhältlichen künstlichen Knochen ähneln. 3D gedruckte Knochen werden zukünftig großen Anklang in klinischen und Patienten-spezifischen Anwendungen finden.

Acknowledgements

At this point I would like to thank all who supported me throughout my years of study, especially...

... Univ.Prof. Dipl.-Ing. Dr. techn. Dieter H. Pahr, not only for his guidance throughout this master thesis, but also for always having an open ear if any problems or questions arise. Without him, I would have not been able to do this work at the Karl Landsteiner University.

... to Lukas Warnung, for his technical support in the lab

... to my parents, who always supported and encouraged me whatever I wanted to do and still continue to do.

... to my boyfriend Felix, who I knew since the beginning of my journey at the TU Vienna. Thanks for always supporting me and helping me out whenever I needed it.

...to all my friends, for moral support and listening to me during rough studying times and a special thanks to Theresia, who was the best studying partner I could have wished for.

Without you all, I wouldn't be at this point.

Table of Content

Abstract.....	I
Zusammenfassung.....	II
Acknowledgements	IV
List of Figures.....	VII
List of Tables.....	XI
List of Abbreviations and Symbols.....	XII
1 Introduction & Motivation	1
2 Femur.....	2
2.1 Anatomy ^{14, 16}	2
2.2 Mechanical Behaviour.....	3
2.3 Fracture Pattern	6
3 Artificial Bones	7
3.1 Composite Bones	7
3.2 Polyurethane based Bones	9
3.3 3D Printed Bones.....	10
3.4 Scope of biomedical application	11
4 Additive Manufacturing.....	13
4.1 Steps before printing	14
4.2 Techniques	15
4.2.1 Stereolithography (SLA)	15
4.2.2 Fused Deposition Modelling (FDM)	17
4.3 Materials used in FDM	18
4.4 Requirements and selected printing method and material.....	20
5 Imaging Techniques	21
5.1 Micro Computed Tomography (μ -CT) ⁹⁷	21
5.2 3D Surface Scan.....	24
6 Materials and Methodology	25
6.1 Materials.....	25
6.2 3D Surface Scans.....	26
6.3 Artificial Bone Alignment.....	28
6.4 μ -CT	29
6.5 Image Processing in Medtool 4.5.....	30

6.5.1 ORTHOBone_Standard (OBS) and ORTHOBone (OB)	30
6.5.2 SYNBONE® (SYN)	32
6.5.3 SAWBONE® (SAW).....	34
6.6 3D Printing	35
7.6.1 Extraction of the STL Files	35
6.6.2 Infill Density Estimation	36
6.6.2 Slicing and Printing Parameters.....	39
6.7 Embedding & Mechanical Testing.....	42
6.7.1 Embedding	42
6.7.2 Mechanical Testing	43
7 Results.....	48
7.1 ORTHOBone_Standard.....	48
7.2 ORTHOBone	53
7.3 SYNBONE®	56
7.4 SAWBONE®.....	61
7.5 Artificial Bones.....	65
7.6 Printed Bones.....	68
7.7 Comparison of Artificial and Printed Bones	71
8 Discussion.....	72
8.1 3D Surface Scan versus μ -CT	72
8.2 Artificial Bones.....	73
8.3 Printed Bones.....	75
8.4 Comparison of Artificial and Printed Bones	77
9 Conclusion.....	80
References	81
Appendix.....	88

List of Figures

Figure 1: Anatomy of Femur shown on the basis of an artificial bone 2

Figure 2: Anatomical (AA) and mechanical (MA) axis of the femur shown on the basis of an artificial femur..... 4

Figure 3: Common fracture region of the proximal femur. Fracture of the femoral neck are shown in section A. Section B shows fracture of the proximal femur and section C shows subtrochanteric fracture..... 6

Figure 4: SGFR Composite Bone. Femur, 4th Gen., Composite, 17 PCF Solid Foam Core, Medium (A Pacific Research Company, Vashon Island, Washington 98070, USA.) 8

Figure 5: PU based Bones. (A) ORTHObones Standard Femur, right (3B Scientific GmbH, 20459 Hamburg Germany) (B) ORTHObones Premium Right Femur (3B Scientific GmbH, 20459 Hamburg Germany) (C) Right Femur with distal canal opening (SYNBONE AG, 7205 Zizers, Switzerland)..... 9

Figure 6: Steps in Additive Manufacturing shown on the basis of an 30x30x30 mm cube with gyroid as infill pattern 14

Figure 7: Slicing pattern available in Prusa shown on the basis of a cube with an infill density of 10%. (A) straight lines (B) grid (C) triangles (D) stars. (E) cubic (F) linear (G) concentric (H) honey comb. (I) 3D honey comb (J) gyroid (K) Hilbert-curve. (L) Archimedes arch (M) Archimedes spiral..... 15

Figure 8: Schematic process of SLA 16

Figure 9: Schematic process of FDM 17

Figure 10: μ -CT from Bruker Corporation (40 Manning Road, Billerica, MA 01821), model Bruker Skyscan 1173®..... 21

Figure 11: schematic principle of μ -CT measurement..... 22

Figure 12: Beam-Hardening artefact shown on the basis of the reconstructed μ -CT of a purchased artificial bone 23

Figure 13: Ring Artefacts shown on the basis of a reconstructed μ -CT scan of a purchased artificial bone 23

Figure 14: schematic sketch of the triangulation working principle of a 3D surface scanner. 24

Figure 15: Artificial Bones: (A) OB and OBS (B) SYN, and (C) SAW 26

Figure 16: Illustration of the exported STL files. (A) OBS (B) SYN and (C) SAW 27

Figure 17: Workflow of the Alignment of the artificial bone. (A) Fixiation of Distal Epiphysis (B) Laser Alignment of Epicondyles lateralis and Epicondyles medialis (C) horizontal Laser

Alignment (D) Alignment of the mechanical axis of the femur (E) marked cutting line (F) final cropped femur.....	29
Figure 18: (A) Special holder for bones in the μ -CT (B) special holder and sample placed in the μ -CT chamber.....	29
Figure 19: Steps of Segmentation in terms of Midplanes of ORTHOBone. (A) rescaled image (B) usage of -arith filter (C) usage of -morphk opening filter (D) usage of -morphk closing filter (E) Segmentation in Slicer 4.11.20200930 [®] (F) fill pores filter (G) usage of -arith filter to subtract cortex from bone to get the spongiosa (H) inverted spongiosa	32
Figure 20: Steps of Segmentation in terms of Midplanes of SYN. (A) rescaled image (B) usage of -arith filter (C) usage of -morphk opening filter (D) first manually segmentation in 3D Slicer 4.11.20200930 [®] (E) final segmentation of the cortex (F) fill por filter (G) usage of -arith filter to subtract cortex from bone to get the spongiosa (H) inverted spongiosa	33
Figure 21: Steps of segmentation on terms of Midplanes of SAW. (A) rescaled image (B) usage of -arith filter (C) binary mask of the cortex (D) manually segmented cortex (E) fill pores filter (F) usage of the -arith filter to subtract the cortex from the whole bone to obtain the spongiosa (G) inverted spongiosa	35
Figure 22: schematic figure of the obtained spongiosa (gyroid pattern, 5% infill) and cortex (linear pattern, 100% infill) of the artificial bones. (A) for OBS and OB (B) for SYN (C) for SAW.....	36
Figure 23: Cortex and Spongiosa shown of the different artificial bones. (A) OBS (B) OB (C) SYN (D) SAW.....	36
Figure 24: Compression test of the milled cube of infill foam to represent the artificial spongiosa.....	37
Figure 25: /A) Power law of previous work ¹⁰² showing the calculated Power law and experimental curves from cubial PLA samples with varying Gyroid infill. (B) sample_z (tested orthogonally to the printing direction) and sample_xy (tested in printing direction) both with a gyroid infill pattern and 10% infill density	38
Figure 26: Printing plate of PrusaSlicer 2.1.1 [®] with sliced bone samples.....	39
Figure 27: Original Prusa i3 MK3 [®] printing process for the PLA femur	41
Figure 28: Schematic Embedding process. (A) embedding of the distal end of the printed bone (B) embedding of the Caput femoris (C) final embedded bone, ready for compression test.....	42
Figure 29: Set-Up for compression test of the printed and artificial bones in marked STANCE position (20°).....	43

Figure 30: Laser Alignment of the Caput femoris for the right position for compression test	44
Figure 31: Correction of the obtained compression curve	45
Figure 32: Correction of the SAW_1K force-displacement curve	46
Figure 33: schematic force-displacement curve of OBS_6P to show how the characteristic values of FU_{lt} and S were determined in the range of 0 to 2 mm displacement	46
Figure 34: Segmenting of OBS (A) segmented spongiosa (B) segmented cortex (c) midplane without segmented region (D) segmented spongiosa and cortex shown on the original midplane output in different direction in space	48
Figure 35: Comparison of the obtained STL files of the 3D surface scan (grey) and μ -CT (green). (A) Alignment of the two bones (B) Deviations greater than 0.5mm denoted by the red area and pins for selection of points in this area	49
Figure 36: Infill show of OBS. (A) printing file in Prusa Slicer® (B) printed bone	50
Figure 37: Force-Displacement curves of the ORTHOBone_Standard (OBS), printed (P) and artificial (K) samples	51
Figure 38: Fracture Pattern of OBS shown with OBS_6P	52
Figure 39: Printed OBS sample (A) before (B) after compression test	52
Figure 40: Infill show of OB. (A) printing file in Prusa Slicer® (B) printed bone	53
Figure 41: Force-Displacement curves of the ORTHOBone (OB), printed (P) and artificial (K) samples	54
Figure 42: Fracture Pattern of OB shown with OB_4P	55
Figure 43: Printed OB sample (A) before (B) after compression test	55
Figure 44: Segmenting of SYN (A) segmented spongiosa (B) segmented cortex (c) midplane without segmented region (D) segmented spongiosa and cortex shown on the original midplane output in different direction in space	56
Figure 45: Comparison of the obtained STL files of the 3D surface scan (grey) and μ -CT (green). (A) Alignment of the two bones (B) Deviations greater than 0.5mm denoted by the red area and pins for selection of points in this area	57
Figure 46: Printing of SYNBONE® (A) exported g-code (B) printed bone	58
Figure 47: Force-Displacement curves of the SYNBONE® (SYN), printed (P), and artificial (K) samples	59
Figure 48: Fracture pattern of SYNBONE® shown with SYN_3P	60
Figure 49: Printed SYN sample (A) before (B) after compression test	60

Figure 50: Segmenting of SAW (A) segmented spongiosa (B) segmented cortex (C) midplane without segmented region (D) segmented spongiosa and cortex shown on the original midplane output in different direction in space	61
Figure 51: Comparison of the obtained STL files of the 3D surface scan (grey) and μ -CT (green). (A) Alignment of the two bones(B) Deviations greater than 0.5mm denoted by the red area and pins for selection of points in this area.....	62
Figure 52: Printing of SAW (A) exported g-code (B) printed bone.....	62
Figure 53: Force-Displacement curves of the SAWBONE [®] (SAW), printed (P), and artificial (K) samples	63
Figure 54: Printed SAW sample (A) before (B) after compression test	64
Figure 55: Average Force-Displacement curves of the artificial (K) bones and their standard deviation. (OBS...ORTHOBone_Standard, OB...ORTHOBone, SYN...SYNBONE [®] , SAW...SAWBONE [®]).....	65
Figure 56: Ultimate Force of the artificial bones. (OBS...ORTHOBone_Standard, OB...ORTHOBone, SYN...SYNBONE [®] , SAW...SAWBONE [®])	66
Figure 57: Stiffness of the artificial bones. (OBS...ORTHOBone_Standard, OB...ORTHOBone, SYN...SYNBONE [®] , SAW...SAWBONE [®])	66
Figure 58: Fracture pattern of artificial bones. (A) OBS (B) OB (C) SYN (D) SAW	67
Figure 59: Average Force-Displacement curves of the printed bones. (OBS...ORTHOBone_Standard, OB...ORTHOBone, SYN...SYNBONE [®] , SAW...SAWBONE [®]) and their standard deviation.....	68
Figure 60: Ultimate Force of the printed bones. (OBS...ORTHOBone_Standard, OB...ORTHOBone, SYN...SYNBONE [®] , SAW...SAWBONE [®])	69
Figure 61: Stiffness of the printed bones. (OBS...ORTHOBone_Standard, OB...ORTHOBone, SYN...SYNBONE [®] , SAW...SAWBONE [®])	69
Figure 62: Fracture pattern of artificial bones. (A) OBS (B) OB (C) SAW (D) SYN.....	70
Figure 63: Comparison of the ultimate force of the printed (P) and artificial (K) bones. (OBS...ORTHOBone_Standard, OB...ORTHOBone, SYN...SYNBONE [®] , SAW...SAWBONE [®])	71
Figure 64: Comparison of Stiffness of the printed (P) and artificial (K) bones. (OBS...ORTHOBone_Standard, OB...ORTHOBone, SYN...SYNBONE [®] , SAW...SAWBONE [®])	71
Figure 65: Measurement protocol OBS_1K	88
Figure 66: Measurement protocol SYN_1K	89
Figure 67: Measurement protocol SAW.....	89

List of Tables

Table 1: Determination of the infill density by performing compression tests of cubes.....	37
Table 2: Common printing settings for cortex and spongiosa (EW stands for extrusion width)	40
Table 3: Determined material characteristics for OBS	51
Table 4: Determined material characteristics for OB.....	54
Table 5: Determined material characteristics of SYNBONE®	59
Table 6: Determined material characteristics of SAWBONE®	63

List of Abbreviations and Symbols

AA...Anatomical axis	S... Stiffness
ABS...Acrylonitrile butadiene styrene	SAW... SAWBONE®
AM... Additive Manufacturing	SGFR... short-glass-fibre reinforced
CAD... Computer aided design	SLA... Stereolithography
d... distance	SYN... SYNBONE®
E_{Bone} ... E -modulus of Bone	μ ... linear attenuation coefficient
EW...Extrusion width	μ -CT... Micro Computed Tomography
F_{ult} ...ultimate Force	ΔF ... change in Force
FDM... Fused Deposition Modelling	Δu ... change in Displacement
FEA... Finite Element Analysis	_K... artificial
FFR... fibre glass fabric reinforced	_P... printed
I_B ... Beam intensity	
I_0 ...initial Beam intensity	
k... Power law factor	
MA... mechanical axis	
MRI... Magnet Resonance Imaging	
OB... ORTHOBone	
OBS...ORTHOBone_Standard	
OP... osteoporotic bone	
PCL... Polycaprolactone	
PET...Polyethylene Terephthalate	
PET-A... amorphous PET	
PET-C... crystalline PET	
PET-G... glycol modified PET	
PLA... Polylactide	
PU... Polyurethane	
QCT... Quantitative Computed Tomography	

1 Introduction & Motivation

Artificial bones are designed to mimic real bone in their mechanical behaviour and serve as surrogates for human bones. The advantage of such bones is to better standardize and understand diverse medical conditions without harming a living organism. With regard to human femur, synthetic long bones have successfully been assessed in studies concerning intramedullary and extramedullary fractures¹⁻³ and also hip resurfacing arthroplasty⁴⁻⁵. They are also used to evaluate periprosthetic fracture fixation in the presence of total joint arthroplasty⁶⁻⁹. Another use of these surrogate bones is the comparison of the mechanical performance to the one of human femurs to gain more knowledge on the biomechanics of femurs and risk factors.¹⁰⁻¹²

Artificial bones come in a broad range of quality starting from polyurethane foam models which are relatively inexpensive (~12-40 €) and ending with highly sophisticated composite materials with prices of up to a few hundred euros. Most of these artificial bones have a similar geometry and the thickness of the cortex is designed to match the desired mechanical properties and capabilities of manufactures. However, it is not always known which natural bone geometry and densities are resembled in commercially available artificial bones.

The goal of this master thesis is to 3D print bones using fused deposition modelling (FDM) for rapid prototyping, which is not only cost efficient but also faster than other methods¹³ and, therefore, allows the fast manufacturing of samples directly in the lab. The printed bones will be based on the geometry and infill properties of four different artificial bones and comparison with their artificial analogues will be performed. Especially their performance concerning stiffness and resulting ultimate force are of interest in this study. In the future, such printed bones can be individualised according to patient data and thus offer a wide variety of clinical applications.

2 Femur

The human body roughly consists of 206 bones, which are building up the human locomotor system together with cartilage, tendons and joints.¹⁴ Basic building blocks are so called osteocytes, of which up to 42 billion are present in an adult human body.¹⁵ They build up bones from the smallest, tiniest ones in the ear (malleus, incus and stapes) up to the largest, the Femur.^{14, 16}

2.1 Anatomy^{14, 16}

The femur is a long hollow bone and its structure can be broken down into the following areas; the *corpus femoris*, the *collum femoris* and the *extremitas proximalis* and *distalis* as shown in Figure 1 below. Noticeable are structures like the *Trochanter major* and *minor*, which are unmistakable recognised on femurs. Not shown in Figure 1 is the *Linea aspera*, which develops along *corpus femoris*. Since Figure 1 represents the anatomy of a femur on the basis of an artificial bone, the *Linea intertrochanterica* is also missing. The latter would form the border between *collum femoris* and *corpus femoris* on the front of the femur. The *condylus lateralis* and *medialis* build up the distal end and are interconnected through the *facies patellaris*.

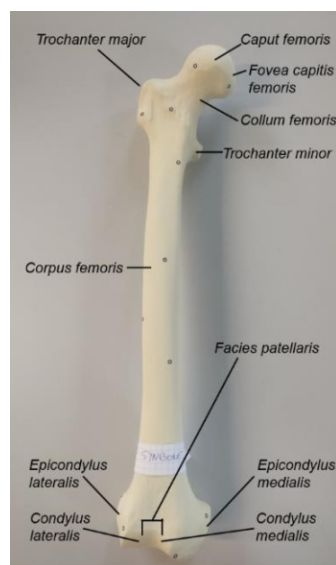


Figure 1: Anatomy of Femur shown on the basis of an artificial bone

Only the landmarks on the surface of the femur are shown in Figure 1. On a macroscopical level the femur could be divided into a dense layer, called *corticalis* or *cortex* and a spongiosa of varying density.¹⁷ The spongiosa is built of *trabecula* varying in thickness around $194 \pm 33 \mu\text{m}$ ¹⁸. Elke *et al.* analysed CT data of the proximal end of the femur and found three different sections: the epiphysis, the epiphyseal scar, and the metaphysis all with different cancellous bone pattern. In the epiphysis the trabecular bone seem to be reticulate, while the metaphysis showed a more longitudinally orientation.¹⁹ This trabecular bone “mushroomed” from the femoral head perpendicular to the thin cortical shell as found out by Stiehl *et al.*²⁰. The density of the spongiosa changes with age and varied with sub-regions of the proximal femur and therefore affecting the mechanical behaviour of the bone.²¹

2.2 Mechanical Behaviour

Stiehl *et al.* also found that the spongiosa of the main compressive stunt connecting the femoral head to the neck had similar bone density compared to cortical structures present in the femur.²⁰

Von Meyer *et al.* already stated that the trabecular architecture follows the direction of tensile and principle compressive stresses.²²⁻²³ These tensile and compressive lines are so called trajectories and are represented in Von Meyers *et al.* and Culmann *et al.* famous sketch²³, but also in modern anatomy textbooks.¹⁴

These findings inspired Wolff *et al.*²⁴ to work on the formation and degradation of bone. They postulated that bone will be laid down where it is needed (due to acting load) and removed where it is not needed²⁴, better known as Wolff’s law. If the whole central part of the cancellous structure of the proximal femur would be removed, the bone strength for impact loading would approximately decrease by about 50%.²⁵

The lines of compressive and tensile stresses do not only follow the internal load distribution but are also represented by the mechanical axis of the femur as shown in Figure 2. There are two possible definitions for the anatomical axis of the femur

(Figure 2 AA); the connection between femoral shaft centre and the mid-shaft medial-to-lateral width is one possibility, the other one is the axis connecting femoral shaft centre to a point 10 cm above knee joint.²⁶ Concerning load distribution across the lower extremity the mechanical axis is more relevant. This axis ranges from the centre of femoral head to the centre of the ankle joint, which is approximately declined 3° to the anatomical axis.²⁷ The angle between the anatomical axis and the mechanical axis, which runs from the femoral head to the intercondylar notch, considering only the femur (Figure 2 MA) is about 5 to 7° .²⁷ Especially in the total knee arthroplasty the alignment of anatomical and mechanical axis is of great interest, since it can vary widely based on pelvic width and height of the patient.²⁸



Figure 2: Anatomical (AA) and mechanical (MA) axis of the femur shown on the basis of an artificial femur

Not only the angle between mechanical and anatomical axis plays a role in the load configuration during daily life activities, also the angle in which the load is applied on the femoral head is decisive. The Julius Wolff Institute at the Berlin Charité conducted a study concerning loads acting in hip implants to gain knowledge on the

angle and peak forces acting on the femur.²⁹ They found out that peak forces and acting angles are not only dependent on the patients but also on the activity they are performing.²⁹ During the stance phase (one leg stand) the average peak value of the force was 2077 N with the angle varying between 8 to 21° in the frontal plane.²⁹

During normal walking with an average speed of 4 km/h the hip joint gets loaded with 238% of the person's bodyweight.³⁰ Almost the same percentage is reached when standing on one leg (stance phase in the gait cycle).³⁰ Many biomechanical researches simulating stance phase are found in literature.³¹⁻³⁸ only varying in the chosen angle of applied load.

Dall'Ara *et al.* for example used the mechanical testing in stance position to "compare the ability of BMD and BMC of different proximal femoral regions in predicting femoral mechanical properties".³² By testing 36 specimen in stance position (20°) an average failure force of 8709 ± 2929 N was obtained for the proximal femur.³² Dall'Ara *et al.* also used the same test set up to validate a nonlinear quantitative computed tomography (QCT) based finite element model.³¹

Bousson *et al.* tried to use QCT to find a relationship between geometric and densitometric parameters to predict the strength of a femur.³³ Choosing an angle of 25° for representing the stance phase. The average ultimate force reached, using 28 specimen, was 6.0 ± 2.4 kN.³³ In the study of Cody *et al.* also an angle of 25° was used, but the reached force until failure was 3kN higher (9.9 ± 3.2 kN).³⁴

Comparable results of the ultimate force of femurs were obtained by Kulka *et al.* with 8.5 ± 2.4 kN³⁶ and Link *et al.* with 8.9 kN³⁷ despite choosing a different angle of load application (12° and 11°).

Besides the choice of simulating stance phase during mechanical tests, another configuration is widely used in literature, the so called side configuration.^{31-32 39-44} This is often done to simulate or gain more knowledge on the forces acting on the femur during a fall before fracture occurs.

2.3 Fracture Pattern

A fracture only occurs when the acting force is higher than what the bone can withstand. This is often the case when falling directly on the side of the hip.⁴⁵⁻⁴⁷ The side fall on the greater trochanter represents 98% of the hip fractures and can be retraced by the formation of a hematoma on the fracture site⁴⁸. This means only 2% of the fractures can be traced back to a spontaneous trauma.⁴⁸ The risk of fracture is also influenced by the density of the bone⁴⁵, level of recent physical activity and body mass index.⁴⁷ Even in younger people a direct fall to the side of the hip can cause a high impact fracture of the femur.⁴⁶

Daescu *et al.* tested human femurs to determine the loads acting on the bone during a side fall to validate a finite element analysis (FEA) model predicting proximal femur stiffness and loads during a side fall. It was found that the frozen femurs could withstand 4.0 ± 1.6 kN before fracture occurred.⁴¹ This finding correlates with the study of Cheng *et al.* who also found an average ultimate force of 4.0 ± 1.6 kN using 70 femora.⁴⁰ These studies show that the human femur withstand only half of the load during a side fall compared to the loading situation in stance position.³¹⁻³⁴

There are mainly 3 different section where fractures occur; the femoral neck fractures shown in Figure 3 section A, the fracture of the proximal femur including intertrochanteric fractures (section B) and the fracturing of the subtrochanteric femur in section C.⁴⁹ In the elderly the two most common fractures occur in the femoral neck and intertrochanteric, where the latter one results in longer hospital stays.⁵⁰ Besides fractures in these sections, fractures of the femoral head (above section A) and fracture of the femoral shaft (under section C) can be classified.^{49, 51}

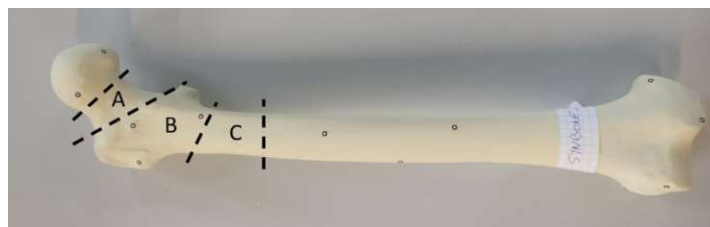


Figure 3: Common fracture region of the proximal femur. Fracture of the femoral neck are shown in section A. Section B shows fracture of the proximal femur and section C shows subtrochanteric fracture.

3 Artificial Bones

Dimitriou *et al.* found variations of the exact geometry of the femur in human beings.⁵² This asymmetry may complicate operations like hip reconstruction or dealing with fractures. Therefore, it is advantageous to train and test certain operation techniques in advance^{1, 3-4, 6-8, 53-55}. Usually is not possible in living human beings due to ethical concerns. An alternative is, donor tissue, however, is not only difficult to get, it also involves a large amount of preparation processes before the bones can be tested. The entire soft tissue has to be removed and the surface has to be cleaned properly. Despite that, the bone can only be tested once, concerning failure test or different implants. Another issue with donor bones is their variability due to age differences and diseases, which makes it impossible to reproduce results. However, human bones simulate the in-vivo situation the best. A promising alternative to donor tissue is the usage of artificial bones. Cristofolini *et al.* already approved in 1996 that the mechanical qualities of artificial bones lay within the range of cadaveric specimen.¹⁰ However, the materials used for artificial bones are not comparable to the in-vivo situation, but due to their defined properties, results become reproducible. They are easy to purchase and depending on the money spend, different materials are available but they are restricted to a certain geometry.

3.1 Composite Bones

Composite bones are the best in terms of mechanical performance, but also the most expensive. They evolved with time from the first mechanically realistic replicate consisting of an epoxy reinforced cortical shell with glass fibres to a fibre glass fabric reinforced (FFR) composite.¹¹ The manufacturing of these type of composite bone needed manual craftsmanship and, therefore, lacked in anatomical details and uniformity in mechanical properties.¹¹ Further improvements of the composite materials were made by Pacific Research Company by using short-glass-fibre reinforced (SGFR) epoxy instead of FFR, allowing for a more detailed model.¹¹ Heiner *et al.* tested the older (FFR) vs. the new (SGFR) bones in terms of stiffness under bending in torsional and compressive loads. It was found that the SGFR composite bones were less stiff than the FFR but had less variability in the

mechanical performance and while still being in the range of natural bone.^{11, 56} Furthermore the alignment of the bone in the testing machine was decisive.¹¹

The bones of Pacific Research Company evolved from generation to generation. The current fourth generation SGFR was introduced due to the third generation being prone to crack formation.⁵⁷ Chong *et al.* found out that the newer generation had an increased fracture toughness by 48% and resembles the natural bone properties even more than the third-generation composite bone.⁵⁷ They also showed that the fourth generation bone performed more realistic in high activity loading than the previous one.⁵⁸

A big advantage of these fourth generation composite bones of Pacific Research Company is the low inter-specimen variability concerning mechanical properties and they are therefore ideal for biomechanical analyses.⁵⁹

An example of such a fourth generation SGFR composite femur is shown in Figure 4 below. The composite bone is differentiable from the polyurethane bones (shown in Figure 4) on the basis of its colour. It is dark brown compared to the light brown/yellow appearance of the PU bones. At this point the relatively high price of around 200 € of these bones has to be mentioned. On the other hand, polyurethane bones can be purchased for around 12 to 40 €, depending on the quality.



Figure 4: SGFR Composite Bone. Femur, 4th Gen., Composite, 17 PCF Solid Foam Core, Medium (A Pacific Research Company, Vashon Island, Washington 98070, USA.)

3.2 Polyurethane based Bones

A cheap alternative to composite bones are polyurethane based artificial bones. Currently companies such as 3B Scientific GmbH (Ludwig-Erhard-Str. 20, 20459 Hamburg Germany), SYNBONE AG (Tardisstrasse 199, 7205 Zizers, Switzerland) and A Pacific Research Company (10221 SW 188th Street, PO Box 409, Vashon Island, Washington 98070, USA.) are producing PU based bone surrogates. Three bones and their foam representing the spongiosa are shown in Figure 5 below. It shows three commercially available polyurethane based femora (Figure 5 A-C) and a cross-sectional cut to show off the denser part (representing the cortex) and the porous foam (representing the spongiosa). Furthermore, the medullary canal is visible, which has a cylindrical design and is found throughout the whole shaft and varies from real human femora.



Figure 5: PU based Bones. (A) ORTHObones Standard Femur, right (3B Scientific GmbH, 20459 Hamburg Germany) (B) ORTHObones Premium Right Femur (3B Scientific GmbH, 20459 Hamburg Germany) (C) Right Femur with distal canal opening (SYNBONE AG, 7205 Zizers, Switzerland)

Similar to the composite bones, the polyurethane based bones did evolve over time. Hein *et al.* were the first one to use a polyurethane (PU) foam as a substitute for trabecular bone.⁶⁰ Subsequently, Szivek *et al.* manufactured two different polyurethane foams by varying the ratio of resin and isocyanate and compressed them to evaluate their respective *E*-modules.⁶¹ Furthermore the formation of bubbles during an exotherm reaction in the polyurethane was observed, resulting in different porosities. Also, the ratio of resin to isocyanate did influence the bubble diameter and therefore the porosity of the foam.⁶² As a result of this study, Szivek *et al.* claimed that the stress-strain curves were similar to curves of trabecular bone and exhibited less variation in mechanical properties than natural bone.⁶¹ Thompson *et al.* used rigid cellular foam of four different densities to test their shear

and compressive behaviour. They found out that their compressive yield strain was almost constant, while shear stresses did vary and concluded that PU foams are only efficient for simulating the elastic behaviour of cancellous bone but not the failure properties.⁶³ PU foam furthermore were used to simulate osteoporotic bone (OP), as done by Patel *et al.*⁶⁴ In this study, compression tests were performed on cylindrical PU core samples varying in size and density. It was concluded, that one foam density qualifies to simulate OP bone when compression properties are of interest and not energy dissipation. A big advantage of polyurethane is that resin and isocyanate can be cast in different shapes and sizes.⁶¹

3.3 3D Printed Bones

As already discussed above, Dimitriou *et al.* found out that the shape of human femur can vary in geometry.⁵² This might be true for various bones in the human body. For this reason, it is useful to have a tool which is able to show these variations accurately. With 3D printing it is possible to manufacture such models accurately, cheap and quickly. Even with a quantity of one. This was shown for example by Carew *et al.* by printing different skulls to show the efficiency of 3D printing for forensic evidences.⁶⁵ The conclusion of this study was that the printing of these samples only varied in an acceptable deviation for them to act as demonstrative evidence in court. Also Bartikian *et al.* printed different skull bones, such as the *occipital*, *temporal* and *sphenoid* with good anatomical details.⁶⁶ Since body donors are limited, such 3D printed models present a good alternative to represent the structure of bones. O'Reilly *et al.* used the CT-Data of patients to obtain an anatomical model of the lower limb for 3D printing for education purposes.⁶⁷ Also AbouHashem *et al.* manufactured bones through 3D printing.⁶⁸ They used existing surface scan data and skeletal collections to fabricate these bones for educational purposes. Literature research shows that one of the main applications of 3D printed bones at the moment is anatomical education. First steps in studying the biomechanical behaviour of such FDM printed bones were recently made at the Institute of Lightweight and Structural Biomechanics (ILSB) at TU Vienna by printing human femora based on CT-Data of real bones and subsequently performing compression tests simulating stance phase during a gait cycle.⁶⁹

3.4 Scope of biomedical application

All these artificial bones mentioned in the chapters 3.1 and 3.2 can be used in various applications. These range from establishing research models using artificial bones to validating FEA results for testing different implant systems. Even training courses for surgeons could be performed using such bones to improve their skills. In all mentioned studies composite bones were used to simulate human bone. Depending on the quality of the artificial bone the price of these bones vary significantly.

An approach to be independent of human tissue studies is FEA, but these models need to be validated which is often done with artificial bones.^{1, 12, 31} Besides the orthopaedic usage of artificial bones, the FEA method is used to predict mechanical behaviour of bones in general.^{12, 31, 70} Papini *et al.* compared the mechanical behaviour of human femur with artificial bones and FEA by testing the axial and torsional stiffness in mid stance orientation.¹² These stiffnesses were also part of an investigation done by Zdero *et al.*, who studied the influence on applying different load rates on synthetic femurs.⁷⁰

Such FEA models can also be useful to understand the influence of fixation techniques after fractures. Cheung *et al.* implemented a finite element model which described the strains on the surface of a femur treated with intramedullary nails due to fracture of the femur and validated it on the basis of synthetic femurs.¹ In the same manner Bougherara *et al.* proceeded.³ For orthopaedic surgeons' fracture of the femoral shaft after a total hip arthroplasty is a key concern, which is why Shah *et al.* tested three different bone plate repair methods on synthetic femurs, simulated stance phase during walking and compared it with a developed FEA model.⁵³

Besides the validation of FEA models artificial bones are used for pre-clinical studies. For example Dennis *et al.* studied different fixation techniques used in periprosthetic femoral shaft fixation on synthetic femurs to see which provides the best fixation during different physiological loading modes.⁶ This study suggested that the use of plate constructs with different screws are more stable during daily activities. Furthermore, Zdero *et al.* tested the performance of fixation techniques simulating midshaft fractures without a bone gap and compared them with the stiffness,

lateral bending and torsion before the fixation on the artificial bone was done.⁸ The highest stiffness was reached with a construct of nonlocking plates in combination with an allograft strut. Stevens *et al.* used synthetic femurs to study the influence of three different wiring techniques for cerclage-plating and what effect the different wires and the plate insert had on the mechanical behaviour in cyclic loading.⁷ This study showed an improvement of the stability and fixation strength when the insert technique was used. Also, the correct alignment of the femoral component in relative *varus* or relative *valgus* in hip resurfacing plays an important role and was tested by Davis *et al.* on the basis of composite artificial femurs.⁵

From great interest are studies which investigate the interaction between the bone-implant surface. Grant *et al.* for example investigated the friction coefficients between synthetic composite bones and uncemented implants, which are critical for proper load transfer.⁵⁴ It was shown that the artificial bones used for pre-clinical implant testing are sensitive to their lubrication condition and surface finishing. Also, the torque during the insertion of a screw into a bone is from great interest. Surgeons have to apply torque and have to be cautious when to stop. Therefore, a study concerning the stopping and stripping torque for cortical and cancellous bone was performed by Tsuji *et al.* testing a wide range of bone densities represented by SAWBONE[®] blocks varying in density.⁷¹ Often screws used to fix a complicated fracture are removed after a certain time, therefore it is important to know the pull-out forces and shear stresses acting on the bone and screws. For that reason, Zdero *et al.* used fourth generation composite bones to study cancellous bone screw purchase by testing the pull-out force, shear stress and energy during the removal of the screw inserted.⁷² A comparison between the bone screw purchase between natural bone, third and fourth generational composite bones was also done. It was shown that the use of fourth generation composite bone performed closer to natural bone than third generation did.⁵⁵

4 Additive Manufacturing

Additive manufacturing (AM) is per definition a method which joins different volume elements together layer by layer to form a new geometry.^{73 74} It can be categorized in seven different process categories, namely⁷⁴:

- Binder jetting
- Direct energy deposition
- Material extrusion
- Material jetting
- Powder bed fusion
- Sheet lamination
- Vat photopolymerization

Thompson *et al.* focused on the usage of AM in combination with computed tomography (CT) in their review article, stating that AM is advantageous for “low volume production as no additional tooling is required when producing new parts”⁷⁵

AM has been used not only for printing anatomical models as done by Igami *et al.* by printing a three dimensional model of a liver and injecting colour to visualise hepatic veins⁷⁶, but also for surgical guidance⁷⁷⁻⁸⁰ before performing a complicated surgery. For this purpose, Kenngott *et al.* printed a whole torso and filled it with silicone replica of the inner organs.⁷⁹

Thompson *et al.* also found in their literature research that Stereolithography (SLA) and Fused Deposition Modelling (FDM) are the main AM techniques used in medicine.^{75, 81} This two AM methods will be discussed in more detail in the following chapters.

4.1 Steps before printing

A few steps are necessary before a work piece can be printed (Figure 6). First, the geometry of the model is required, either this is achieved by computer aided design (CAD) or by an image technique followed by post processing procedures. This model has to be exported as an STL file (standard triangulation language or stereolithography) and imported into a slicing software, which cuts the model into layers for the subsequent printing process. Typically, the model is not printed as a solid block but only the outlines are while the space inside is either kept hollow or, to obtain a certain rigidity and strength, different so called infill patterns are used (Figure 7). The mechanical properties then depend on the infill density, the amount of space which is filled with material, and the infill pattern, the way how the inside is filled. Various infill-patterns are available and the ones provided by Prusa are depicted in Figure 7. When the model had been properly sliced the so called g.code has to be exported. This code basically tells the printer exactly where to move and deposit material to obtain the final physical model.⁸²

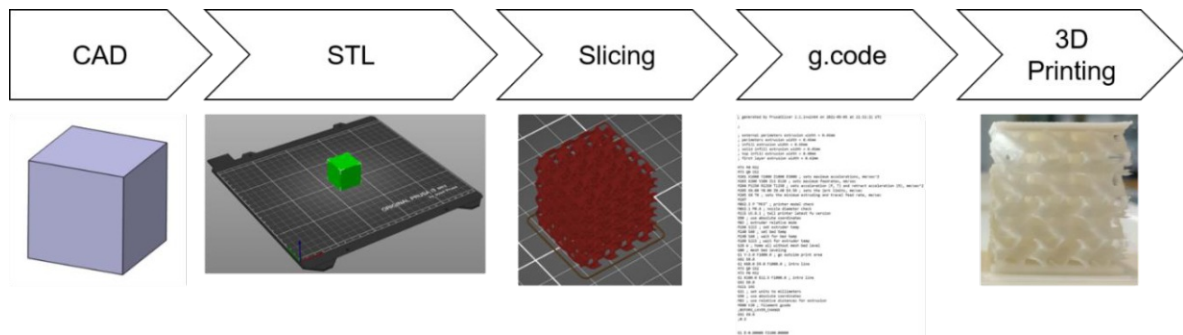


Figure 6: Steps in Additive Manufacturing shown on the basis of an 30x30x30 mm cube with gyroid as infill pattern

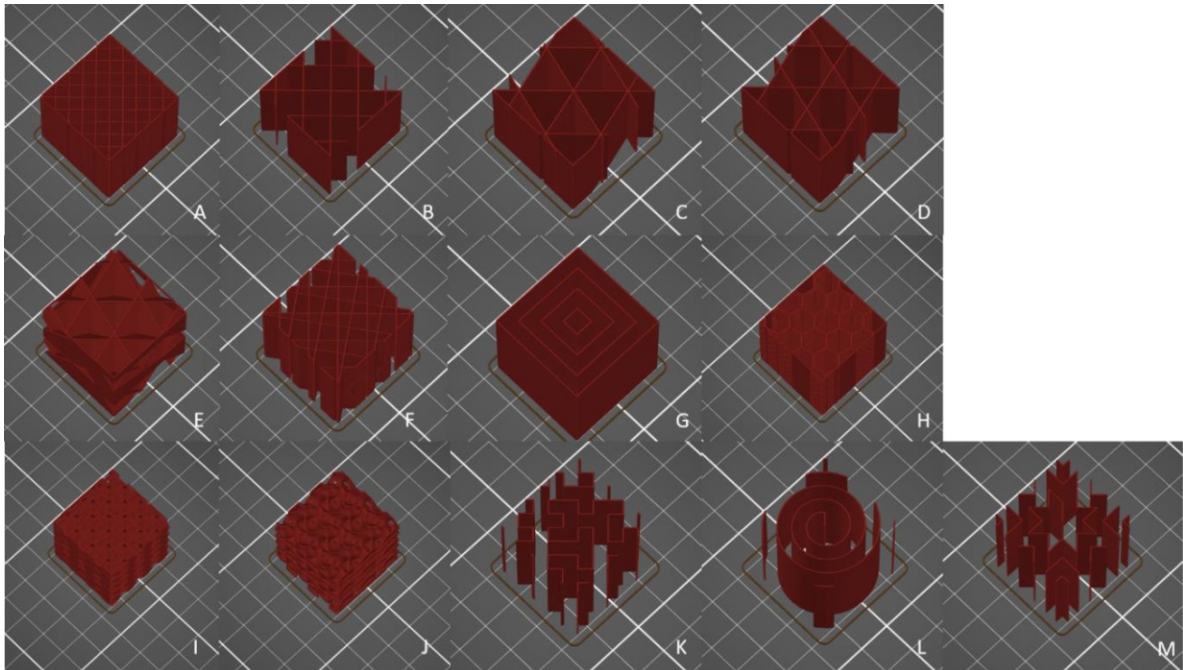


Figure 7: Slicing pattern available in Prusa shown on the basis of a cube with an infill density of 10%. (A) straight lines (B) grid (C) triangles (D) stars. (E) cubic (F) linear (G) concentric (H) honey comb. (I) 3D honey comb (J) gyroid (K) Hilbert-curve. (L) Archimedes arch (M) Archimedes spiral

4.2 Techniques

4.2.1 Stereolithography (SLA)

SLA is based on the principle of hardening a photosensitive resin punctually using light. It needs a vat filled with photosensitive resin (polymer) and a light source (Figure 8). The main components for an SLA printer are a vat filled with photosensitive resin, a light source which can be guided to irradiate single pixels (either using a scanning mirror or a micro mirror array) and a stage which moves the part to the next layer. Figure 8 shows a schematic drawing of a so called inverted/upside-down SLA, in this case the printing part is pulled out of the liquid (indicated by the arrow in z direction). For the generation of a 3D object the photosensitive resin is irradiated locally, according to the STL file, leading to a local polymerization reaction. When one layer is irradiated the stage moves up allowing for the resin to flow beneath the part and the subsequent layer is irradiated. The light source also penetrates the old layer to a certain degree allowing for a smooth transition between layers. This procedure is repeated until the workpiece is finished.

SLA needs post processing steps, such as the removal of the supporting structure (if one was necessary) or removal of unpolymerized resin. Typically, an end hardening process using UV light is also required. The manufactured piece then has a smooth surface and high resolutions are achievable.⁷³

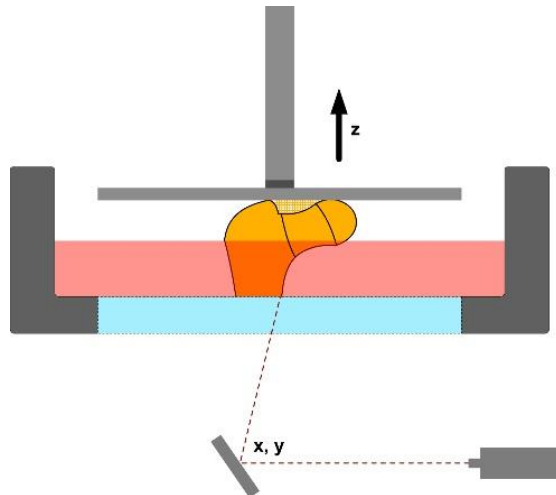


Figure 8: Schematic process of SLA

Since SLA allows the manufacturing of complex geometries with high accuracy, this technique found its way into medical applications and validation processes of FEA. Bibb *et al.* used stereolithography to produce over 25 accurate models of cancellous bone to enable easy validation of an FEA.⁸³ Furthermore, Petzold *et al.* found that SLA models are very useful for the diagnosis and preoperative process in the case of maxilla-cranio-facial surgery.⁸⁴

SLA was compared with FDM with regard to shrinkage rate, dimensional accuracy, cost and time it took to produce moulds. In this process, Choudari and Patil *et al.* found out that SLA performed better concerning shrinkage rate and dimensional accuracy, but the production time and costs are higher than in FDM.¹³ Therefore a trade-off between accuracy, time and cost in production has to be made before producing samples with SLA or FDM.

4.2.2 Fused Deposition Modelling (FDM)

Contrary to SLA FDM is typically faster due to its less complicated principle (Figure 9). Wound up filament (a thermoplastic material) is heated up through the nozzle head until its melting point is almost reached and laid down at the manufacturing stage. The sudden change in temperature causes the filament to solidify again. In the next step either the manufacturing stage or the extruder is moved down/upwards to lay down the next layer upon the previous one. This process is repeated until the wished geometry is achieved. A big advantage of FDM is that no post processing is necessary. The only expectation is, when the desired geometry needed a supporting frame, which has to be removed.⁷³

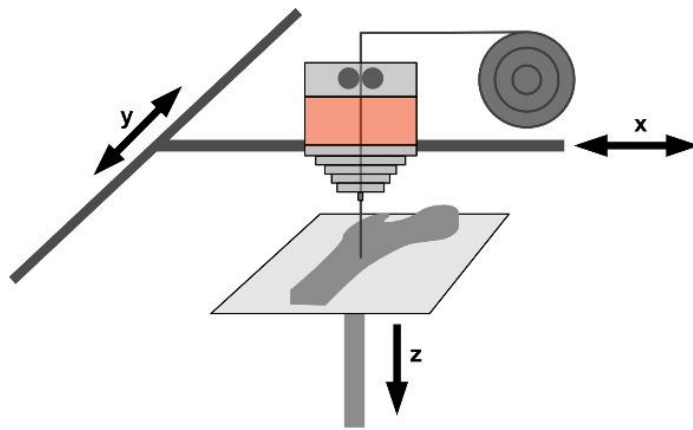


Figure 9: Schematic process of FDM

Raut *et al.* found out that the printing direction affects the mechanical properties of parts manufactured with FDM and has to be considered.⁸⁵ This was also confirmed by Warnung *et al.*, who tested the tensile behaviour of commonly used materials in FDM and compared them with data provide from manufactures.⁸⁶ If someone wants to optimize the tensile performance of the produced FDM parts, also infill density and number of layers are decisive according to Griffiths *et al.*⁸⁷

Hutmacher *et al.* showed that different mechanical behaviour of polycaprolactone (PCL) FDM printed scaffolds could be achieved when a physiological environment

was simulated. The printed structure was even completely filled with cells over a period of 3-4 weeks.⁸⁸ Van Uden *et al.* also used polycaprolactone to produce patient specific scaffolds with 100 % infill density and showed that FDM offers a rapid and low cost possibility to help cure degeneration of the intervertebral disc.⁸⁹ In addition to PCL Xu *et al.* used hydroxyapatite to produce an artificial goat femur, mimicking natural bone in mechanical behaviour, suggesting this material combination for the treatment of bone defects.⁹⁰

4.3 Materials used in FDM

Materials used for additive manufacturing can be divided into three main groups, namely⁹¹:

- Plastics/Polymers
- Metals
- Ceramics
- Others

This chapter will focus on three different polymer filaments (Polylactide (PLA), Polyethylene Terephthalate (PET) and Acrylonitrile butadiene styrene (ABS)) as those are the main materials in the method.

ABS is an amorphous thermoplastic polymer consisting of butadiene-acrylonitrile-copolymer embedded into a rigid framework of styrene-acrylonitrile copolymer. It is characterized with high fracture toughness. Besides FDM ABS is used in the automotive industry, for electronics and in the sanitary area to name a few industrial sectors.⁹² According to manufacturers, ABS has a tensile strength of 41-51 MPa, an *E*-modulus of 2.1 GPa and breaks at 20% strain. The nozzle temperature for printing is in the range of 210-260 °C Rodrigues-Panes *et al.* studied the influence on the mechanical behaviour of ABS concerning different AM parameters. It was found out that the layer height does not influence the mechanical strength results. However, when the infill density was raised the tensile performance was increased by almost a quarter. A reduction of the strength performance by 88 % compared to the bulk material was observed when

the specimen layers were printed perpendicular to the applied stress due to weaker bonding in the material.⁹³

The second material which is often used in industry is PET, known especially for plastic bottles. PET crystallizes slowly, which allows it to be used in an amorphous- lucent appearance or in a crystalline-opaque state.⁹² According to manufactures the raw material has an E -modulus of 2.15 GPa. The exact mechanical properties of PET however depend on the degree of crystallinity. It can be divided into two major categories; the partly-crystalline PET (PET-C) and the amorphous PET (PET-A). PET-C is a thermoplastic with intermediate strength but high stiffness and hardness, while having a relative low fracture toughness. The bulk material has an E -modulus of 3.6 GPa. In comparison, PET-A has a slightly lower stiffness and hardness, but performs better in terms of fracture toughness.⁹² Another version of PET is PET-G, which is modified with glycol. This results in a decrease in the degree of crystallinity and makes the material more lucent. Mercado-Colmenero *et al.* performed compression test of PET-G and found out that it has a lower average E -modulus of 1.3 GPa compared with PET (2.15 GPa).⁹⁴

PLA is an artificial polymer consisting of the naturally occurring lactic acid. Polylactide appears in two stereoisomers, where the L-configuration is primarily used in AM. Due to its melting point (180 °C) an extrusion temperature of 190-220 °C is often used.⁹² PLA has an E -modulus of 3.5 GPA and is stiffer than the described materials before. Rodrigues-Panes *et al.* also varied printing parameter for PLA manufactured workpieces and compared the results with ABS. An increase in layer height resulted in a decrease of tensile strength by 11% and an increase of the infill density also resulted in the improvement of the mechanical behaviour. It was found out that PLA has greater tensile strength and behaves more rigidly than ABS, while being the cheaper material.⁹³

4.4 Requirements and selected printing method and material

With regard to the printing process, the aim was to use a commercially available printing method that was as cheap as possible, had a good price/performance ratio, and allows the printing of hollow structures. For this reason, FDM was chosen over SLA as 3D printing method in this work, despite showing poorer layer adhesion and creating flaws in the printed sample. It's the cheapest method which uses relatively stiff and strong polymers, allows for hollow prints and uses harmless materials compared to SLA. PLA was chosen as a material due to its higher stiffness (~3 GPa) compared to ABS (~2 GPa) and PET (~2 GPa). Unfortunately, these advantages come with the disadvantage of anisotropic material behaviour of the part and a slightly inhomogeneous bulk material.

5 Imaging Techniques

A variety of image techniques are used in industry as well as medicine to access the inner structure of bodies and samples. Most commonly used are radiography (X-ray), computer tomography (CT), Magnet Resonance Imaging (MRI) and Positron-Emission-Tomography (PET).⁹⁵ Every method has its advantages but also drawbacks, like for example the usage of X-rays which can harm the body. An alternative image technique is 3D surface scanning, which enables the access to structural information without harming the sample in anyway. Though it provides only superficial information it is the imaging tool of choice for virtual anthropology.⁹⁶ This chapter will give a short introduction into the working principle of micro Computed Tomography (μ -CT) and 3D Surface Scan and their usage to access geometrical information which can be processed in a way to be used for additive manufacturing.

5.1 Micro Computed Tomography (μ -CT)⁹⁷

The interplay of computer tomography and AM has a long history dating back to the 1990, when Mankovich *et al.* used a CT-scan to reconstruct a skull using SLA.⁹⁸ Figure 10 shows a μ -CT from Bruker Corporation (40 Manning Road, Billerica, MA 01821) as an example for such a device. All μ -CT consist of an X-ray source (X-ray tube), a sample holder, detector and filter.

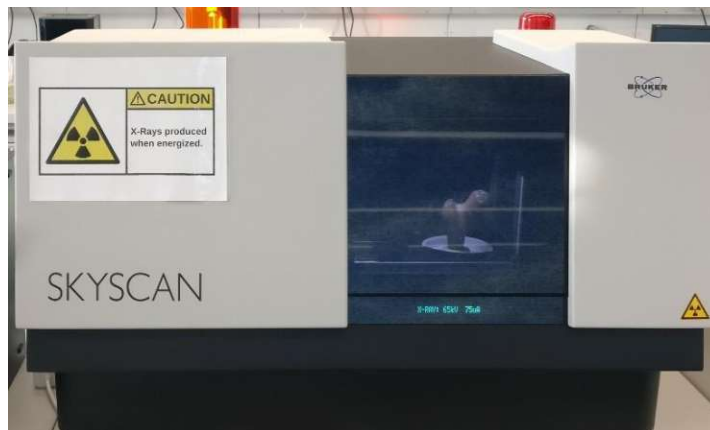


Figure 10: μ -CT from Bruker Corporation (40 Manning Road, Billerica, MA 01821), model Bruker Skyscan 1173[®]

The X-ray source emits x-rays which hit the sample placed on the holder (Figure 11). Due to density differences in the sample and the used energy, an attenuation of the incoming X-rays occurs, which can be described through Equation 1.

$$I_B = I_0 e^{-\mu d} \quad (1)$$

Where I_B is the beam intensity, I_0 the initial incoming beam intensity, μ the linear attenuation coefficient and d the distance from the x-ray source. To scan the whole sample, it is necessary to rotate the sample by 180° or 360° (Figure 11). This is done by angular steps and allows better capturing of the attenuation and inside properties of the sample due to changes in the projections. The choice of angular steps influences the number of projections scanned. For example, if a 360° scan is performed with an angular step range of 0.4° then 900 projections will be obtained for the reconstruction. A few post processing steps are necessary after the scanning procedure is completed.



Figure 11: schematic principle of μ -CT measurement

The obtained 2D projections of the object have to be reconstructed into a 3D object. There are a few options for the reconstruction, such as Fourier theorem or filtered back-projection. Micro CT images are often compromised with artefacts resulting from the reconstruction process. Beam hardening and ring artifacts are the most common ones. The first one is due to low energy photons getting absorbed stronger than high energy photons in a beam resulting in an increase of the average photon energy along the beam path and therefore hardening the beam. This

beam-hardening effect is shown in Figure 12, causing the depression of the curve after the steep increase, although passing the same material.

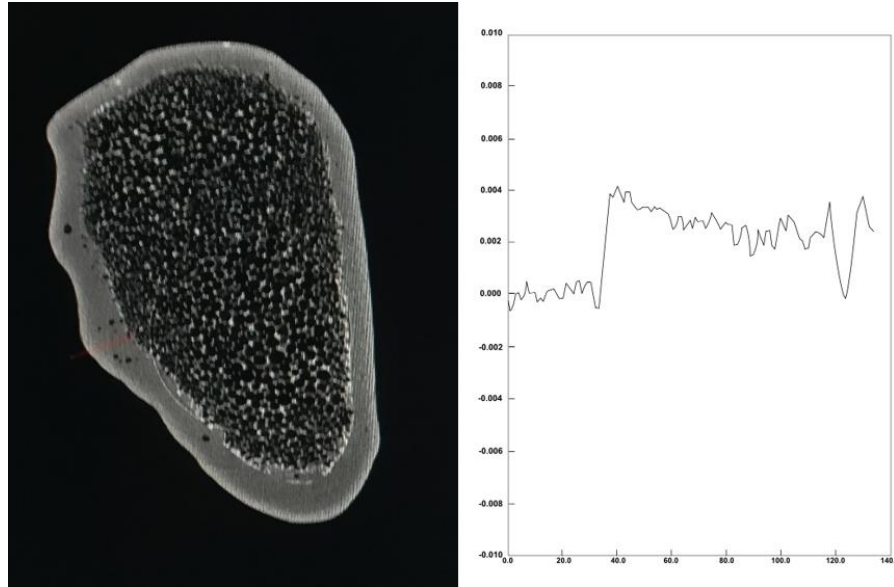


Figure 12: Beam-Hardening artefact shown on the basis of the reconstructed μ -CT of a purchased artificial bone

Ring artefacts are caused by errors of elements in the flat-field detector producing under- and over-estimated areas of the scanned sample. An example of such ring artefacts can be seen in Figure 13 below.



Figure 13: Ring Artefacts shown on the basis of a reconstructed μ -CT scan of a purchased artificial bone

After the successful elimination of these kinds of artefacts the obtained μ -CT image can be further processed for scientific research.

5.2 3D Surface Scan

In contrast to μ -CT, 3D surface scan is a non-invasive method to gain information of surfaces of objects. Fahrni *et al.* even compared these two techniques concerning their reproducibility and found out that 3D surface scan techniques performed better.⁹⁹ Besides the advantage of being a non-destructive technique, fragile objects can be scanned without the fear of destroying them, which is especially important for palaeoanthropology and archeology.⁹⁶ Friess *et al.* described two possibilities of how 3D surface scans operate. The first is based on the principle of measuring the time a light ray needs to be reflected back to the origin of the 3D scanner, which is often used for larger areas. The second operation mode is based on triangulation as shown in Figure 14. A light source emits a light ray which hits the object and gets reflected by it. The detector receives this information of distance and angle and an algorithm tries to triangulate the coordinates of the reflection due to calibrated points on the scanned plate. One major drawback of these technique is only information of the surface geometry is captured and the inner structure is not available.⁹⁶

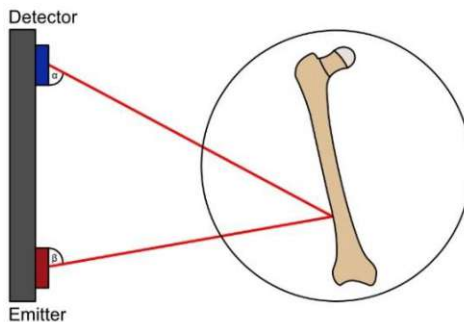


Figure 14: schematic sketch of the triangulation working principle of a 3D surface scanner.

If only structural information is needed, as for example to develop new footwear, 3D surface scan resembles a good choice.¹⁰⁰ These technique is also good to develop anatomical models for educational purpose as done by Thomas *et al.* In this study, the skeleton of a spiny dogfish and cane toad was scanned and then printed using selective laser sintering. These anatomical models showed almost all details of the skeletons with only a few exceptions.¹⁰¹ This study also showed that 3D surface scans can be used to access the outer geometry of bones and further processing enables the possibility to use additive manufacturing to print anatomically models of bones with a constant thickness and infill.

6 Materials and Methodology

6.1 Materials

In this master thesis, four different artificial bones were scanned (Surface scan and μ -CT), aligned, embedded and mechanically tested via compression tests. The artificial femurs were obtained from three different companies which are:

- 3B Scientific GmbH, Ludwig-Erhard-Str. 20, 20459 Hamburg, Germany
- SYNBONE AG, Tardisstrasse 199, 7205 Zizers, Switzerland, and
- A Pacific Research Company, 10221 SW 188th Street, PO Box 409, Vashon Island, Washington 98070, USA.

The samples ordered were:

- 2x ORTHOBones Standard Femur, right (3B Scientific GmbH)
- 2x ORTHOBones Premium Right Femur (3B Scientific GmbH)
- 2x Right Femur with distal canal opening (SYNBONE®)
- Femur, 4th Gen., Composite, 17 PCF Solid Foam Core, Medium (SAWBONES®)

The ORTHOBones as well as the SYNBONE® were polyurethane based. The SAWBONE® on the other hand was comprised of a composite material and can therefore be expected to perform better in mechanical testing. Figure 15 shows pictures of all artificial bones, which will be further abbreviated to OBS for ORTHOBone Standard, OB for ORTHOBone Premium, SYN for the SYNBONE® and SAW for the SAWBONES®. Furthermore, the abbreviation P for printed and K for “künstlich” (German) which means artificial in English, was introduced.

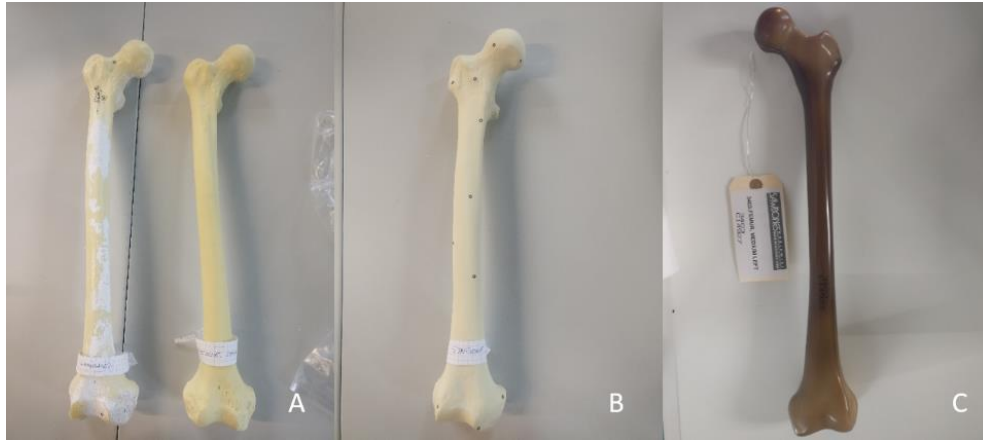


Figure 15: Artificial Bones: (A) OB and OBS (B) SYN, and (C) SAW

The geometry of the artificial bones from 3B Scientific® showed only little variation in geometry thus either OBS or OB was measured to obtain the sample geometry.

6.2 3D Surface Scans

Initially the sample shape was recorded using an optical 3D scanner, the GOM-Atos Core 300® (GOM GmbH, 38122 Braunschweig, Germany), to obtain a virtual representation of the bones. Further analysis was carried out with the provided software package GOM Scan® (GOM GmbH, 38122 Braunschweig, Germany) and GOM Inspect® (GOM GmbH, 38122 Braunschweig, Germany).

The samples were prepared by attaching the necessary reference markers. Furthermore, the brown surface colour of the sample from SAW made it necessary to apply an anti-gloss lacquer (MR® 2000 Anti-Reflex L) to be visible in the measurement. After that, the bone was placed on the rotation plate and the exposure time was adjusted for that specific position. It was important that the femur was not moved after taking the first picture, otherwise it would not be possible to stitch the pieces together to obtain a 3D representation of the whole bone in the end. To capture the whole surface structure the plate and/or the camera had to be moved after scanning the current position to expose the bone from a different angle. Since the laser is not only scanning the artificial bone, but also the rotational plate, a correction of the scanned data had to be made manually. This was achieved by the function “Cut out points” using the GOM Scan® software, which created a plane and underneath that, every point is cut off. When a rotation of 360° was reached and

therefore the upper surface of the femur had been scanned to the best possible way, the whole scan had to be saved as a series. To obtain the whole bone as 3D file the sample was rotated by 180° and the same procedure was repeated and stitched together using the applied reference points. The 3D structure was then polygonised, recalculated and exported as STL file using GOM Scan® software.

The post-processing of the obtained STL file, to close holes in the mesh, was done in GOM Inspect®. Since no obvious major holes were visible, the automatic function of filling holes was used to select through surfaces and the final STL file, shown in Figure 16, was exported.

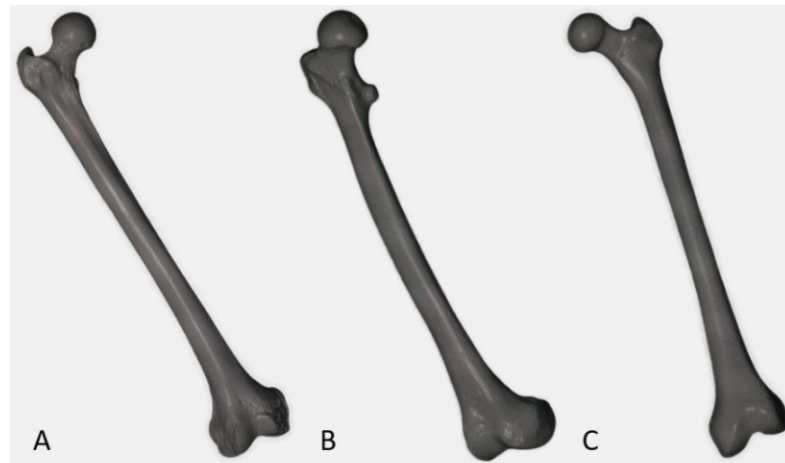


Figure 16: Illustration of the exported STL files. (A) OBS (B) SYN and (C) SAW

The obtained 3D surface scans were then compared with the STL file of the cortex obtained by segmentation of the μ -CT image to illustrate the deviation of both imaging techniques. This was done in Meshmixer 3.5® (Autodesk GmbH, 81379 Munich, Germany) by importing both STL files and manually bring them together as close as possible. Afterwards one of the STL files was set as target by selecting it and using Actions, set to target. The other file was then selected and using the select tab the surface to which the files should be aligned to was highlighted. Subsequently the align to target function, found under: select, edit, align to target, was used to finally align the two 3D files. The software then uses an algorithm to iteratively find the best-fit 3D alignment. To obtain the best possible fit the maximum values were used, being 100 iterations with 0.1 mm as error tolerance. The as obtained aligned STL-files were then compared using the analysis function: deviation.

6.3 Artificial Bone Alignment

For further testing only the proximal part of the femur was used, thus the samples had to be prepared accordingly. To do so, the physical bone samples had to be cut and embedded for further processing.

Due to limited space in the μ -CT chamber, the artificial bones had to be truncated. In addition, it was necessary to align the bones correctly in the mechanical axis of the femur, to later allow for a correct mechanical testing.

To achieve the correct alignment, the artificial bone was placed on supports and the *Distal Epiphysis* was fixed with cable ties (Figure 17 A). A line laser was used to find the shaft axis alignment. In this configuration, it was necessary to put spacers under the *Epicondyles lateralis* so that the laser light could be seen on the highest point of both the *Epicondyles lateralis* and the *Epicondyles medialis* (Figure 17 B). After these steps it was also necessary to align the bone horizontally in the correct plane. The set up was rotated by 90° and the femur was placed in a way that the light crossed the *Fovea capitis femoris* (Figure 17 C). Completing these steps, the fixed bone was transferred into a custom-made device, helping to align and cut the bone in the correct position. To be able to truncate the femur at the length of 14.5 cm, a simple measuring tape was used. A second laser was then used to align the artificial bones in the mechanical axis of the femur. For that purpose, the second laser was first aligned along the shaft axis, and then rotated by 3° , so that the light would cross through the middle of *Facies patellaris* and the middle of *Caput femoris* (Figure 17 D). The sample was fixated in this position using a circular clamp (best seen in F, white circular part with 3 screws). The next step was to highlight the position on the femur, where it should be cut off (Figure 17 E). To finalise the alignment the artificial bones were cut at the marked position (Figure 17 F) and were ready for the embedding process (see chapter 7.7).

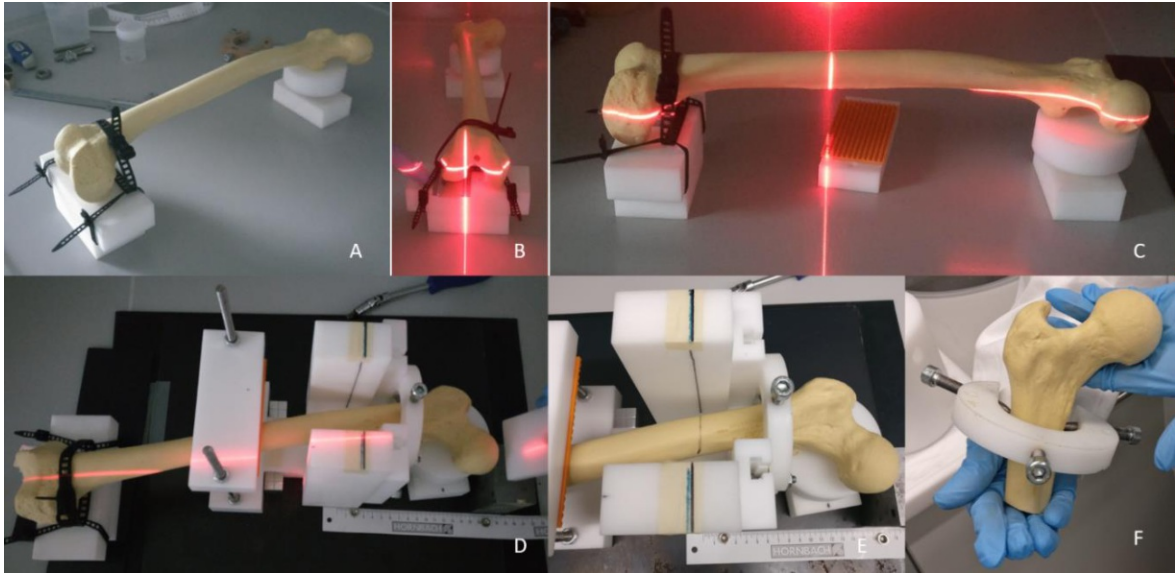


Figure 17: Workflow of the Alignment of the artificial bone. (A) Fixiation of Distal Epiphysis (B) Laser Alignment of Epicondyles lateralis and Epicondyles medialis (C) horizontal Laser Alignment (D) Alignment of the mechanical axis of the femur (E) marked cutting line (F) final cropped femur

6.4 μ -CT

To perform μ -CT the samples were embedded (see chapter 7.7) and attached to a special sample holder, as shown in Figure 18 A and placed in the μ -CT chamber (Figure 18 B).

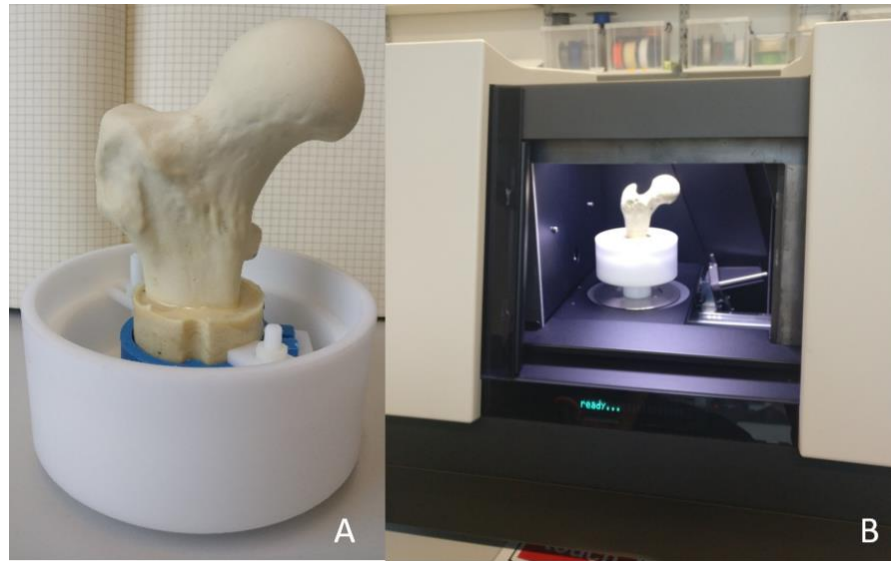


Figure 18: (A) Special holder for bones in the μ -CT (B) special holder and sample placed in the μ -CT chamber

The μ -CT was performed using a Bruker Skyscan 1173[®] (Bruker Corporation, Billerica, MA 01821). Prior to scanning the sample, a flat field correction was performed to correct for any field inhomogeneities. Since all bones are approximately 15 cm high, they are on the upper limit of the chamber size, and thus oversize scans had to be performed.

The sample OBS_1K was analysed first, using a voltage of 65 kV and a probe current of 75 mA at a resolution of 35 μ m. For SYN_1K a different sample plate had to be used leading to a lower resolution of 70 μ m. The scan of the SAW bone was performed using the same settings as were used for the SYN_1K. In addition, no filter was used for scanning all three artificial bones. The complete set of scan parameters is included in Appendix Figure 65-67.

For processing of thy μ -CT scans the data was reconstructed using the NRecon[®] software. In the first step the single images were aligned with respect to each other as to reflect the scanned sample. In a second step a beam hardening correction was performed, followed by a ring artefacts reduction.

6.5 Image Processing in Medtool 4.5

The obtained μ -CT files had to be further processed before an STL surface files could be created for printing the different artificial bone geometries. To do so, the Medtool 4.5 software (Dr. Pahr Ingenieure e.U., Pfaffstätten, Austria) was used to convert the .tif files obtained from the μ -CT scan to one .mhd file and to segment the bones between cortical and trabecular region. Afterwards the desired geometry was extracted and exported as proper STL file ready for 3D printing.

6.5.1 ORTHOBone_Standard (OBS) and ORTHOBone (OB)

First, the obtained μ -CT scan had to be rescaled to save memory and ensure faster processing. This was done with a resize filter, which changes the resolution by a set factor. In this case, a change of resolution by a factor of 10 was used (Figure 19 A). The consequence of this was that 10 voxels were summed up to one new, larger voxel in all spatial directions leading to a thousand-fold lower file size. The image resolution after this step was 350 μ m. In order to further reduce the file size, it was also necessary to scale the grey value range from 0 to 255 and set the raw image

format to unsigned integer. Furthermore, midplanes and projected images of the bone were created to visualize the femur and its embedding. Since only the geometry of the artificial bone is of interest, the image had to be properly segmented. Therefore, an arithmetic filter (-arith) was used to segment out the femur and get rid of the surroundings (Figure 19 B). Since the grey values outside of the bone were around 50 and the inside around 110-120, an arithmetic filter was used. As a consequence, every grey value above 120 got set to a grey value of 0 and every under 30 was also set to 0. In a second step of cropping, to obtain the region of interest, a neighbourhood filter: morphological operations 2 (-morph), was used. A kernel of 3x3 with the opening operation and a threshold of 50 was chosen. This meant that, first a cube of 3x3x3 voxels was subtracted before added again, to be able to cut away parts, that are thinner than the used kernel (Figure 19 C). This filter allowed to remove the remainder of the embedding and the holder structure. Before the extraction of the cortex and spongiosa could be started, the image was cleaned to get rid of lose voxels, which are not connected to the whole bone structure by using the modifying filter clean image. In an attempt to smooth the edges another morphological filter was used (-morph), but this time with closing, instead of opening operation (Figure 19 D). A rectangular shape with the size of 3 voxels and a threshold of 50 was used. Since no clean edges were achieved this way, the option of exporting the data set to 3D Slicer 4.11.20200930 was utilized. For this purpose, the pre-segmentation done in Medtool 4.5 was exported to 3D Slicer 4.11.20200930 and manually touched up to achieve the segmentation shown in Figure 19 E. This was done by first smoothing the pre segmentation and then paint and erase parts of the cortex where it was necessary. Since the spongiosa is also of interest as a separate file, the compute filter, fill pores, was used to get the geometry of the complete bone without distinction between cortex and spongiosa (Figure 19 F). In the next step, the use of the -arith filter allowed the subtraction of the whole bone minus cortex by setting volume A (=hole bone), -A (for subtraction) and inserting the second volume (cortex), the result is shown in Figure 19 G. As a last step for the segmentation process of the OBS, the spongiosa image had to be inverted by the usage of the arithmetic filter (-arith) by setting every voxel with a grey value of 0 to 1 and

everything larger than 1 to 0 (Figure 19 H). Now the cortex and spongiosa were ready to be further processed for the generation of the required STL files.

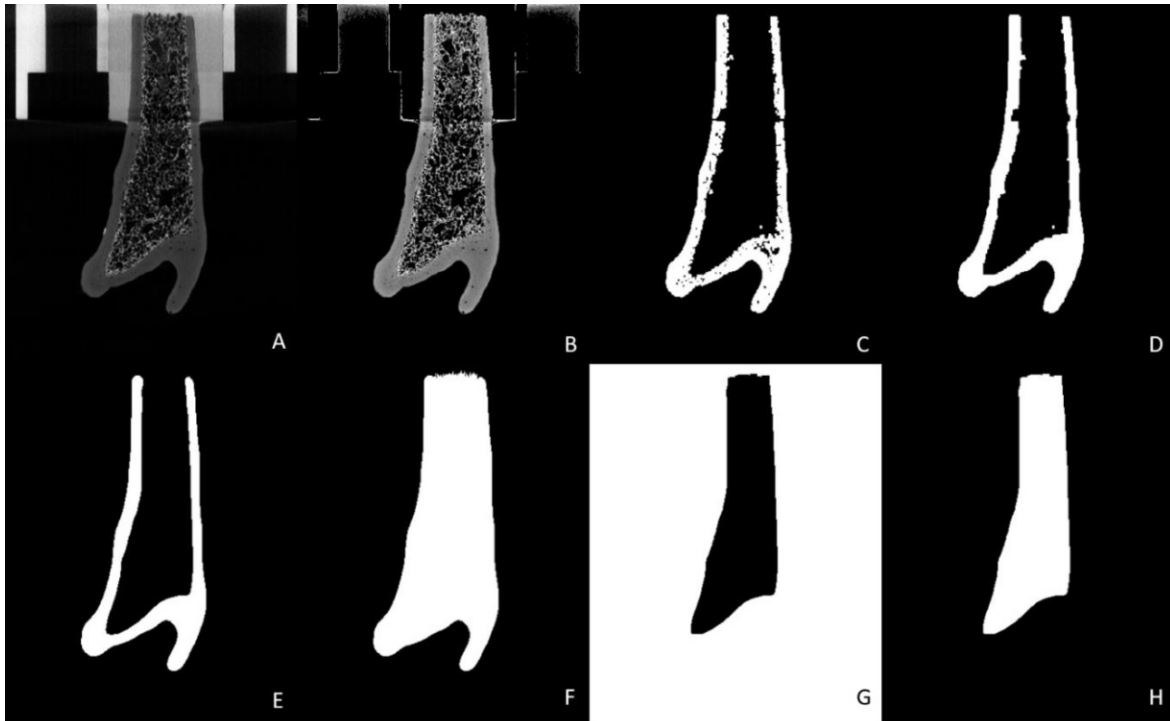


Figure 19: Steps of Segmentation in terms of Midplanes of ORTHOBone. (A) rescaled image (B) usage of -arith filter (C) usage of -morphk opening filter (D) usage of -morphk closing filter (E) Segmentation in Slicer 4.11.20200930[®] (F) fill pores filter (G) usage of -arith filter to subtract cortex from bone to get the spongiosa (H) inverted spongiosa

6.5.2 SYN BONE[®] (SYN)

At first, the μ -Ct image also had to be rescaled by changing the resolution by a factor of 2 and then again by a factor of 3 (Figure 20 A) followed by setting the raw image format to unsigned integer and scaling the grey values to a range from 0 to 255. The image resolution for further processing was 420 μ m. For the first cropping step (Figure 20 B) the arithmetic filter (-arith) was used setting every grey value above 120 and below 20 to zero. To get rid of the sample holder, the -morphk filter with a kernel of 3x3 pixel and threshold of 36 grey value was used in opening mode (Figure 20 C). As through the very thin cortex and therefore no clear differentiation between the grey values of cortex and spongiosa at the *Fossa trochanterica* a further segmentation (see Figure 20 D-E) was done in multiple steps manually in 3D Slicer 4.11.20200930[®]. This was done by first smoothing the pre segmentation

and then painting and erasing parts of the cortex where it was necessary. With the final segmentation of the cortex (Figure 20 E), the fill pores filter was used to obtain a mask of the whole bone and refined manually in 3D Slicer 4.11.20200930[®] shown in Figure 20 F. Next the subtraction of the cortex from the whole bone, to obtain the spongiosa, was performed using an arithmetic filter (-arith) by loading a volume A (=whole bone) and usage of the operation -A to subtract the second loaded volume (=cortex). As shown in Figure 20 G, the grey values of the spongiosa had to be converted to 0 and 1, which was done by setting all values which are equal to zero to 1 and everything bigger than 1 to zero, thereby the image was converted as shown in Figure 20 H. Now the cortex and spongiosa were ready to be further processed for the generation of STL files.

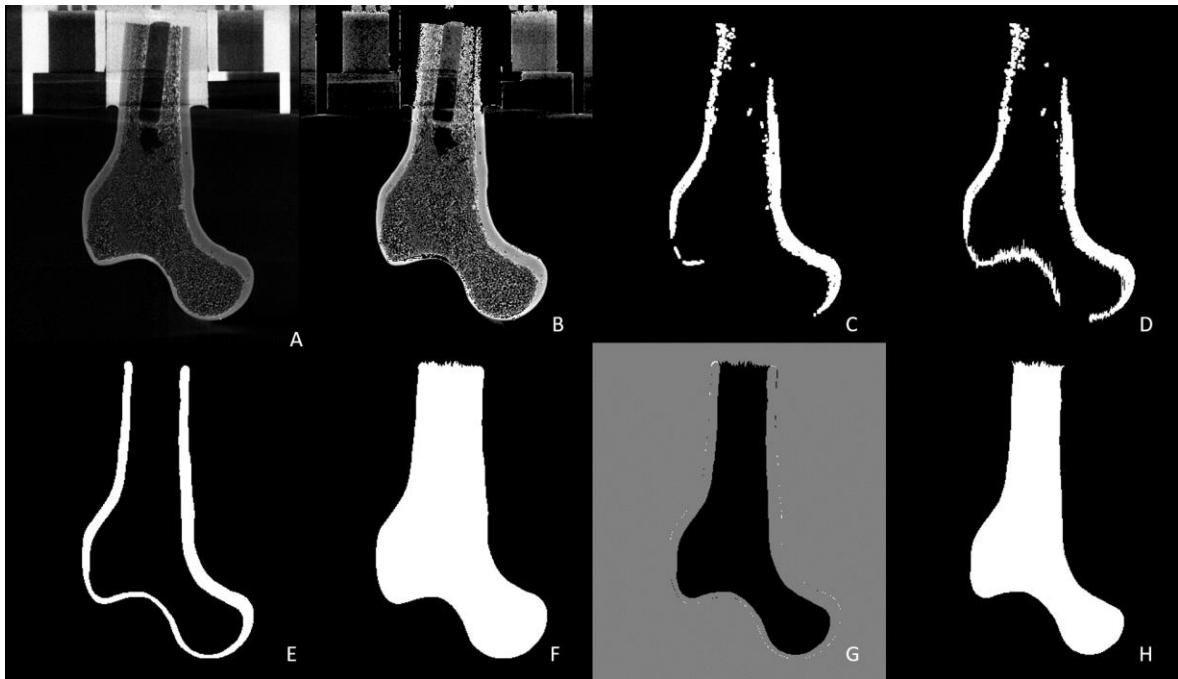


Figure 20: Steps of Segmentation in terms of Midplanes of SYN. (A) rescaled image (B) usage of -arith filter (C) usage of -morph opening filter (D) first manually segmentation in 3D Slicer 4.11.20200930[®] (E) final segmentation of the cortex (F) fill por filter (G) usage of -arith filter to subtract cortex from bone to get the spongiosa (H) inverted spongiosa

6.5.3 SAWBONE[®] (SAW)

In the case of SAWBONE[®] a distinction between spongiosa and cortex was easier in the shown μ -CT (Figure 21 A), due to the composite material. First the converted scan had to be rescaled by a factor of 5 using the resize filter “change resolution by factor”. The image resolution after this step was 350 μ m. Furthermore, the raw image format was set to unsigned integer and the grey values had to be rescaled from zero to 255. To get rid of the embedding and the holder structure, every grey value smaller than 100 was set to zero using an arithmetic filter (-arith) as shown in Figure 21 B. Next, a binary mask was created by setting every grey value above 1 to exactly one, which led to the segmentation shown in Figure 21 C. It can clearly be seen that, the segmentation has a hole in the *Caput femoris*, which was closed manually by using the 3D Slicer 4.11.20200930 software (Figure 21 D). To be able to extract the spongiosa as well, it was necessary to use the fill pores filter to obtain the whole bone with the final fine segmentation done in 3D Slicer 4.11.20200930 software as shown in Figure 21 E. Subsequently, the spongiosa was obtained by subtraction of the cortex from the whole bone using an arithmetic filter -arith. For that the whole bone was loaded as a volume A and the operation -A was used to subtract the second loaded volume (=cortex) from it. The obtained spongiosa shown in Figure 21 F then had to be inverted to have the final grey values of zero and 1. Therefore the arithmetic filter was used once again by setting every pixel having a grey value of zero to a new value of 1 and every pixel having a value larger than 1 was set to zero. The final result is shown in Figure 21 G. Now the cortex and spongiosa were ready to be further processed for the generation of STL files.

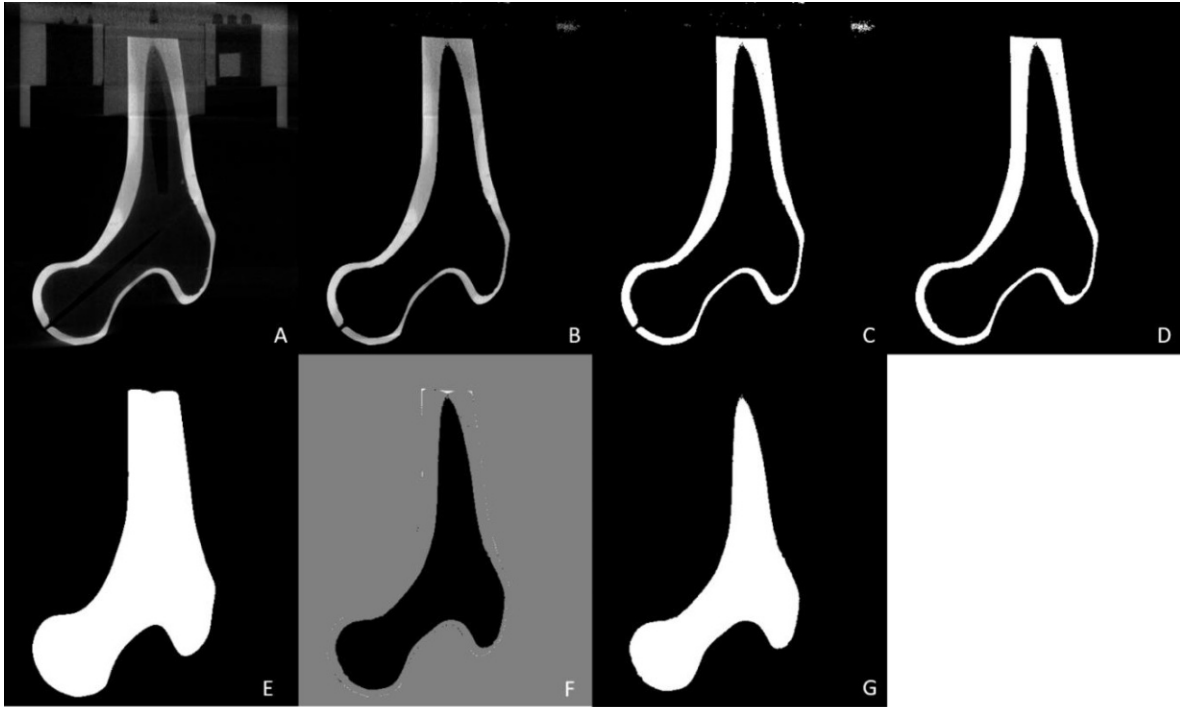


Figure 21: Steps of segmentation on terms of Midplanes of SAW. (A) rescaled image (B) usage of -arith filter (C) binary mask of the cortex (D) manually segmented cortex (E) fill pores filter (F) usage of the -arith filter to subtract the cortex from the whole bone to obtain the spongiosa (G) inverted spongiosa

6.6 3D Printing

7.6.1 Extraction of the STL Files

To convert the labelled .mhd files of the obtained cortex and spongiosa segmentations, another script in Medtool 4.5 (Dr. Pahr Ingenieure e.U., Pfaffstätten, Austria) was used. The option a fabrication processor sheet instead of an image processor sheet, made it able to easily convert the labelled files by just reading in the .mhd files and using the -fevox script to output an STL file for each label. This was done for all spongiosa and cortices of the artificial bones obtained by the methods described in chapter 6.5 Image Processing in Medtool 4.5. A schematic image of the extracted cortices and spongiosa STL files are shown in Figure 22 A-C. For a better visualization, the surfaces are already sliced and only half of the model is shown.

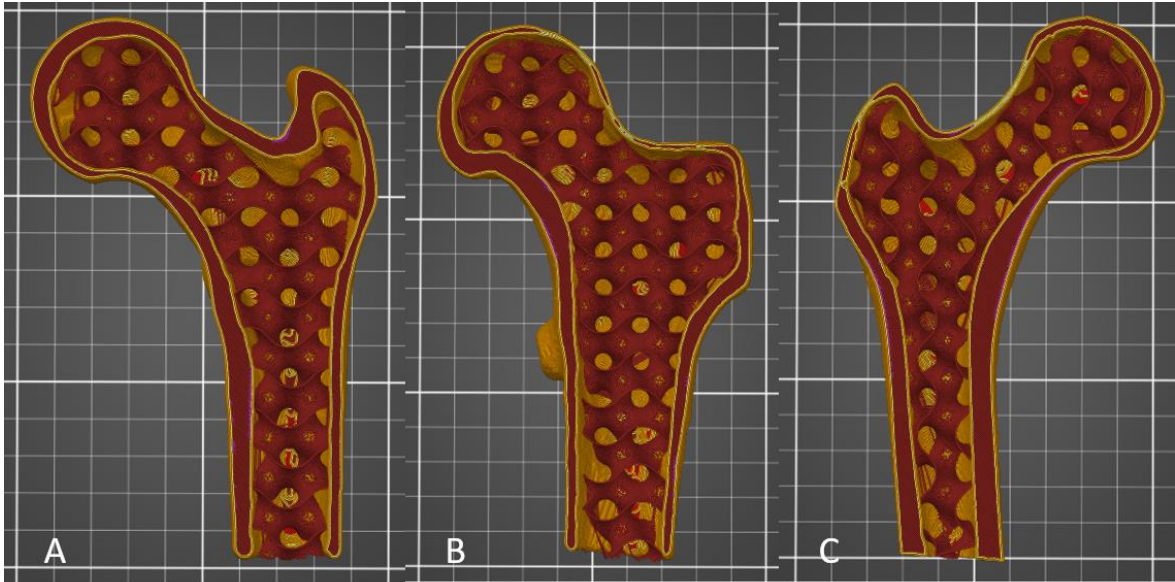


Figure 22: schematic figure of the obtained spongiosa (gyroid pattern, 5% infill) and cortex (linear pattern, 100% infill) of the artificial bones. (A) for OBS and OB (B) for SYN (C) for SAW

6.6.2 Infill Density Estimation

After obtaining the necessary STL files from the cortex and spongiosa, two major questions emerged. First, how stiff is the foam inside the artificial bones which is used to represent the spongiosa (Figure 23) and secondly, how can this stiffness be related to the infill density of the 3D printed analogues.

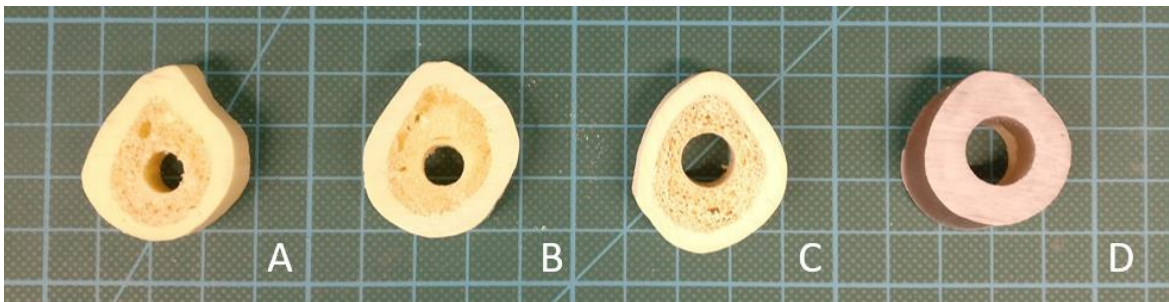


Figure 23: Cortex and Spongiosa shown of the different artificial bones. (A) OBS (B) OB (C) SYN (D) SAW

To answer the first question, cubes with an edge length of 10 mm were milled out of the distal end of the artificial femurs of ORTHOBone_Standard (OBS), ORTHOBone (OB) and SYNBONE® (SYN) and compression tests were performed as shown in Figure 24. Then the E -modulus of the different foams were calculated

by relating the stresses and strains obtain from force-displacement measurements. The obtained E -moduli of the cubes can be seen in Table 1.

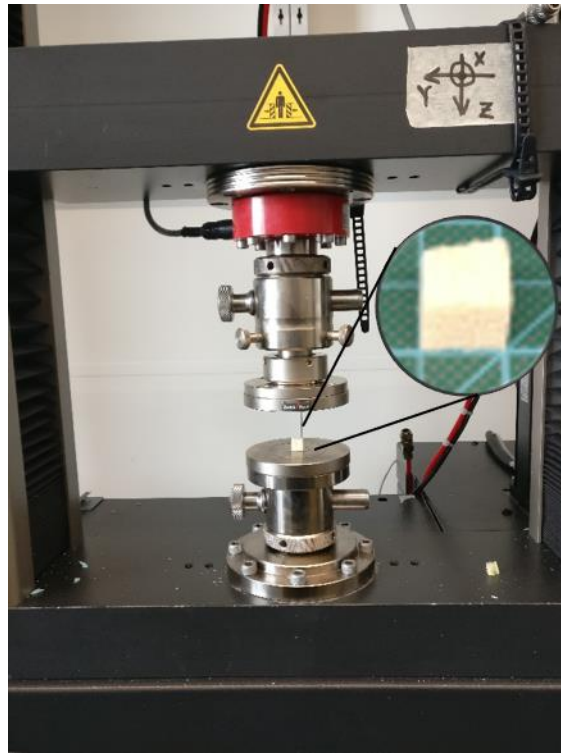


Figure 24: Compression test of the milled cube of infill foam to represent the artificial spongiosa

Table 1: Determination of the infill density by performing compression tests of cubes

Sample	E -modulus in MPa	Average in MPa	Standard Deviation in MPa	Infill Density
OBS_W1	9.49			
OBS_W2	9.02	9.06	0.4115	7%
OBS_W3	8.67			
SYN_W1	41.8			
SYN_W2	30.66	33.67	7.12	10-15%
SYN_W3	28.54			
OB_W1	29.65			
OB_W2	27.66	35.6	12.07	10-15%
OB_W3	49.49			

The second question was answered by testing different infill densities of the gyroid pattern. The gyroid pattern was chosen to resemble the structure of trabecular bone. The testing of 30x30x30 mm cubes (Figure 25 B) with infill densities of 10%, 20% and 40% was performed in a project previous project.¹⁰² In this study, compression test were performed on printed PLA cubes, which were loaded orthogonally to the printing direction (sample_z) or in the printing direction (sample_xy). The established relationship between E -modulus and infill density was used to match the obtained E -moduli from the foams to a proper infill density by looking at the sample_z curve (Figure 25 A). The chosen infill densities for printing the spongiosa are shown in Table 1.

The initial aim of the project work¹⁰² was to find a power law connecting bone density with the gyroid pattern density using Equation 2 making it possible to fit the infill density to patient specific bone conditions in the future.

$$E_{\text{eff}} = E_{\text{bone}} * \rho_{\text{infill}}^k \quad (2)$$

Where E_{eff} is the resulting E -modulus of the tested cubes in MPa, E_{bone} is the E -modulus of bone assumed to be 6000 MPa, ρ_{Infill} the infill density of the tested cubes and k is the power law factor, chosen to be 2.

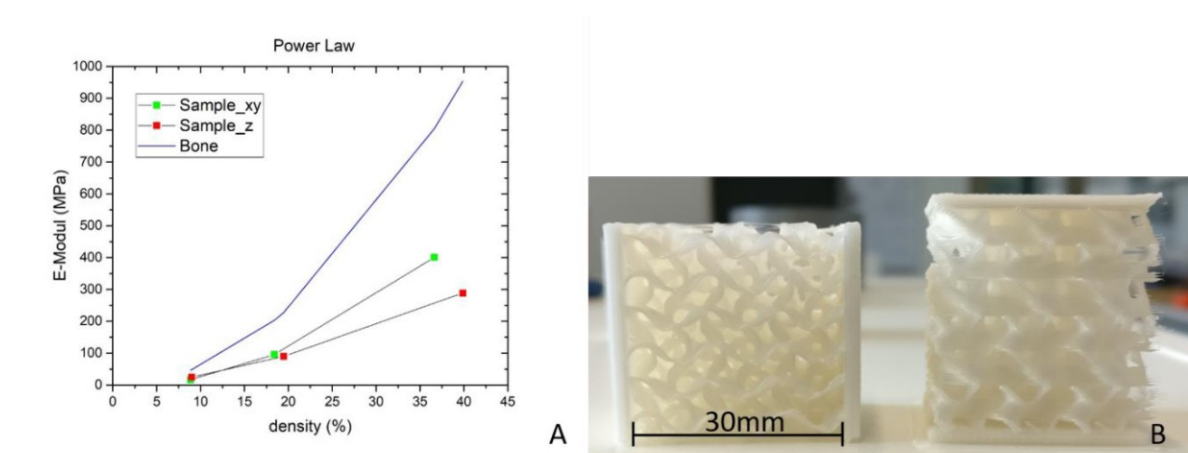


Figure 25: /A) Power law of previous work¹⁰² showing the calculated Power law and experimental curves from cubial PLA samples with varying Gyroid infill. (B) sample_z (tested orthogonally to the printing direction) and sample_xy (tested in printing direction) both with a gyroid infill pattern and 10% infill density

According to this work the infill densities were chosen: For OBS spongiosa an infill density of 7% was used while for OB and SYN 12% were used, due to them having a similar E-modulus.

SAWBONE[®] was not tested, because the company offered the mechanical data and the assumption of an *E*-modulus of 155 MPa was made. This led to an infill density of 27 % for the spongiosa of the SAW bone.

6.6.2 Slicing and Printing Parameters

For slicing of the obtained STL files a software from Prusa[®], PrusaSlicer 2.1.1[®] was used to obtain the necessary g-code for 3D printing. Figure 26 shows the workspace in PrusaSlicer 2.1.1[®]

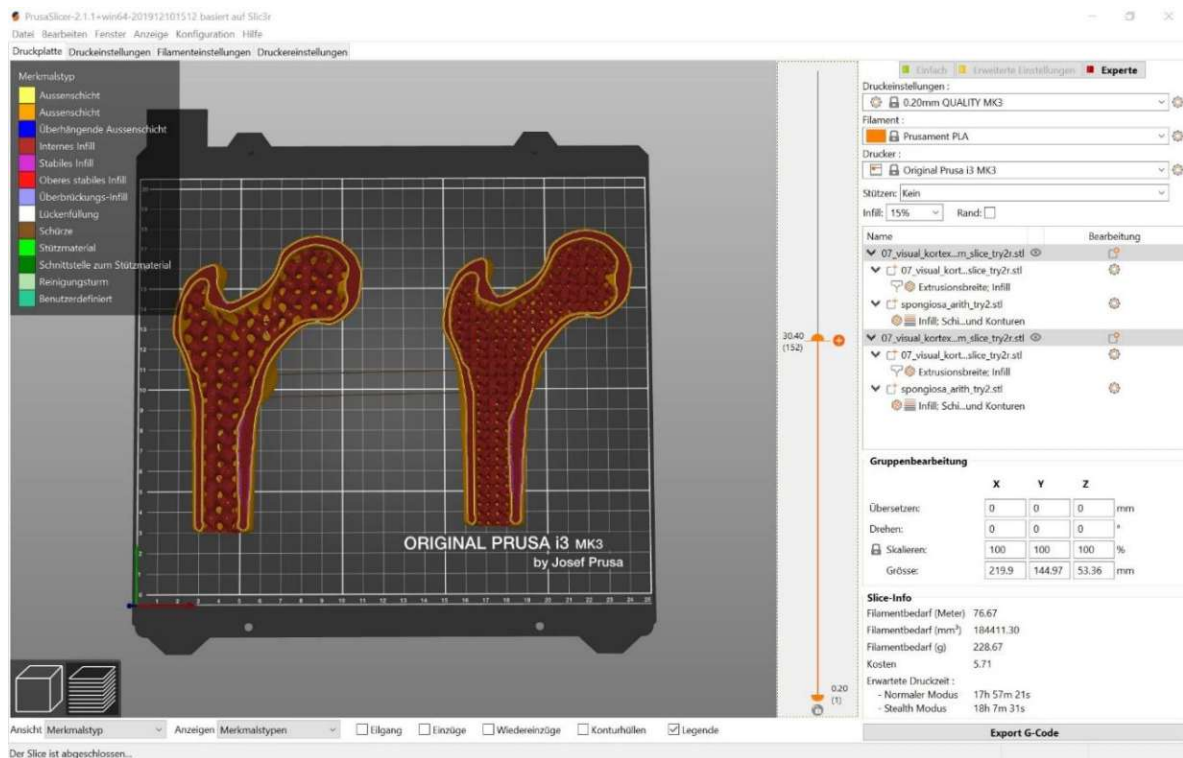


Figure 26: Printing plate of PrusaSlicer 2.1.1[®] with sliced bone samples

First, the STL file of the cortex was loaded and marked to successfully add another part, the spongiosa, to it. In this case, cortex and spongiosa were grouped together but it was possible to use different infill and printing parameters. A linear infill pattern

with 100 % density was used for all cortices regardless of the manufacture of the artificial bone. In case of the spongiosa a gyroid pattern was used for all samples.

What all cortices had in common are the extrusion widths, infill pattern and infill density (the parameters can be seen in Table 2 and Appendix). On the other hand, the spongiosis had in common the layers and perimeter settings and the infill pattern. The default settings of Prusa Slicer 2.1.1[®] were used, only the parameters in Table 2 were changed. Especially higher extrusion width (default 0.42 mm) was set to increase the layer adhesion.

Table 2: Common printing settings for cortex and spongiosa (EW stands for extrusion width)

	Setting	Value
Cortex	Infill pattern	linear
	Infill density	100 %
	EW Outer contour	0.6 mm
	EW contour	0.6 mm
	EW Infill	0.45 mm
	EW Massive infill	0.6 mm
Spongiosa	Infill pattern	gyroid
	perimeter	0

Regardless of the cortex and spongiosa settings, 0.20 mm QUALITY MK3, original Prusament Filament® and Original Prusa i3 MK3® (shown in Figure 27), as a printer, were chosen. Since the samples were printed orthogonally to the testing direction, a support for the laying bone was needed and created automatically. After choosing the printing temperature on the upper limit for the Vanilla White® Prusa Filament of 225 °C for better cohesion, the bones were ready to be sliced. The necessary g-code was saved and exported to the 3D printer and the printing process was started. Figure 27 shows one of the samples during the print.

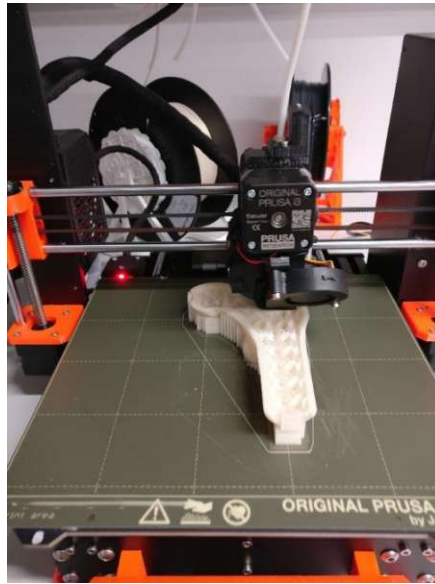


Figure 27: Original Prusa i3 MK3® printing process for the PLA femur

6.7 Embedding & Mechanical Testing

6.7.1 Embedding

Before the printed bone could be mechanically tested via a compression test, it was necessary to remove the support frame and embed the bone at the distal end and the *Caput femoris* as shown in Figure 28 A-B. The samples were embedded using a two-component polyurethane resin from FDW®, in detail the SG 141/4 Komp. A polyurethane resin was mixed together with the PUR 145 Komp. B hardener. Both components were intimately mixed in a 1:1 ratio and stirred until an increase in temperature was noted. The sample was fixed to the embedding device shown in Figure 28 A-B and the resin was added. After a curing period of 20-30 min the samples were ready for compression testing

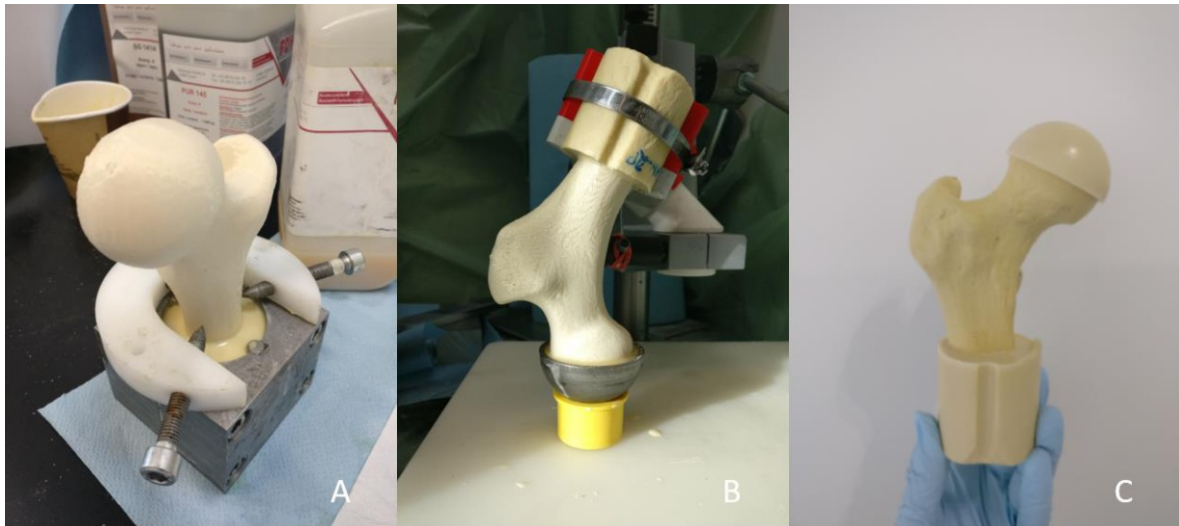


Figure 28: Schematic Embedding process. (A) embedding of the distal end of the printed bone (B) embedding of the *Caput femoris* (C) final embedded bone, ready for compression test

6.7.2 Mechanical Testing

The compression tests were performed on a Z030 machine (ZwickRoell GmbH & Co. KG, D-89079 Ulm, Germany) and the test settings were based on those of Dall'Ara *et al.*³¹. More precisely the compression curve was captured position controlled at 100 Hz using a compression rate of 5 mm/min, the samples were tested until failure. The machine displacement u and the force F was recorded.

Since the scanned bones were already aligned 3° deviating from the shaft axis, it was necessary to tilt the test device for another 17° to realize the desired 20° between the shaft axis and the loading direction, as shown in Figure 29, to simulate a typical load stand situation of a human femur.

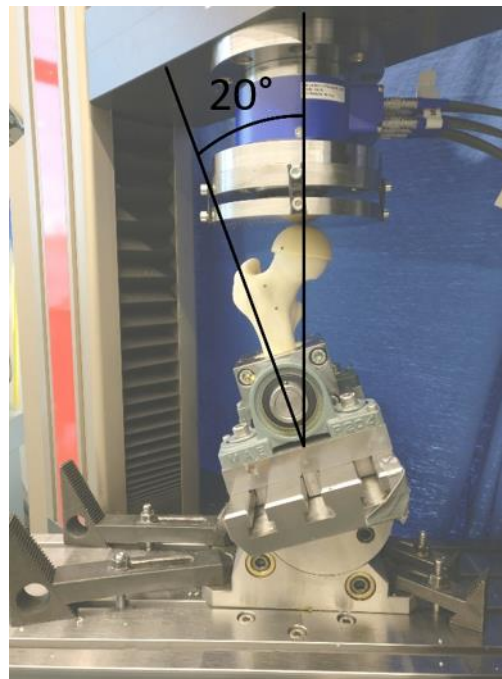


Figure 29: Set-Up for compression test of the printed and artificial bones in marked STANCE position (20°)

Furthermore, the highest point of the *Caput femoris* was aligned in the middle of the testing machine with the help of a laser pointer as shown in Figure 30.



Figure 30: Laser Alignment of the *Caput femoris* for the right position for compression test

To better understand the fracture dynamics the testing was filmed using a Sony Alpha 6400® (Sony Europe B.V., The Heights, Brooklands, Weybridge, Surrey, KT13 0XW, United Kingdom) camera initially. For later tests a highspeed camera, a PCO Dimax CS® (PCO AG, 93309 Kelheim, Germany), was used to better visualize the fracture process.

The ultimate Force F_{ult} and the stiffness of the tested bones, artificial and printed, were evaluated and compared. This was done by recreating the force-displacement curve of the compression test using Excel 2019®. Since the samples were tested without applying a pre-load, the obtained graphs had to be corrected as shown in Figure 31. For that, it was necessary to estimate where the linear region of the curve approximately started and correct the displacement by subtracting the displacement value in this point from the following displacement values.

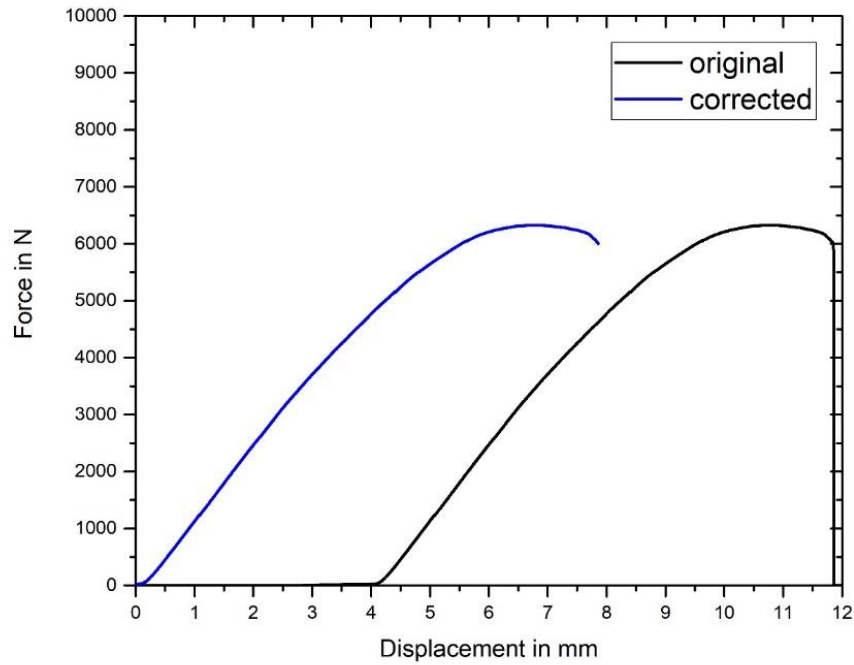


Figure 31: Correction of the obtained compression curve

In the case of SAW_1K (the composite bone from “A Pacific Research Company”) another correction was made due to the crack in the curve. To smoothen the curve, first the point where the crack occurred was searched. Followed by searching for the point where the test reached again the force before the crack. To obtain one curve, the displacement difference between these two points were subtracted between the two cracks and the new graph was visualized using Origin 2016® and is shown in Figure 32 below.

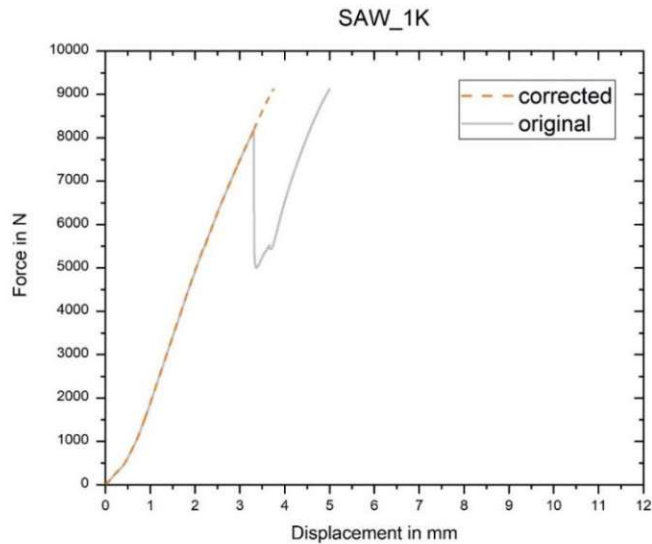


Figure 32: Correction of the SAW_1K force-displacement curve

Furthermore, as shown in Figure 33, the ultimate Force F_{ult} was determined by the highest force value before the failure of the sample. The corresponding stiffness S of the printed and artificial bones were determined by finding tangents in the displacement range between 0 and 2 mm in 0.05 mm steps using Equation 3 and the average value of the stiffness in this linear region of the compression test was used for further discussion.

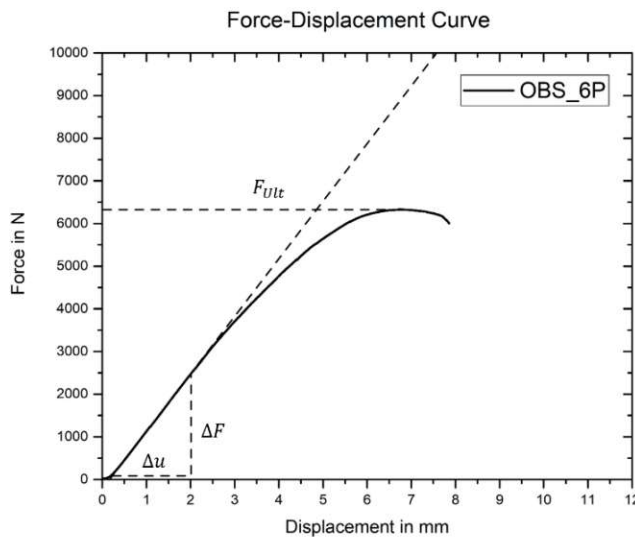


Figure 33: schematic force-displacement curve of OBS_6P to show how the characteristic values of F_{ult} and S were determined in the range of 0 to 2 mm displacement

$$S = \frac{\Delta F}{\Delta u} \quad (3)$$

Where S is the stiffness of the sample in N/mm, ΔF is the change in force in N and Δu the change in displacement in mm.

Since more than one sample were printed and tested for each geometry, the average and standard deviation for all samples of OBS, OB, SYN and SAW were calculated according to Equation 4 and 5.

$$\bar{x} = \frac{1}{n} \sum_{i=1}^n x_i \quad (4)$$

Where \bar{x} is the average, n the amount of data points and x_i representing every data point.

$$\sigma = \sqrt{\frac{\sum (x - \bar{x})^2}{n - 1}} \quad (5)$$

Where σ is the standard deviation, x represents a data point, \bar{x} is the average and n is the amount of data points.

7 Results

Goal of this master thesis was to compare the mechanical performance of artificial bones and their printed counterparts. The respective results of stiffness, ultimate force as well as the results of the 3D surface scan comparison with the μ -CT results of segmentation are summed up below.

7.1 ORTHOBone_Standard

Two different imaging methods were used to obtain the bone's geometry and internal structure. While a 3D surface scan was used to obtain a 3D representation of the sample's surface, μ -CT allowed for analysis of the internal structure.

To obtain an STL file of the artificial cortex as well as the spongiosa a segmentation was performed and is shown in Figure 35 below. The figure shows the segmentation of spongiosa (Figure 35 A) and cortex (Figure 35 B) on its own as well as both in an overlay with the original midplane (Figure 35 D).

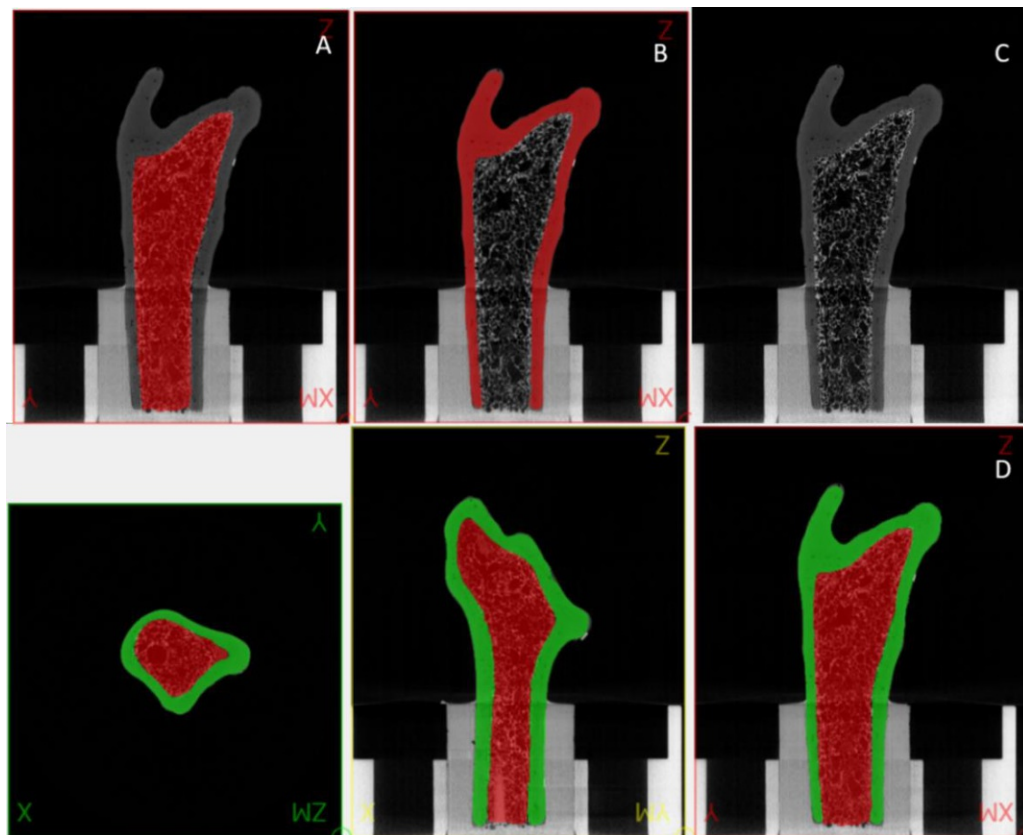


Figure 34: Segmentation of OBS (A) segmented spongiosa (B) segmented cortex (c) midplane without segmented region (D) segmented spongiosa and cortex shown on the original midplane output in different direction in space

The obtained 3D representation of the cortex was then compared to the results of the 3D surface scan Figure 35A shows the result of the alignment of both bones and their deviation from each other (Figure 35 B). The green area shows the STL file obtained from the segmentation of the μ -CT, while grey represents the 3D surface scan STL. Both files did fit well to each other as the red area indicates deviations higher than 0.5mm (Figure 35 B). Pins shown in Figure 35 B are created by the function deviations in Meshmixer 3.5[®] (Autodesk GmbH, 81379 Munich, German) and are there for further selection of the points and surfaces that deviate from each other.

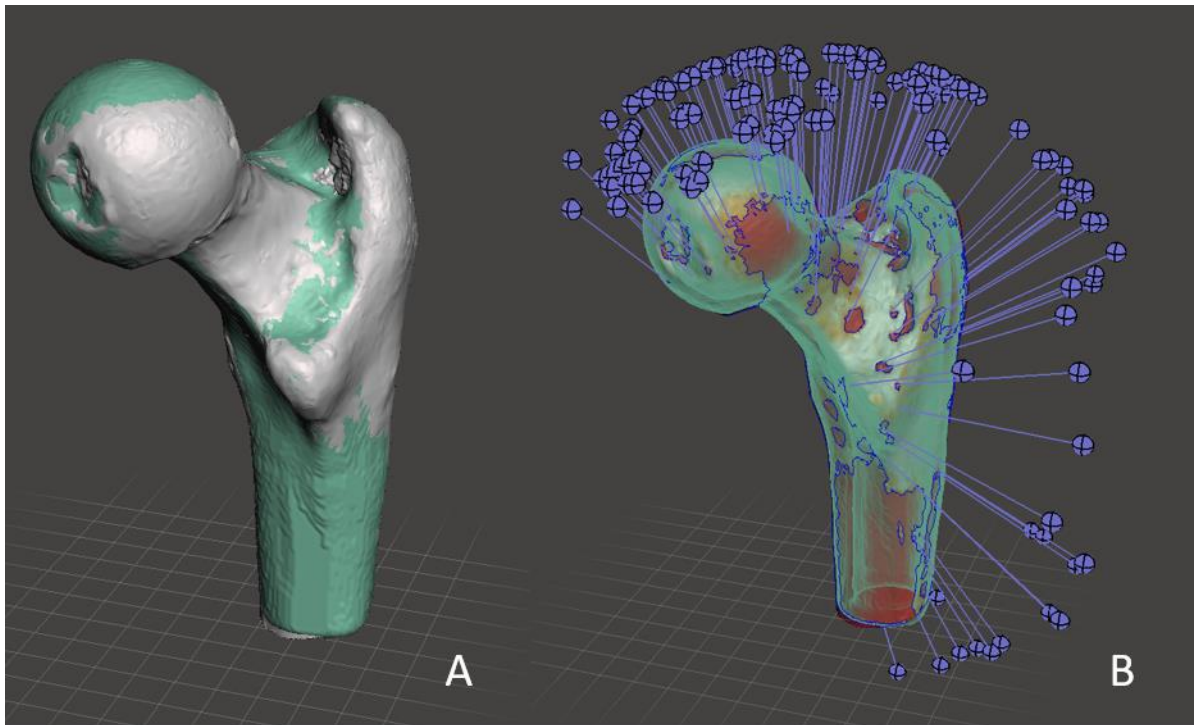


Figure 35: Comparison of the obtained STL files of the 3D surface scan (grey) and μ -CT (green). (A) Alignment of the two bones (B) Deviations greater than 0.5mm denoted by the red area and pins for selection of points in this area

Since the deviation of both structures was in the range of the image resolution and small compared to the overall dimension, only the μ -CT STL files were further progressed for 3D printing. The printing parameters were chosen according to Table 1 and 2 as discussed above, the g-code was exported and the bone was printed (Figure 36 A). Figure 36 A-B illustrates the final printing file of OBS and the outcome of the printing process, showing the inside of the final bone.

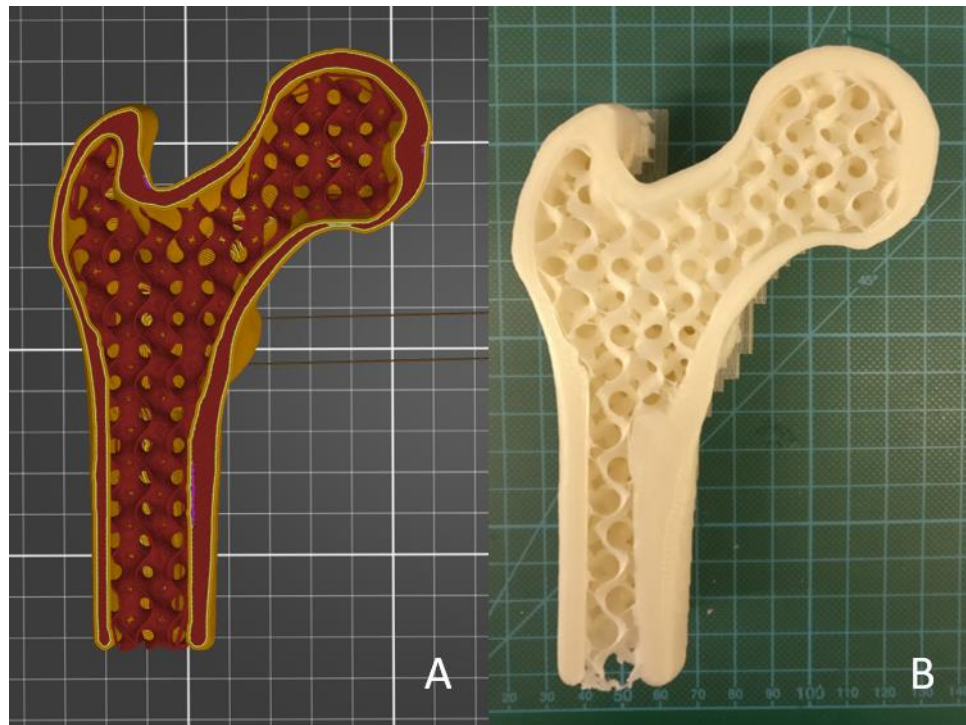


Figure 36: Infill show of OBS. (A) printing file in Prusa Slicer® (B) printed bone

The mechanical properties were then tested as described in chapter 6.7.2. In the case of OBS, two commercial artificial bones with the abbreviation of OBS_K and six printed bones (OBS_P) were examined in a compression test until failure. The resulting force-displacement curves are shown in Figure 37. For sample OBS_1P the embedding process failed thus the results are omitted in the further discussion. The determined structural properties can be seen in Table 3 below. An average stiffness of 1204 ± 338.5 N/mm and an ultimate force of 5446.8 ± 928.4 N was determined for the printed samples. The commercial artificial bones, an average stiffness of 306.8 ± 65.6 N/mm and an ultimate force of 1403.2 ± 112.4 N was determined.

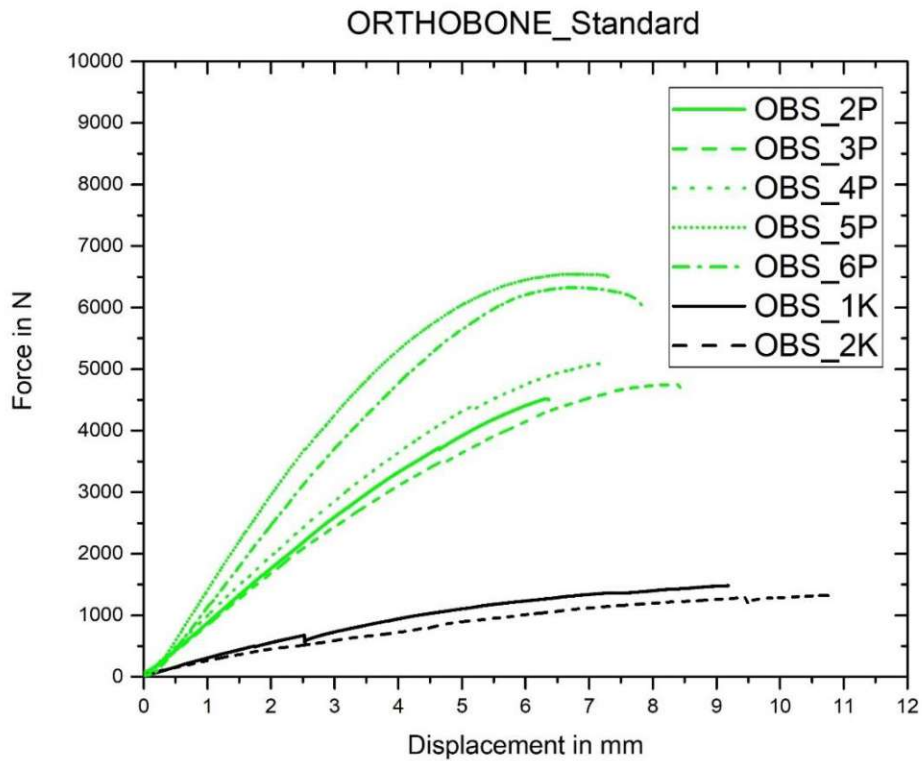


Figure 37: Force-Displacement curves of the ORTHOBone_Standard (OBS), printed (P) and artificial (K) samples

Table 3: Determined material characteristics for OBS

Sample	Force _{ult} in N	ORTHOBONE_Standard				
		Average	Standard Deviation	Stiffness in N/mm	Average	Standard Deviation
OBS_2P	4520.2			924.8		
OBS_3P	4752.7			922.9		
OBS_4P	5089.4	5446.8	928.4	1064	1204	338.5
OBS_5P	6543.8			1689.4		
OBS_6P	6327.9			1418.8		
OBS_1K	1482.6			353.2		
OBS_2K	1323.7	1403.2	112.4	260.4	306.8	65.6

Furthermore, the compression tests were recorded using a highspeed camera (PCO Dimax CS® from PCO AG,93309 Kelheim, Germany) and a sequence of the fracture pattern can be seen in Figure 38. The first image in this sequence shows the bone shortly before the first crack appeared. In the second image, a small crack below the femoral head is visible. The crack then propagates from the proximal area between femoral head and neck throughout the femoral neck until complete failure occurred.

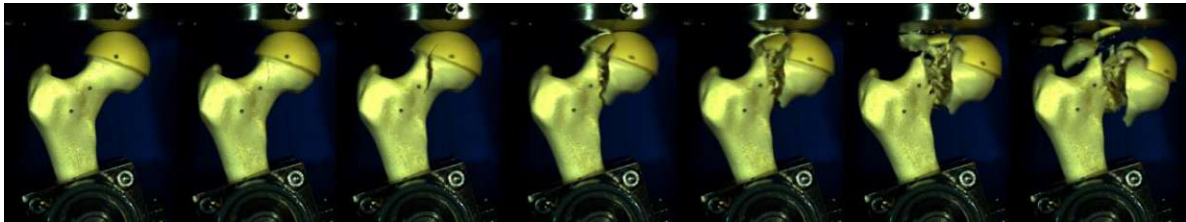


Figure 38: Fracture Pattern of OBS shown with OBS_6P

Additional Figure 39 shows an image of a printed OBS_6P sample before (Figure 39 A) and after (Figure 39 B) the mechanical testing procedure showing a fracture in the neck part, which is according to the AO/OTA fracture and dislocation classification of long-bone fractures¹⁰³ to be classified as 31B1 (subcapital femoral neck) . Furthermore, it shows the splitting of the femoral head due to the crack propagation shown in Figure 38 and its embedding on the distal end of the bone.

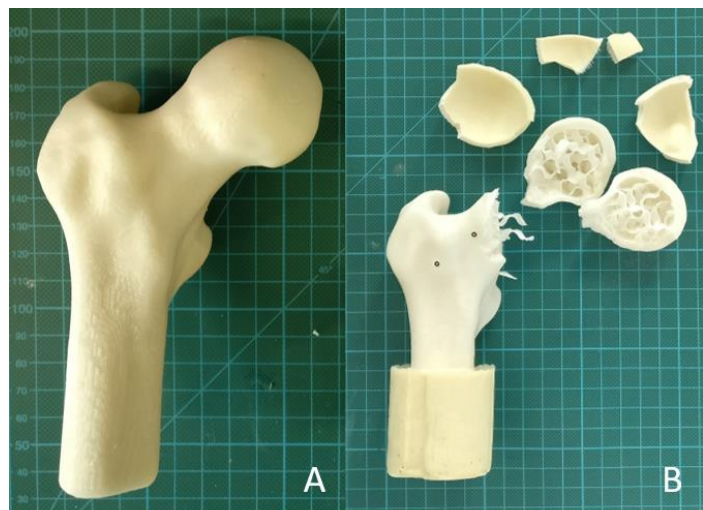


Figure 39: Printed OBS sample (A) before (B) after compression test

7.2 ORTHOBone

Since the ORTHOBone and ORTHOBone_standard were purchased from the same company, the geometries were assumed and proofed to be similar upon visual inspection. Thus, 3D surface scans and μ -CT structure analysis was only performed on one of the samples.

Judging by the fact that OB should have a better quality than the OBS concerning the mechanical properties, a higher infill density of 12% was chosen for the printing. The final g-code containing information about the bone (Figure 40 A) as well as the printed bone (Figure 40 B) showing the chosen parameters can be seen in Figure 40 below.

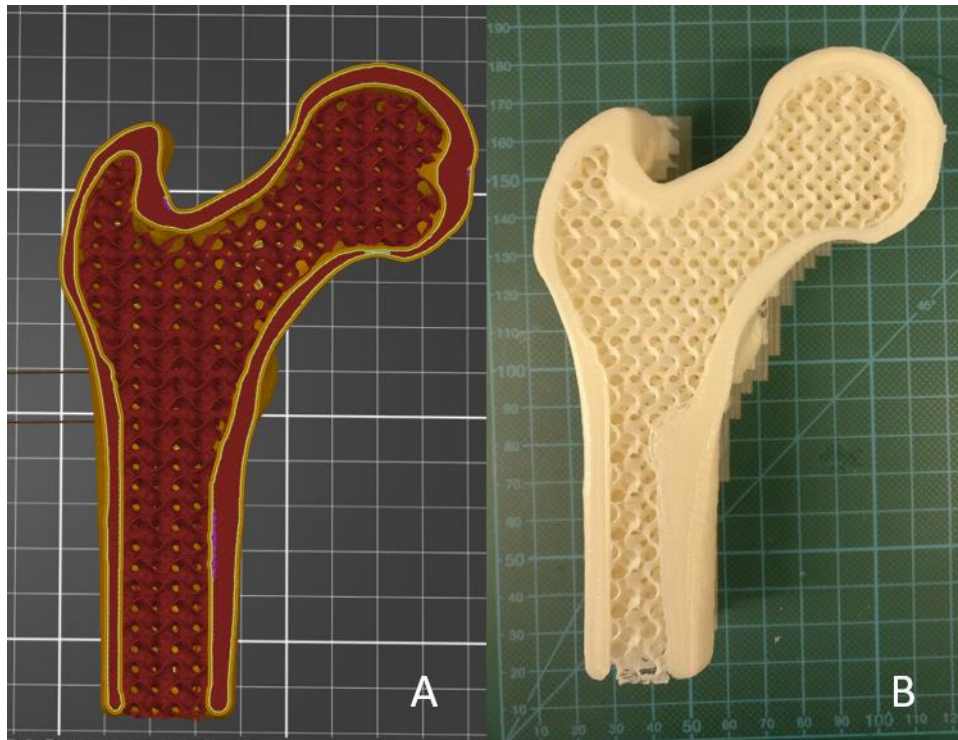


Figure 40: Infill show of OB. (A) printing file in Prusa Slicer® (B) printed bone

The bones were then tested as described in 6.7.2 mechanical testing. In the case of OBS, two artificial bones with the abbreviation of OB_K and four printed bones (OB_P) were tested. Figure 41 below, shows the obtained force-displacement curves and in Table 4 the determined material properties are summed up. The artificial bones did withstand an ultimate force of 2470.3 ± 268.5 N as opposed to the

printed bones with an ultimate force of 6230.6 ± 586.7 N. The results of the determined stiffness are 1422.3 ± 271.1 N/mm for printed bones and 996.6 ± 145.5 N/mm for the artificial once.

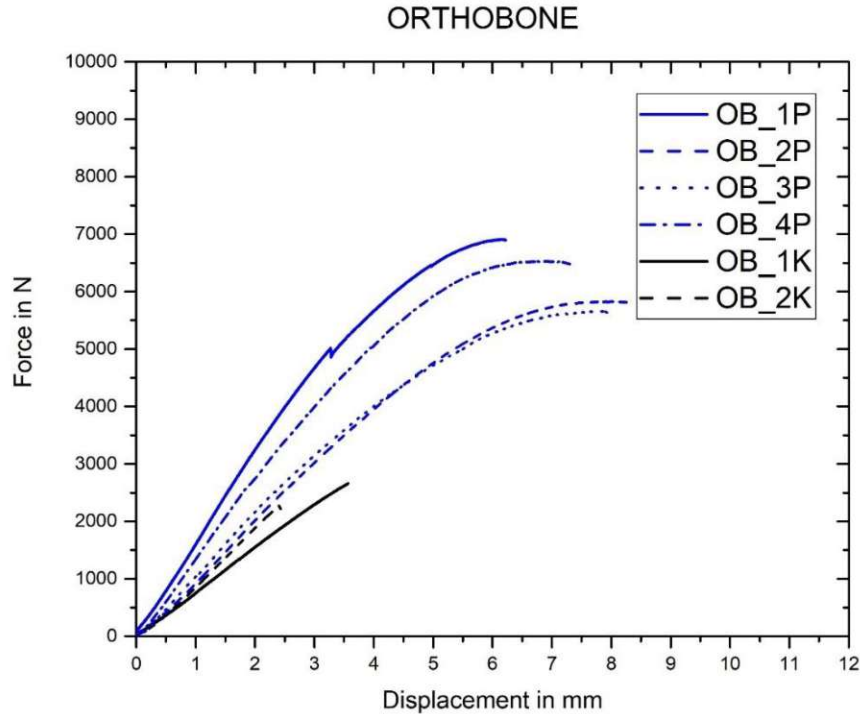


Figure 41: Force-Displacement curves of the ORTHOBone (OB), printed (P) and artificial (K) samples

Table 4: Determined material characteristics for OB

ORTHOBONE						
Sample	Force _{ult} in N	Average	Standard Deviation	Stiffness in N/mm	Average	Standard Deviation
OB_1P	6907.5	6230.6	586.7	1739.5	1422.3	272.1
OB_2P	5827.2			1148.9		
OB_3P	5661.2			1249.3		
OB_4P	6526.3			1551.7		
OB_1K	2660.1	2470.3	268.5	893.8	996.6	145.5
OB_2K	2280.4			1099.5		

Similar to the OBS sample the fracture tests of OB_3P and OB_4P were filmed with a highspeed camera (PCO Dimax CS[®] from PCO AG,93309 Kelheim, Germany). Figure 42 shows the fracture pattern observed during the compression test of OB_4P. Since OB_4P was filmed with a lower frame rate, the crack propagation is less detailed than the one of OBS_6P. The second picture in the sequence shown in Figure 42 shows that the crack started approximately in the middle of the femoral head. This crack then propagated through the femoral head until failure occurred and the head teared off. The compression test of OB_4P resulted in the fracture pattern shown in Figure 43 B. Furthermore, Figure 43 A shows the printed bone before testing. Despite the crack propagation initially starting at the femoral head, the 3D printed bone shows a fracture pattern at the femoral neck (classified as 31B1¹⁰³).

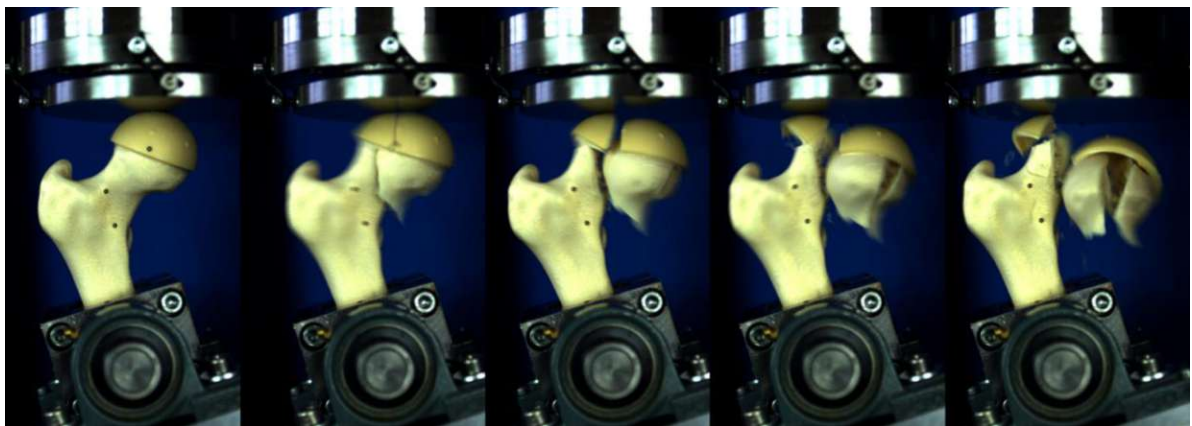


Figure 42: Fracture Pattern of OB shown with OB_4P



Figure 43: Printed OB sample (A) before (B) after compression test

7.3 SYN BONE®

SYNBONE® and ORTHOBones are both PU based bones, but they differ in their geometry. SYN shows more rough edges compared to the OBS and OBS sample and additionally has a thicker femoral neck. Furthermore, the foam representing the spongiosa differs to the one of OBS concerning the *E*-modulus, but has almost the same compared to the premium bone (OB). This fact is interesting, since the SYN bone cost less compared to the OB (12€ compared to 40€).

A segmentation of the obtained μ -CT was necessary to export STL files of the spongiosa and cortex of the artificial SYN BONE®. The results of segmentation process are shown in Figure 44 A-D.

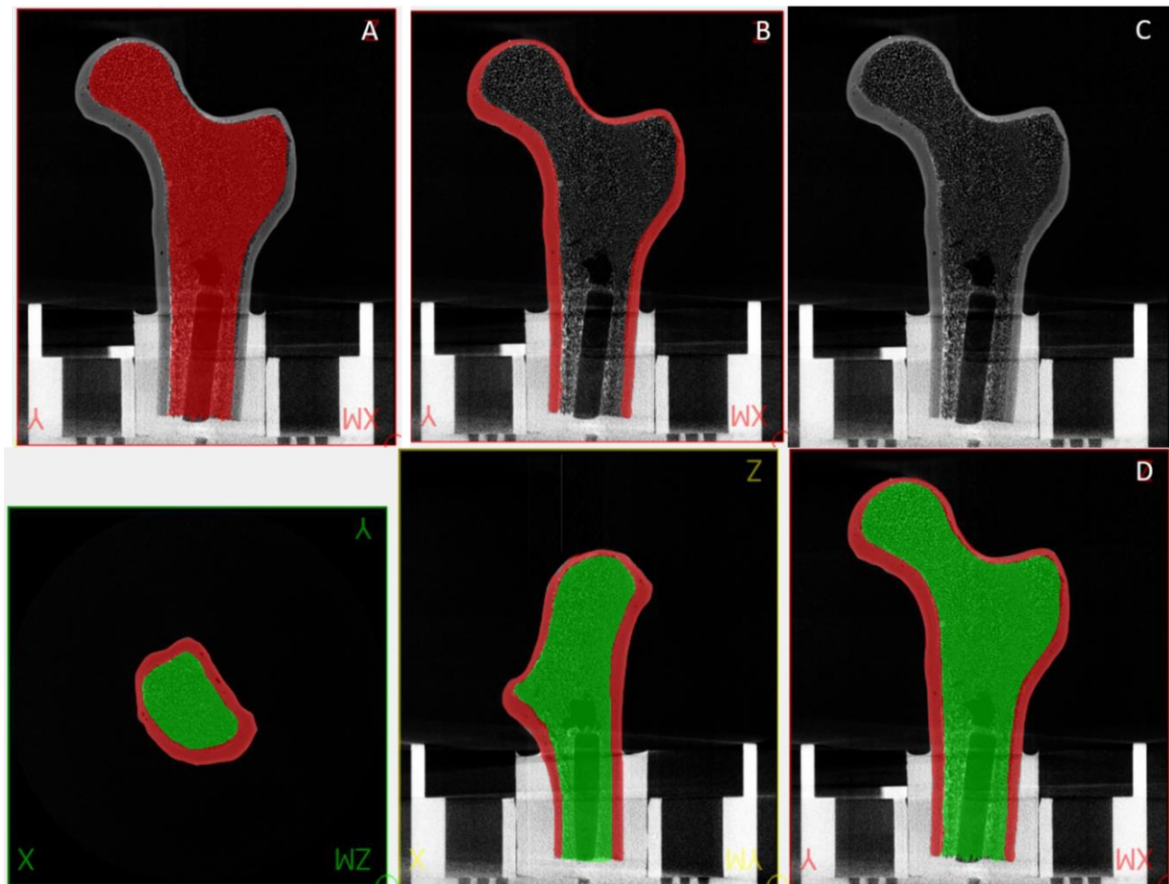


Figure 44: Segmentation of SYN (A) segmented spongiosa (B) segmented cortex (c) midplane without segmented region (D) segmented spongiosa and cortex shown on the original midplane output in different direction in space

The obtained STL file of the segmentation shown above was compared to the STL of the 3D surface scan and the result is shown in Figure 45. The grey area in Figure 45 A represents the 3D surface scan while the μ -CT STL is shown in green.

In Figure 45 B the red area indicates deviation greater than 0.5mm. The pins are automatically created by Meshmixer 3.5® (Autodesk GmbH, 81379 Munich, German) to simplify further work with the deviated areas.

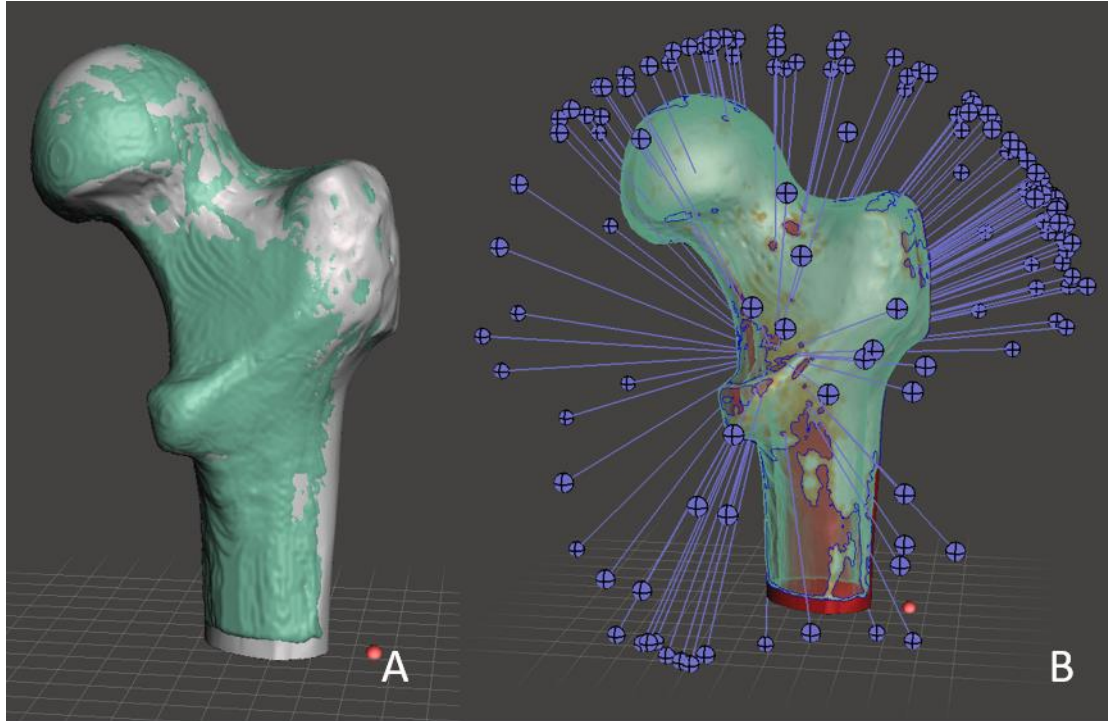


Figure 45: Comparison of the obtained STL files of the 3D surface scan (grey) and μ -CT (green). (A) Alignment of the two bones(B) Deviations greater than 0.5mm denoted by the red area and pins for selection of points in this area

Judging by the minor deviations in the two STL files only the ones obtained *via* μ -CT were used for the 3D printing process. The printing parameter were adapted according to chapter 6.6.2 Slicing and Printing Parameters with an infill density of 12%, the g-code exported and the bone was printed as shown in Figure 46 below.

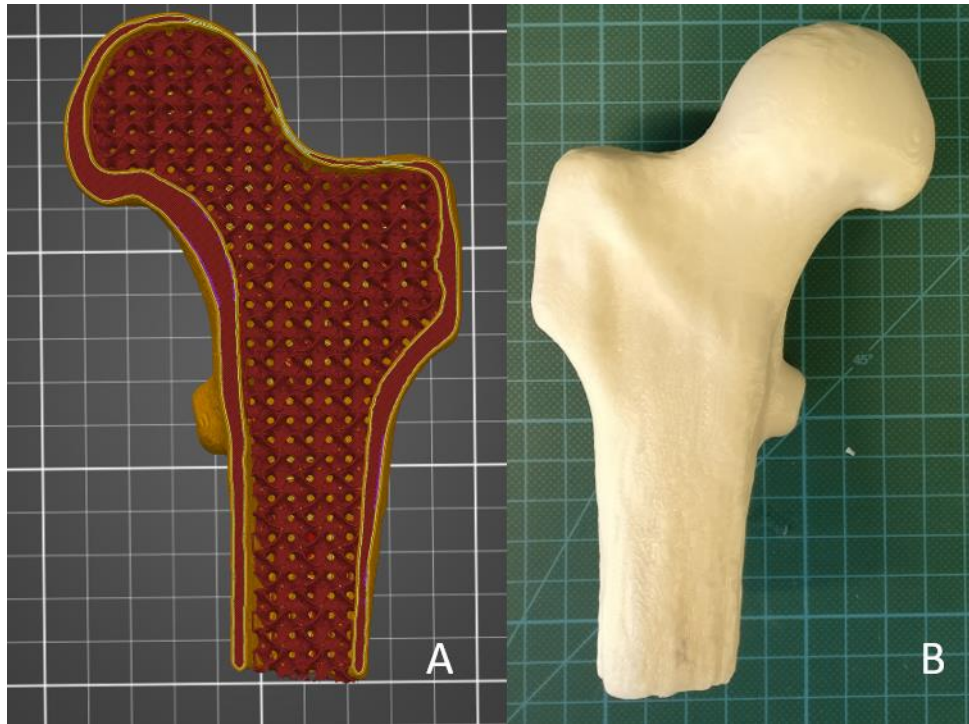


Figure 46: Printing of SYNSTONE® (A) exported g-code (B) printed bone

After embedding, the compression tests were performed. In the case of SYNSTONE®, four printed bones (SYN_P) and two artificial bones (SYN_K) were tested. The determined values of the ultimate Force F_{ult} and stiffness S are summed up in the Table 5. The artificial bones did withstand an ultimate force of 3144.3 ± 174.3 N and had a stiffness of 635.3 ± 12.8 N/mm. For the printed bones a stiffness of 1800.1 ± 231.9 N/mm and an ultimate force of 7137.9 ± 1521.5 N were determined. The obtained force-displacement curves can be seen in Figure 47 below.

Table 5: Determined material characteristics of SYNBONE®

Sample	Force _{Ult} in N	SYNBONE				
		Average	Standard Deviation	Stiffness in N/mm	Average	Standard Deviation
SYN_1P	5780.8	7137.9	1521.5	1752	1800.1	231.9
SYN_2P	6055.8			1740.2		
SYN_3P	7665.8			1580.6		
SYN_4P	9049.3			2127.7		
SYN_1K	3021.1	3144.3	174.3	626.3	635.3	12.8
SYN_2K	3267.5			644.4		

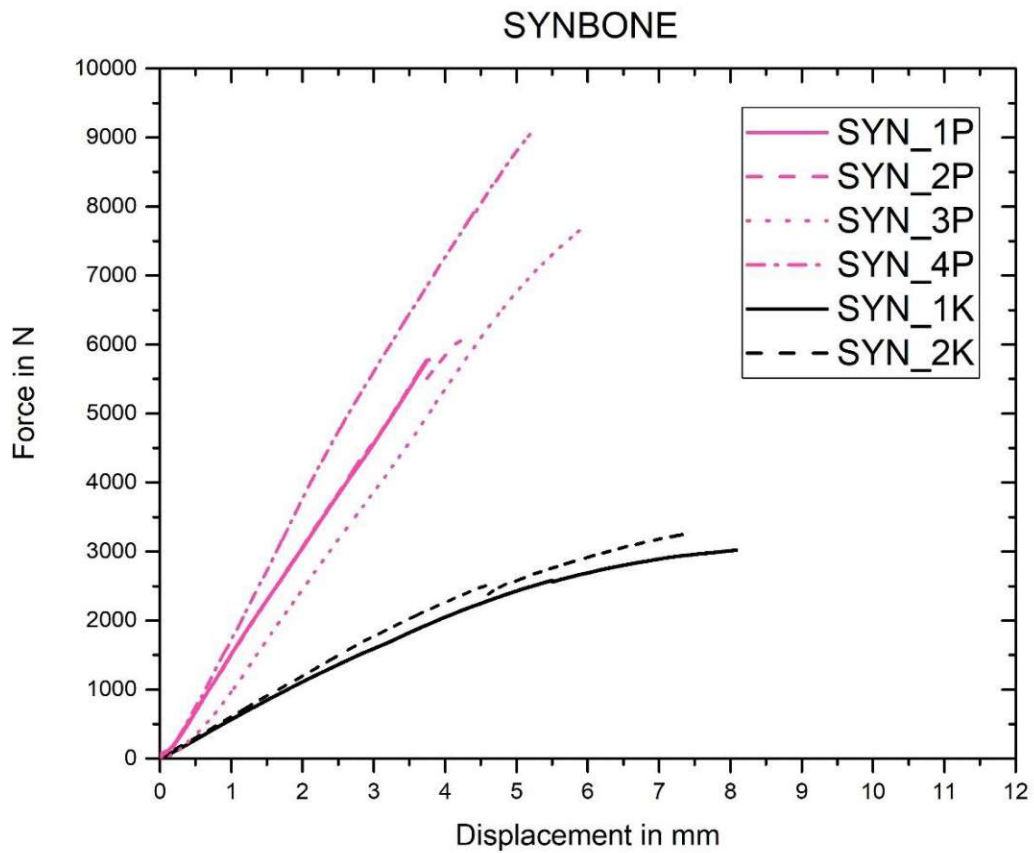


Figure 47: Force-Displacement curves of the SYNBONE® (SYN), printed (P), and artificial (K) samples

The compression test of SYN_3P and SYN_4P were recorded with a highspeed camera (PCO Dimax CS® from PCO AG,93309 Kelheim, Germany), the recorded fracture pattern is displayed in Figure 48. The crack started at the femoral head most likely due to the thinner cortex. It propagated through the head and a half broke off, but unlike the OBS and OB samples, no fracture pattern at the femoral neck was observed (Figure 49 B). Instead the head was split (classification: 31C1¹⁰³) Also, a comparison of the printed bone before (Figure 49 A) and after (Figure 49 B) applying load was made.

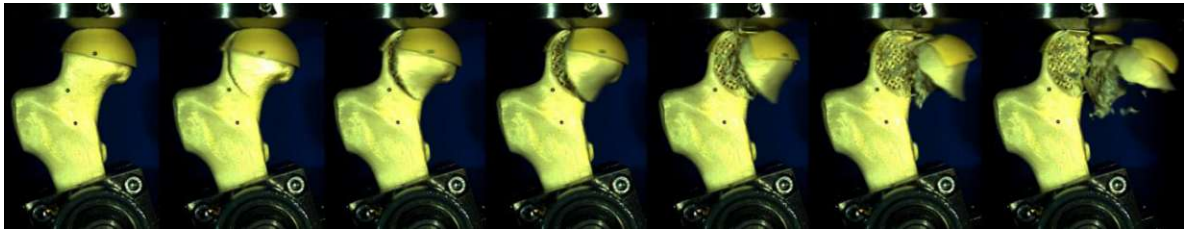


Figure 48: Fracture pattern of SYNBONE® shown with SYN_3P

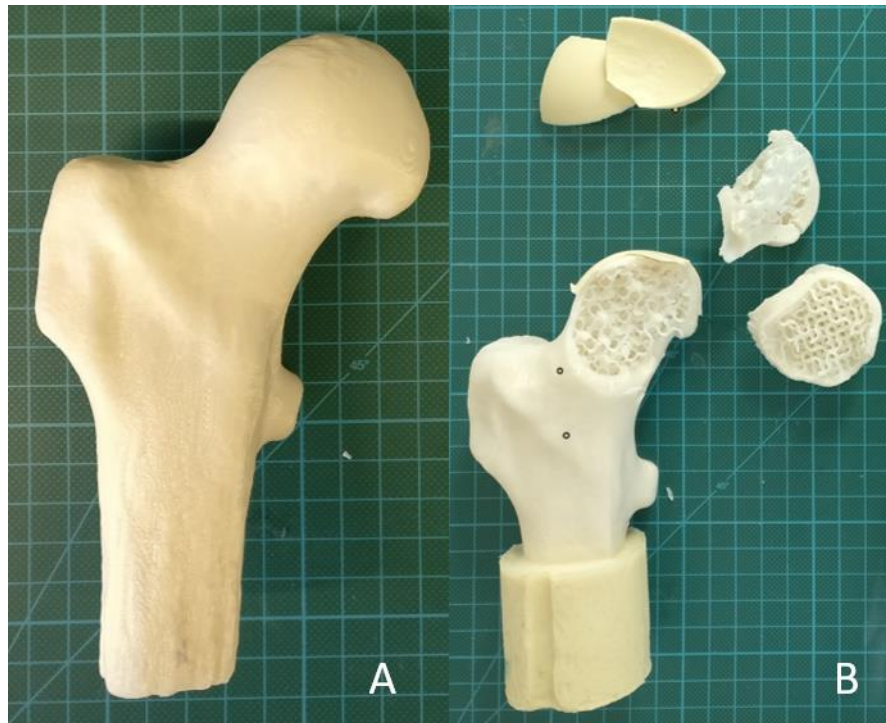


Figure 49: Printed SYN sample (A) before (B) after compression test

7.4 SAWBONE[®]

SAWBONES[®] consists of a composite material. Making it easier to differentiate between cortex and spongiosa in the μ -CT scan. Figure 50 A represents the segmented spongiosa, while Figure 50 B shows the segmented cortex. An overlay of spongiosa and cortex with the original midplanes is shown in Figure 50 D below.

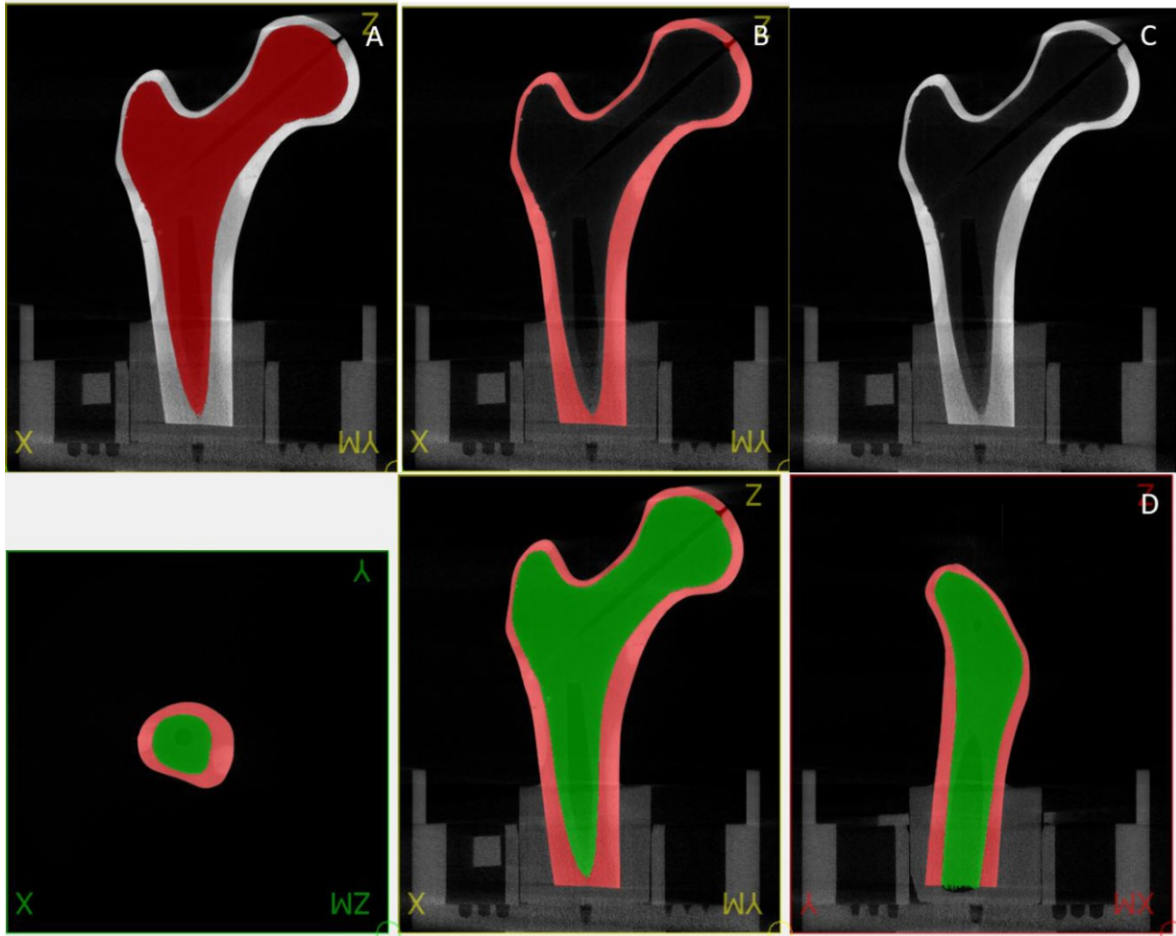


Figure 50: Segmenting of SAW (A) segmented spongiosa (B) segmented cortex (C) midplane without segmented region (D) segmented spongiosa and cortex shown on the original midplane output in different direction in space

The comparison of the surfaces of STL files and μ -CT are shown in Figure 51. The green area in Figure 51 A shows the obtained STL file of the μ -CT, while grey is associated with the 3D surface scan. The red area in Figure 51 B indicates a deviation greater than 0.5 mm after the alignment iterations and the pins are created by Meshmixer 3.5[®] (Autodesk GmbH, 81379 Munich, German) automatically for simplification of further progressing of the deviations.

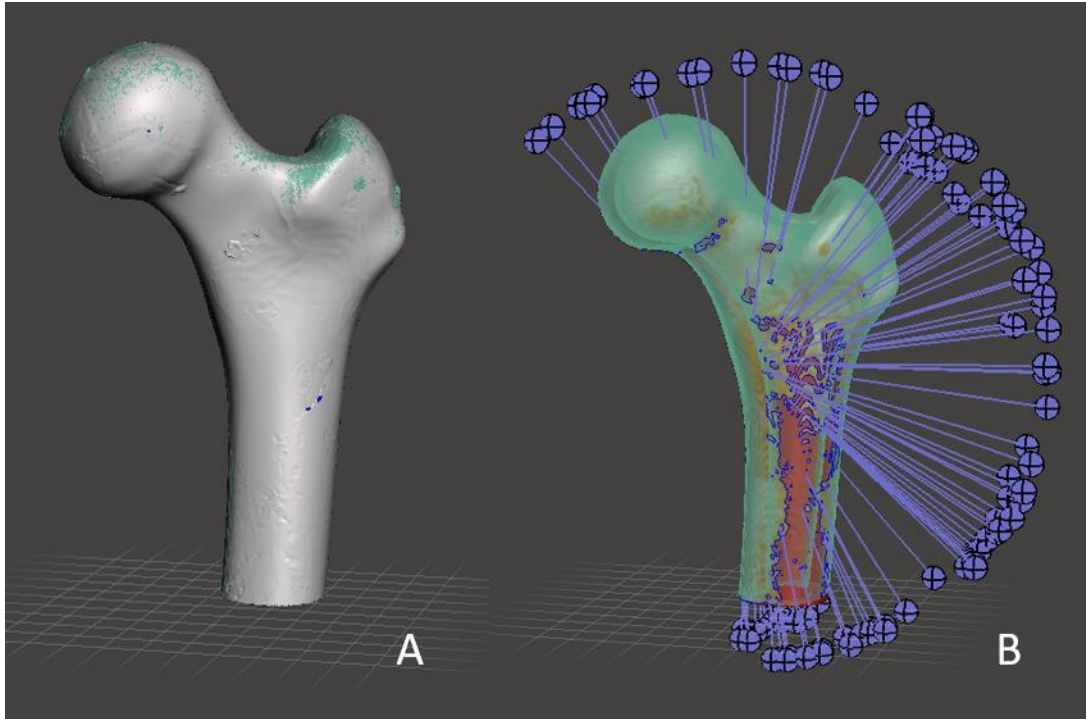


Figure 51: Comparison of the obtained STL files of the 3D surface scan (grey) and μ -CT (green). (A) Alignment of the two bones (B) Deviations greater than 0.5mm denoted by the red area and pins for selection of points in this area

By obtaining the STL files after the segmentation of the μ -CT image and setting the printing parameters the bone was ready to be printed. For the spongiosa an infill density of 27% was chosen according to chapter 6.6.2 Infill Density Estimation and can be seen in Figure 52 A. This Figure 52 also shows an example of the printed SAWBONE[®] (Figure 52 B).

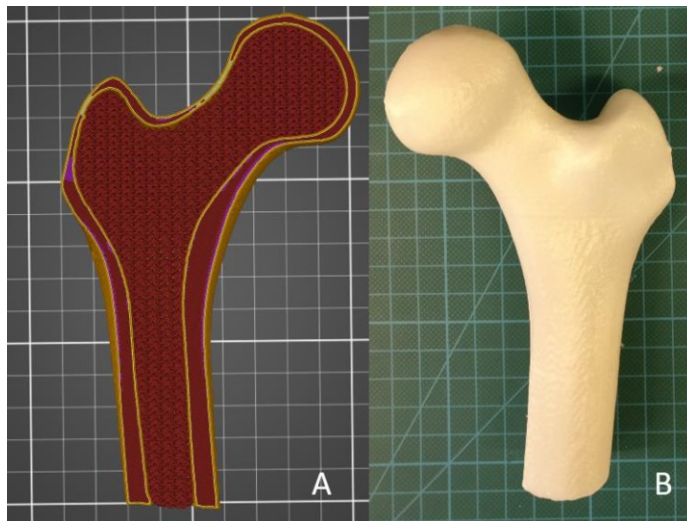


Figure 52: Printing of SAW (A) exported g-code (B) printed bone

After embedding the printed bones according to chapter 7.7.1 Embedding the compression test were performed. In the case of SAWBONE[®] one artificial bone (SAW_K) and three printed bones (SAW_P) were tested and the material characteristics were determined (Table 6). In the case of the printed bones an ultimate force of 7405.9 ± 132.9 N and an average stiffness of 1920.1 ± 137.3 N/mm was obtained. The one artificial bone had a stiffness of 3127.5 N/mm and could withstand an ultimate force of 9119.3 N. Furthermore, the recorded force-displacement curves of SAW samples can be seen in Figure 53 below.

Table 6: Determined material characteristics of SAWBONE[®]

SAWBONE						
Sample	Force _{ult} in N	Average	Standard Deviation	Stiffness in N/mm	Average	Standard Deviation
SAW_1P	7339.3			1774.8		
SAW_2P	7559.0	7405.9	132.9	2047.9	1920.1	137.3
SAW_3P	7319.4			1937.5		
SAW_1K	9119.3			3127.5		

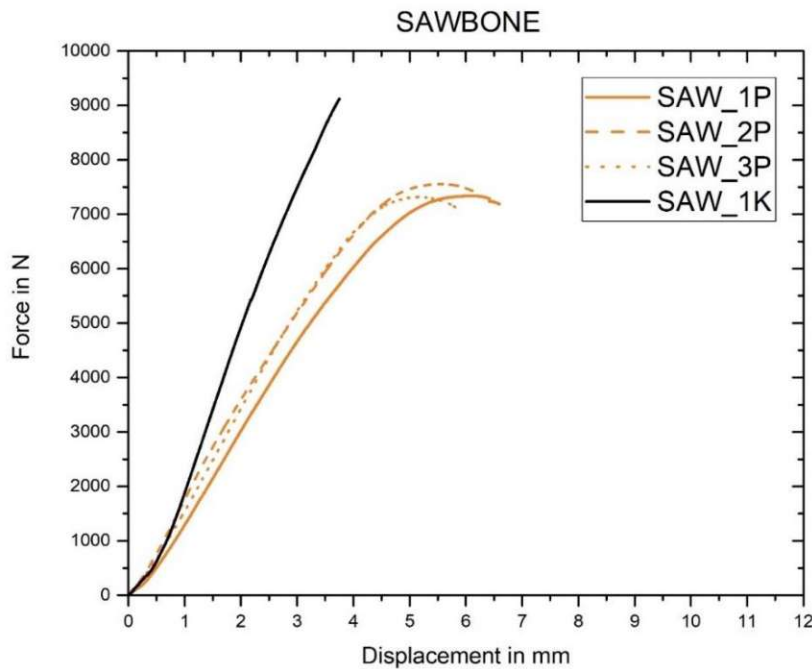


Figure 53: Force-Displacement curves of the SAWBONE[®] (SAW), printed (P), and artificial (K) samples

SAW_3P was filmed with a highspeed camera but only the obtained video was saved. That's why Figure 54 shows only one sample before applying load and after failure and not a sequence of the fracture pattern. Figure 54 shows that the 3D printed bone failed at the femoral neck (classification: 31B1), but also the femoral head broke down into two parts (classification: 31C1)¹⁰³.

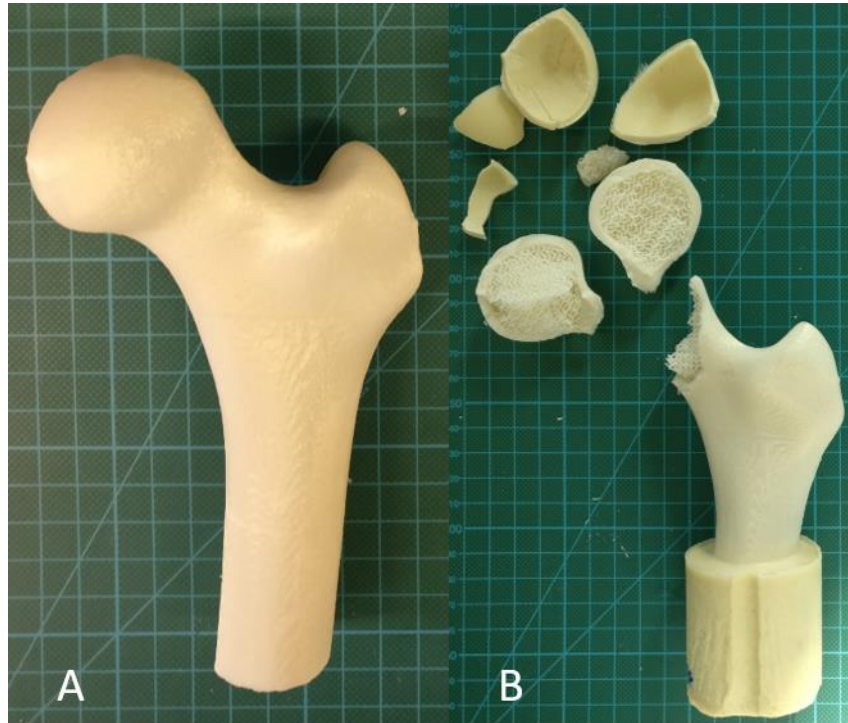


Figure 54: Printed SAW sample (A) before (B) after compression test

7.5 Artificial Bones

Furthermore, the purchased artificial bones were compared to each other concerning their mechanical behaviour during the compression test. Figure 55 shows the average force-displacement curves of the artificial bones, OBS (green), OB (blue), SYN (pink) and SAW (orange) and their standard deviations are denoted by the transparent areas.

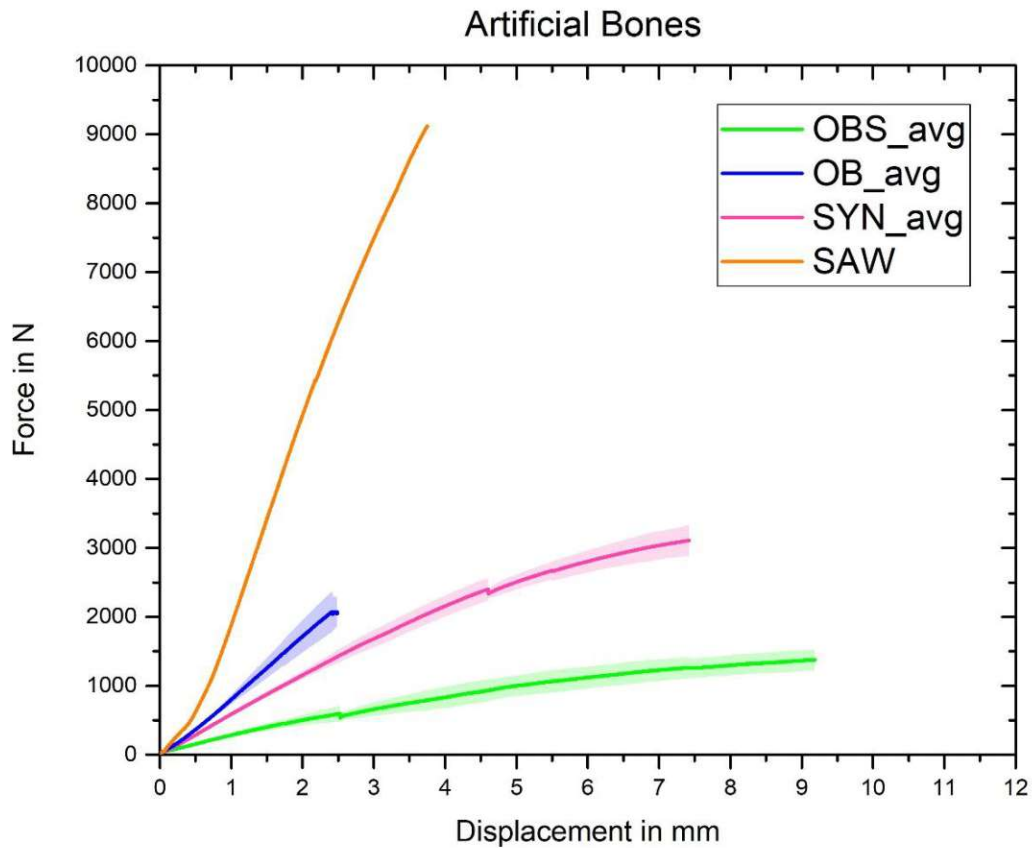


Figure 55: Average Force-Displacement curves of the artificial (K) bones and their standard deviation. (OBS...ORTHOBone_Standard, OB...ORTHOBone, SYN...SYNBONE®, SAW...SAWBONE®)

A comparison of the obtained ultimate forces of the artificial bones is shown in Figure 56. Again, OBS is displayed with green, OB with blue, SYN with pink, and SAW with orange.

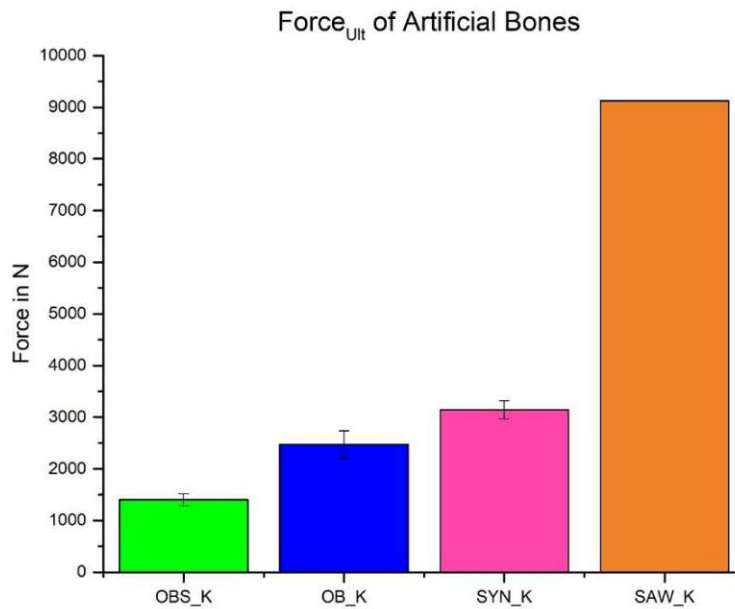


Figure 56: Ultimate Force of the artificial bones. (OBS...ORTHOBone_Standard, OB...ORTHOBone, SYN...SYNBONE®, SAW...SAWBONE®)

Also, the comparison of the obtained stiffnesses is of interest as shown in Figure 57.

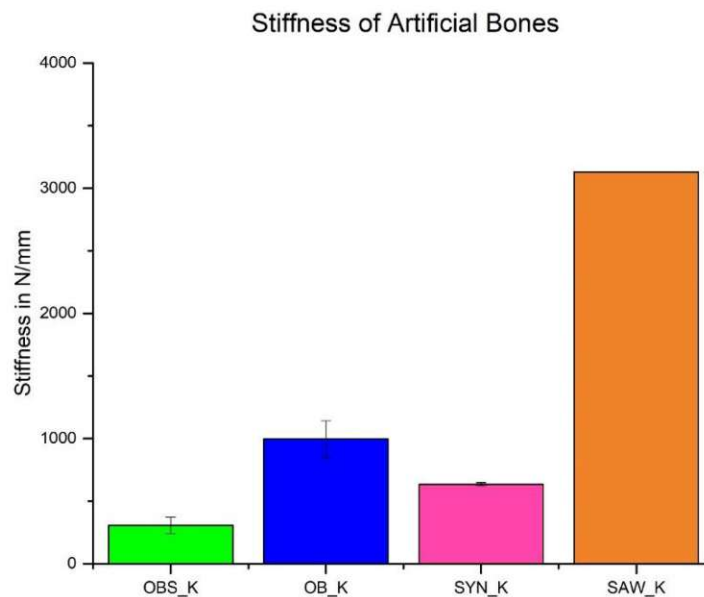


Figure 57: Stiffness of the artificial bones. (OBS...ORTHOBone_Standard, OB...ORTHOBone, SYN...SYNBONE®, SAW...SAWBONE®)

Despite the ultimate force and the stiffness of the samples, different fracture patterns were obtained as shown in Figure 58 below.



Figure 58: Fracture pattern of artificial bones. (A) OBS (B) OB (C) SYN (D) SAW

7.6 Printed Bones

Since not only the artificial bones were tested but also their 3D printed analogues, a comparison of the different bone groups was made. The obtained average force-displacement curves as their standard deviation denoted by the transparent area are shown in Figure 59 with OBS (green), OB (blue), SYN (pink) and SAW (orange).

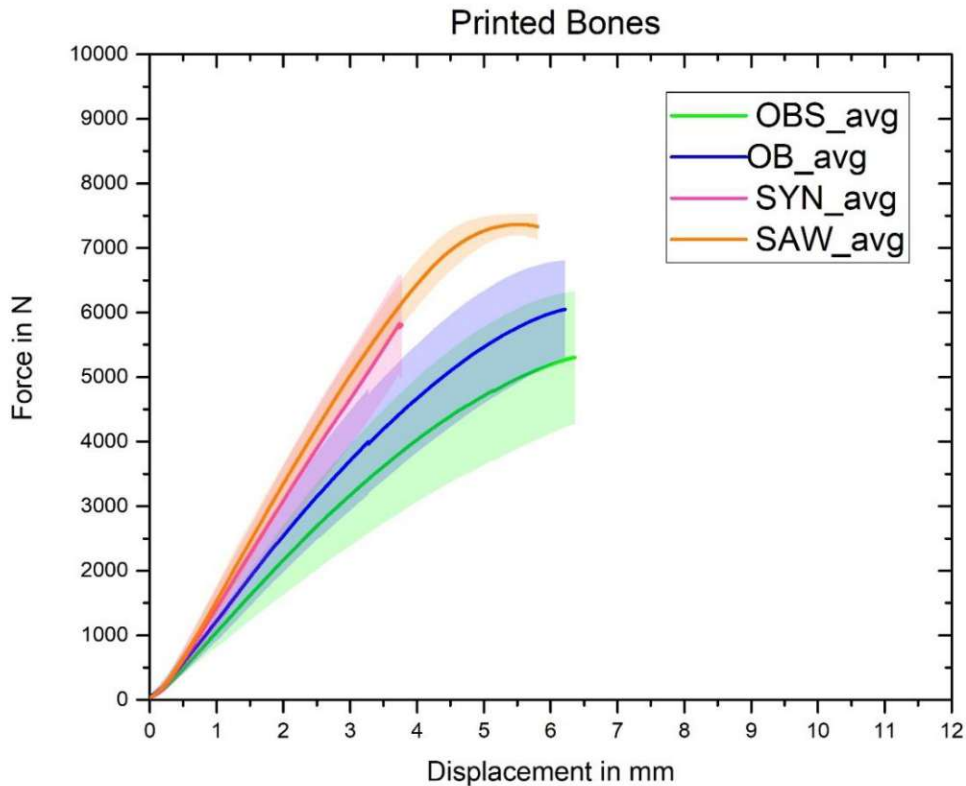


Figure 59: Average Force-Displacement curves of the printed bones. (OBS...ORTHOBone_Standard, OB...ORTHOBone, SYN...SYNBONE®, SAW...SAWBONE®) and their standard deviation.

In the same colours displaced as before (green...OBS, blue...OB, pink...SYN, and orange...SAW) are the obtained ultimate forces (Figure 60).

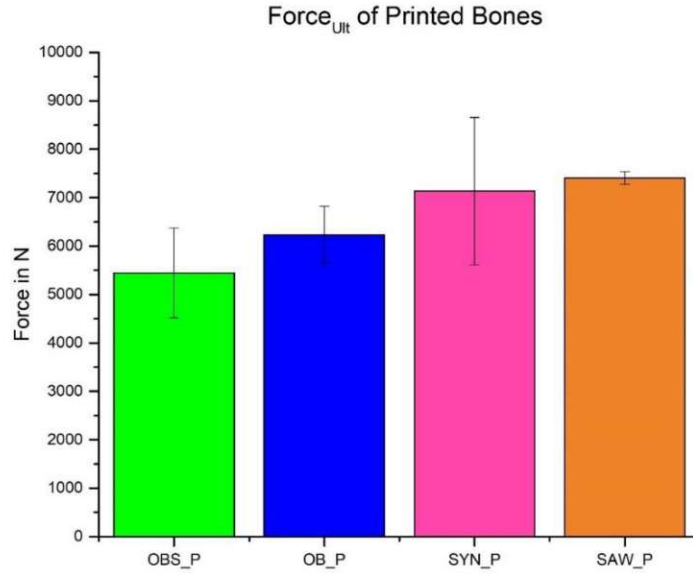


Figure 60: Ultimate Force of the printed bones. (OBS...ORTHOBone_Standard, OB...ORTHOBone, SYN...SYNBONE®, SAW...SAWBONE®)

The obtained stiffnesses are shown in Figure 61.

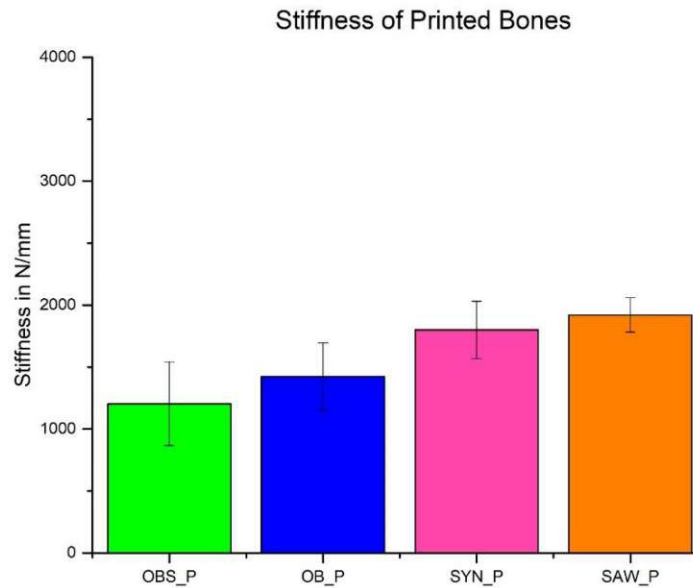


Figure 61: Stiffness of the printed bones. (OBS...ORTHOBone_Standard, OB...ORTHOBone, SYN...SYNBONE®, SAW...SAWBONE®)

The fracture patterns of the printed bones were also analysed and the resulting fracture patterns are shown in Figure 62.

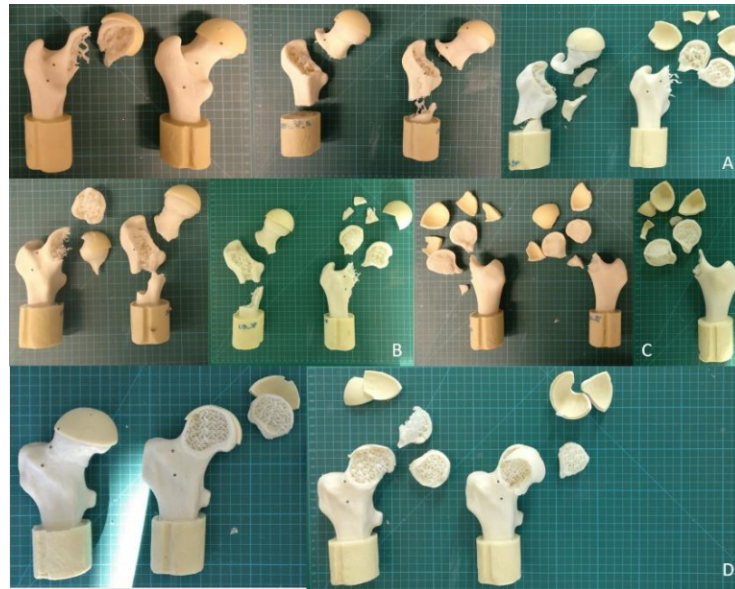


Figure 62: Fracture pattern of artificial bones. (A) OBS (B) OB (C) SAW (D) SYN

7.7 Comparison of Artificial and Printed Bones

To be able to compare the artificial bones with their printed counterpart also the ultimate forces are displayed in Figure 63. The same accounts for the obtained stiffness of all sample groups as shown in Figure 64.

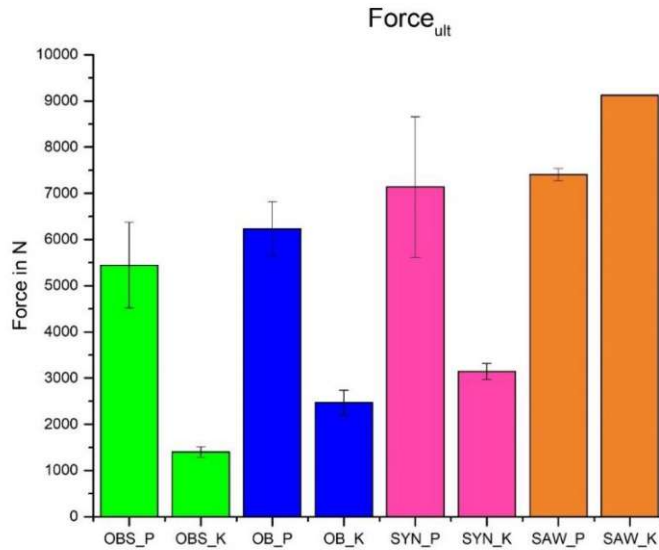


Figure 63: Comparison of the ultimate force of the printed (P) and artificial (K) bones. (OBS...ORTHOBone_Standard, OB...ORTHOBone, SYN...SYNBONE®, SAW...SAWBONE®)

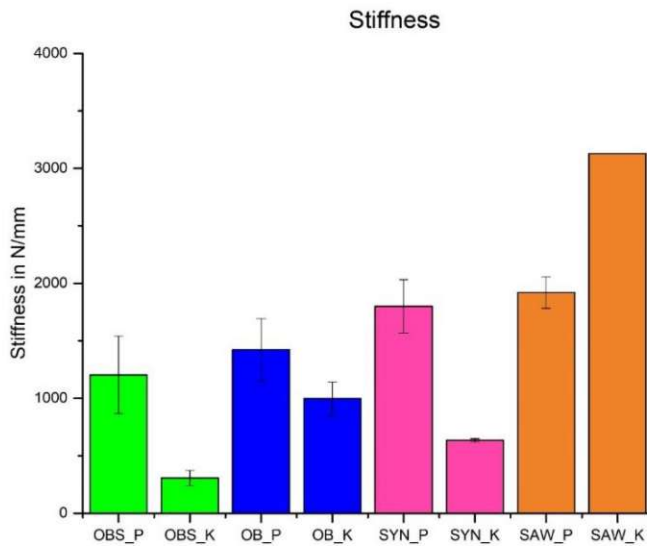


Figure 64: Comparison of Stiffness of the printed (P) and artificial (K) bones. (OBS...ORTHOBone_Standard, OB...ORTHOBone, SYN...SYNBONE®, SAW...SAWBONE®)

8 Discussion

The goal of this work was to compare artificial bones with their printed analogues with respect to mechanical stiffness and ultimate force. Artificial bones could be successfully printed and mechanically tested. The compression test to access the stiffness and ultimate force showed that the printed analogues outperformed their artificial counterpart except for the composite SAWBONE[®]. The advantage of 3D printed bones is that they are fast to manufacture, cheap, and could be used in patient specific applications in future.

8.1 3D Surface Scan versus μ -CT

Throughout every comparison of the 3D surface scan and the STL file of the cortex obtain from the segmentation of the μ -CT, it was not possible to perfectly align the femoral shaft. Despite tolerating the highest error tolerance and iteration number. However, as already shown by Brzobohatá *et al.* low deviations of the 3D surface scans and the μ -CT were identified¹⁰⁴.

The deviations of the OBS/ OB sample are the result of 3D surface scan being able to displace more structural details while this is neglected in the segmentation of the μ -CT (Figure 35). Due to its rougher edges (Figure 15) less deviations around the head and greater trochanter were recognized for the SYN sample. Despite the expectation of higher deviations in the femoral head regions due to the manual segmentation of the thin cortex, almost no red areas are shown in Figure 45. The SAWBONE[®] showed rudimentary surface details compared to the other artificial bones, resulting in less deviations between the 3D surface scan and the μ -CT STL file.

The low deviations (< 1 mm) between the obtained STL files through 3D surface scan and μ -CT resulted in the decision to only print the STL files obtained due to segmentation of the μ -CT. Because they contain information about thickness of the cortex and spongiosa, while the more structural details showing off in the 3D surface scans are negligible for biomechanical testing.

However, 3D surface scans are a fast alternative to μ -CT if bones are printed with a constant cortical thickness and constant infill.

8.2 Artificial Bones

In this master thesis, four different artificial bones were purchased. They did not only vary in geometry (except for OBS and OB due to the same manufacturer), surface details and foam filling, but also in the cortex and spongiosa geometry. Furthermore, the SAW sample does not consist of polyurethane like OBS, OB and SYN do, it is a composite bone. All these differences led to different mechanical behaviour as discussed in the following.

The comparison of the two types of artificial bones from 3B Scientific GmbH, (OBS and OB) shows that OBS has a larger displacement at failure compared to OB. A reason for this behaviour could be the different mechanical properties of the foam used as a representation for the spongiosa. In the case of OBS an average E -modulus of 9.06 ± 0.41 MPa was observed in the foam. In contrast to the average E -modulus determined for the OB foam of 35.6 ± 12.07 MPa making the bone stiffer. Despite having almost the same foam characteristics, samples of SYN could withstand more displacement than OB but less than OBS. OB and SAW seem to endure almost the same displacement at fracture, which is interesting because they have not only different geometries but were also manufactured from different materials.

It was clearly observed that the composite bone (SAW) could withstand much larger loads than the other artificial bones (Figure 56) made out of polyurethane (PU). SAW could withstand three times more force (9119.3 N) than SYN (3144.3 ± 174.3 N) and OB (2470.3 ± 268.5 N). Compared with the ultimate force of OBS (1403.2 ± 112.4 N) it is even six times higher. The ultimate force obtained for SAW was also in the expected range (5528-11109 N) found by previous work of Nicayenzi *et al.*¹⁰⁵

A comparison of the OBS and OB shows that the latter one endures around 1000 N more load before fracture occurs. Since these two bones share the same geometry, this effect can only be attributed to the different foam fillings.

With OB and SYN having mechanical similar performing foams as spongiosa they clearly differed in ultimate force. SYN did withstand a much higher load (~1 kN) before fracturing as compared to OB which is most likely related to the difference in cortex thickness or the embedding.

Concerning the stiffnesses of the artificial bones (Figure 57) it can be assumed that the cortical thickness has to play a major role. When comparing the results of SYN and OB it can be observed that SYN has a ~33% lower average stiffness than OB (635.3 ± 12.8 N/mm compared to 996.6 ± 145.4 N/mm) despite their respective foams having similar mechanical properties. Such a drop in stiffness was only witnessed when the ratio of cortical wall thickness drops by 50%, as shown by Zdero *et al.*¹⁰⁶ When comparing the cortical thickness of the femoral head for the SYN (Figure 49) to the OB sample (Figure 43) using the pictures taken after fracture, one can observe that the SYN sample is only half as thick as the OB sample in this region.

Furthermore, OB (the premium bone of 3B Scientific GmbH, 20459 Hamburg Germany) is even three times stiffer compared to the cheaper OBS sample (306.8 ± 65.6 N/mm compared to 996.6 ± 145.4 N/mm) indicating that higher price indeed changes the quality of the artificial bone.

Again, the SAWBONE® outperforms not only the other artificial bones tested by achieving the highest average stiffness of 3127.5 N/mm, but also previous tested SAWBONES® by Zdero *et al.* (stiffness of 1742.7 ± 174.7 N/mm)¹⁰⁷ and Nicayenzi *et al.* having a stiffness between 2117-2531 N/mm.¹⁰⁵ The lower stiffness obtained by Nicayenzi *et al.* could be a result from the different angle chosen to simulate stance position (15°)¹⁰⁵ in comparison to 20° chosen in this thesis, but also from different sample preparation.

The artificial bones were designed to mimic natural bones in their mechanical behaviour thus similar fracture patterns should be expected. Fracture of the femur is especially prominent in elderly people and the two most common ones are intertrochanteric fracture^{50, 108} and a fracture occurring on the femoral neck¹⁰⁸.

As shown in Figure 62 D, SAW fractures at the trochanteric region just like OBS (Figure 62 A) and the OB (Figure 62 B) bones, which can be classified according to the AO/OTA fracture and dislocation classification of long-bone fractures¹⁰³, as a 31A3 fracture. SYN (Figure 62 C) mimics the fracture of the femoral neck in both samples tested, classifying as a fracture 31B3 (basicervical).

8.3 Printed Bones

The printed bones are based on the segmentation of the μ -CT of their artificial counterparts. The difference of the geometries also applies within the printed sample groups. Furthermore, due to different quality of the foam filling, which represents the spongiosa, different infill densities were chosen. Unlike the artificial bones, all printed bones consist of the same material (PLA). Therefore, differences in mechanical behaviour due to different material was eliminated.

It could be observed that every sample of OBS withstands almost the same displacement before fracturing. Only the force where fracture occurred seems to be divided into two groups. One being around 4800 N (OBS_2P, OBS_3P and OBS_4P) and a second withstanding around 6400 N (OBS_5P and OBS_6P). The relative high deviation in ultimate force (Figure 60) might be a result of using different filament rolls and being printed at different days. Because similar changes in the mechanical performance was observed within the other sample groups. Also, the fact, that machine displacements were measured plays a key role in the different behaviour of the samples, since they are influenced by the embedding process too. Despite performing the embedding process to the best of knowledge, small changes during the stirring process of the resin and concrete placement of the femurs in the embedding device could not be prevented.

SYN_4P performed the best in compression test, even when compared to the artificial SAW_1K (Figure 55). Unfortunately, this was not due to better geometry or infill density, but simply by having a thicker femoral head embedding than the rest. With respect to ultimate force, the thicker head embedding also explains the high standard deviation of SYN (pink) in Figure 60 below. This raises the average ultimate force by $\sim 10\%$ from 6500.8 ± 1018.3 N without SYN_4P up to 7137.9 ± 1521.5 N

including SYN_4P. By the raised value the sample group of SYN performed almost the same as the SAW (7405.9 ± 132.9 N), which unlike the artificial bones did not stand out. OB samples did withstand similar ultimate forces as SYN did (Figure 60), when neglecting SYN_4P, with an average of 6230.6 ± 586.7 N. That was to be expected since the samples have the same infill density of 12% while only varying in geometry. Whereas, the comparison of OB and OBS (Figure 60) shows that the geometry difference can be neglected due to sharing the same. The infill density seems to have a greater influence on failure load¹⁰⁵ than geometry. OBS has an infill density of only 7% compared to 12% of OB and withstands ~ 1 kN less force before fracturing (OBS: 5446.8 ± 928.4 N, OB: 6230.6 ± 586.7 N). As already stated by Nicayenzi *et al.* the density of the cancellous bone does not influence the stiffness as much as the fracture force of synthetic femurs¹⁰⁵. This fact is shown in Figure 61, when looking at OBS (green), OB (blue), SYN (pink) and SAW (orange). Despite varying in infill density from 7-27%, the stiffness is almost the same.

The high standard deviation of OBS (1204 ± 338.5 N/mm) in Figure 61 could be due to OBS_5P and OBS_6P, which were printed using a different PLA roll. Neglecting the two samples, OBS would have an average stiffness of 970.5 ± 80.9 N/mm, which is ~ 300 N/mm lower. The deviation of this sample can only be traced back to the embedding process and different PLA rolls used. Unlike expected, due to thinner cortex of the femoral head, SYN showed a higher stiffness (1800.1 ± 231.9 N/mm) than OB (1422.3 ± 272.1 N/mm). This observation could be traced back to the thicker head embedding of SYN_4P. Excluding the stiffness of SYN_4P an average stiffness of 1690.9 ± 95.7 N/mm was obtained. This shows that SYN and OB almost have the same stiffness when errors of the embedding process are excluded. The diameter of the femoral neck of the SYN is higher than the one of OB, which results in higher stiffness of 200 N/mm, despite the thinner cortex at the femoral head. Furthermore, the geometry of the femur seems to have a minor impact on stiffness, since all three different bone geometries have an average stiffness between 1200-1900 N/mm.

Apparently, the geometry played a role in fracture pattern, since all three different geometries showed different fracture behavior (Figure 62). Two fracture sites were recognized for OBS and OB (Figure 62 A and B), one at the femoral shaft and the second at the neck, classifying as fractures of the type 31A2 and 31B3 (OBS). The thinner cortex at the femoral head plays a role in the fracturing process, since it was clearly visible that the bones burst first at the thinnest part (Figure 62 D), without breaking the neck (classification: 31C1). Only samples of SAW showed the expected fracture at the femoral neck (classification: 31B2¹⁰³), but also the head busted in two parts, which would be classified as a splitting of the femoral head (31C1¹⁰³) (Figure 62 C). However, all fracture modes had a natural appearance, and no layer splitting was seen due to the direction of printing.

Furthermore, Figure 63 shows the same trend in F_{ult} for artificial and printed bones by showing an increase of F_{ult} from the OBS samples to the SAW samples. This indicates similar strength of the polymers PLA and PU. Also, the stiffness shown in Figure 64 correlated except for SYN_K presumably due to the design of the cortex in the femoral head region. This indicates different stiffness of the bulk materials.

8.4 Comparison of Artificial and Printed Bones

By comparing the fracture pattern of the artificial bones (Figure 58) and the printed once (Figure 62) it can be stated that they do not have the same fracture pattern. Only the sample of OBS and OB show a similar failure at the femoral shaft just like their counterpart, but they also broke at the femoral neck. In the case of SYN the artificial bones clearly show the more realistic fracture pattern, while their printed counterparts burst at the femoral head due to the thin cortex. Interestingly, the printed SAW show a more realistic fracture at the femoral neck compared to the artificial ones breaking at the shaft. In sum the printed bones break in a more expected, brittle, and “explosive” way than their artificial counterparts except for SYN. This is also a result of the printed bones containing more energy before fracture than artificial ones.

As shown in Figure 63 the printed femurs, withstand more load than the artificial ones. Only SAW samples endured lower load (7405.9 ± 132.9 N) than the purchased

bone (9119.3 N). This may be the result of the composite material outperforming the printed bones which are solely comprised of PLA. OBS_P show an average ultimate force of 5446.8 ± 928.4 N before fracturing as opposed to OBS_K with 1403.2 ± 112.4 N, which is almost four times lower. Also, the geometrical equal OB_P endured more than twice as much force than the artificial counterpart (OB_P: 6230.6 ± 586.7 N; OB_K: 2470.3 ± 268.5 N). With SYN having the same infill density (12%) and almost the same mechanically performing foam as OB, the printed bones performed significantly better with an average ultimate force of 7137.9 ± 1521.5 N compared to the SYN_K 3144.3 ± 174.3 N. This is twice as much load before fracturing than the artificial one could endure.

Dall'Ara *et al.* already found out in their previous study that a human femur could withstand forces between 8710 ± 2930 N in stance configuration before breaking³¹. Compared with the artificial bones only SAWBONE[®] could reach this load benchmark. The upper limit of our printed bones is 8662.4 N, which makes them comparable to the average value of natural bone.

Dall'Ara *et al.* also defined the stiffness of natural human femur with an value of 6280 ± 1940 N/mm³¹. Compared with the artificial bones, not even SAWBONE[®] could keep up by having a stiffness of 3127.5 N/mm. The other purchased femurs showed only a stiffness between 307-996 N/mm, which is way below the natural bones. All the printed bones show a stiffness of 1204-1920 N/mm (Figure 64) also not comparable to natural bone, but higher than the PU based artificial bones. Literature also reports values of 757 N/mm¹², 1070 N/mm (rehydrated bone)¹⁰ and 1360 N/mm (fresh frozen)¹⁰, which are comparable to artificial bone stiffness as well as printed samples stiffness. The deviation from literature is due to different sample preparation and differently chosen angles to represent the stance position. Furthermore, the samples of Cristofolini and Vicenconti *et al.* were fresh frozen human tissue and rehydrated one¹⁰. In the case of Papini *et al.* the donors were all around 75 years of age¹² and it is not known which age group and bone condition the artificial bones should resemble.

As shown in Figure 64 all printed samples outperformed their artificial counterpart except for the composite bone (SAWBONE®). It has a higher stiffness of 3127.5 N/mm compared with the one of SAW_P (1920.1 ± 137.3 N/mm). In the case of SYN (Figure 64 pink) the printed bones have a stiffness of 1800.1 ± 231.9 N/mm, which is higher than not only the artificial counterpart (SYN_K: 635.3 ± 12.8 N/mm) close to the printed SAW samples. Concerning the OB samples (Figure 64 blue), the printed bones reached an average stiffness of 1422.3 ± 272.1 N/mm, which is approximately 500 N/mm higher than the one of the artificial bones (996.6 ± 145.5 N/mm). The printed samples of the OBS have four times higher stiffness than their artificial counterpart (OBS_P: 1204 ± 338.5 N/mm, OBS_K: 306.8 ± 65.6 N/mm).

9 Conclusion

This master thesis shows that printed bones could keep up with already available synthetic surrogates for human femur concerning their mechanical behaviour. As expected, only the composite bone performed better than PLA printed bones, but with adjustments of geometric, material and the printing parameter, the mechanical behaviour of SAWBONE® should be reachable.

With respect to the variations of the mechanical test results, the embedding process and/or load introduction could be improved. Furthermore, the variation of the material parameters due to the printing process should be studied and reduced.

Research concerning patient specific printed bones could be of interest. The bones would be designed in a way that the resemble the characteristics of their bone condition by changing the infill density. This would open the possibility of patient-specific pre-operative studies, for example on implant systems.

To conclude this master thesis, it can be stated that printed bones seem to be a good alternative to already purchasable artificial bones. Not only because they could endure more load, have a greater stiffness but also the production cost would be cheaper.

References

1. Cheung, G.; Zalzal, P.; Bhandari, M.; Spelt, J. K.; Papini, M., Finite element analysis of a femoral retrograde intramedullary nail subject to gait loading. *Medical Engineering & Physics* **2004**, *26* (2), 93-108.
2. Talbot, M.; Zdero, R.; Garneau, D.; Cole, P. A.; Schemitsch, E. H., Fixation of long bone segmental defects: A biomechanical study. *Injury* **2008**, *39* (2), 181-186.
3. Bougherara, H.; Zdero, R.; Miric, M.; Shah, S.; Hardisty, M.; Zalzal, P.; Schemitsch, E. H., The biomechanics of the T2 femoral nailing system: A comparison of synthetic femurs with finite element analysis. *Proceedings of the Institution of Mechanical Engineers, Part H: Journal of Engineering in Medicine* **2009**, *223* (3), 303-314.
4. Davis, E. T.; Olsen, M.; Zdero, R.; Papini, M.; Waddell, J. P.; Schemitsch, E. H., A Biomechanical and Finite Element Analysis of Femoral Neck Notching During Hip Resurfacing. *Journal of Biomechanical Engineering* **2009**, *131* (4).
5. Davis, E. T.; Olsen, M.; Zdero, R.; Waddell, J. P.; Schemitsch, E. H., Femoral neck fracture following hip resurfacing: the effect of alignment of the femoral component. *The Journal of bone and joint surgery. British volume* **2008**, *90* (11), 1522-7.
6. Dennis, M. G.; Simon, J. A.; Kummer, F. J.; Koval, K. J.; DiCesare, P. E., Fixation of periprosthetic femoral shaft fractures occurring at the tip of the stem: A biomechanical study of 5 techniques. *The Journal of Arthroplasty* **2000**, *15* (4), 523-528.
7. Stevens, S. S.; Irish, A. J.; Vachtsevanos, J. G.; Csongradi, J.; Beaupré, G. S., A biomechanical study of three wiring techniques for cerclage-plating. *Journal of orthopaedic trauma* **1995**, *9* (5), 381-7.
8. Zdero, R.; Walker, R.; Waddell, J. P.; Schemitsch, E. H., Biomechanical evaluation of periprosthetic femoral fracture fixation. *The Journal of bone and joint surgery. American volume* **2008**, *90* (5), 1068-77.
9. Cusick, R. P.; Lucas, G. L.; McQueen, D. A.; Graber, C. D., Construct stiffness of different fixation methods for supracondylar femoral fractures above total knee prostheses. *American journal of orthopedics (Belle Mead, N.J.)* **2000**, *29* (9), 695-9.
10. Cristofolini, L.; Viceconti, M.; Cappello, A.; Toni, A., Mechanical validation of whole bone composite femur models. *Journal of Biomechanics* **1996**, *29* (4), 525-535.
11. Heiner, A. D.; Brown, T. D., Structural properties of a new design of composite replicate femurs and tibias. *Journal of Biomechanics* **2001**, *34* (6), 773-781.
12. Papini, M.; Zdero, R.; Schemitsch, E. H.; Zalzal, P., The Biomechanics of Human Femurs in Axial and Torsional Loading: Comparison of Finite Element Analysis, Human Cadaveric Femurs, and Synthetic Femurs. *Journal of Biomechanical Engineering* **2006**, *129* (1), 12-19.
13. Choudhari, C.; Patil, V., Product Development and its Comparative Analysis by SLA, SLS and FDM Rapid Prototyping Processes. *IOP Conference Series: Materials Science and Engineering* **2016**, *149*, 012009.
14. Streicher, J.; Pretterklieber, M. L., Waldeyer - Anatomie des Menschen. In *4 Bewegungsapparat. 4.1 Allgemeine Knochen-, Gelenk- und Muskellehre–4.3 Membrum superius, obere Extremität*, Anton, W.; Friedrich, A.; Franz, P.; Johannes, S., Eds. De Gruyter: 2012; pp 95-295.
15. Buenzli, P. R.; Sims, N. A., Quantifying the osteocyte network in the human skeleton. *Bone* **2015**, *75*, 144-150.
16. Platzer, W.; Shiozawa, T., *Taschenatlas Anatomie, Band 1: Bewegungsapparat*. 2018.
17. Meyers, M. A.; Chen, P.-Y.; Lin, A. Y.-M.; Seki, Y., Biological materials: Structure and mechanical properties. *Progress in Materials Science* **2008**, *53* (1), 1-206.

18. Hildebrand, T.; Laib, A.; Müller, R.; Dequeker, J.; Rügsegger, P., Direct Three-Dimensional Morphometric Analysis of Human Cancellous Bone: Microstructural Data from Spine, Femur, Iliac Crest, and Calcaneus. *Journal of Bone and Mineral Research* **1999**, *14* (7), 1167-1174.
19. Elke, R. P. E.; Cheal, E. J.; Simmons, C.; Poss, R., Three-dimensional anatomy of the cancellous structures within the proximal femur from computed tomography data. *Journal of Orthopaedic Research* **1995**, *13* (4), 513-523.
20. Stiehl, J. B.; Jacobson, D.; Carrera, G., Morphological analysis of the proximal femur using quantitative computed tomography. *Int Orthop* **2007**, *31* (3), 287-292.
21. Cui, W. Q.; Won, Y. Y.; Baek, M. H.; Lee, D. H.; Chung, Y. S.; Hur, J. H.; Ma, Y. Z., Age- and region-dependent changes in three-dimensional microstructural properties of proximal femoral trabeculae. *Osteoporosis international : a journal established as result of cooperation between the European Foundation for Osteoporosis and the National Osteoporosis Foundation of the USA* **2008**, *19* (11), 1579-87.
22. von Meyer, G. H., The classic: The architecture of the trabecular bone (tenth contribution on the mechanics of the human skeletal framework). *Clinical orthopaedics and related research* **2011**, *469* (11), 3079-3084.
23. Skedros, J. G.; Brand, R. A., Biographical sketch: Georg Hermann von Meyer (1815-1892). *Clinical orthopaedics and related research* **2011**, *469* (11), 3072-6.
24. Wolff, J., Ueber die innere Architectur der Knochen und ihre Bedeutung für die Frage vom Knochenwachstum. *Archiv für pathologische Anatomie und Physiologie und für klinische Medicin* **1870**, *50* (3), 389-450.
25. Martens, M.; Van Audekercke, R.; Delpont, P.; De Meester, P.; Mulier, J. C., The mechanical characteristics of cancellous bone at the upper femoral region. *Journal of Biomechanics* **1983**, *16* (12), 971-983.
26. Luo, C.-F., Reference axes for reconstruction of the knee. *The Knee* **2004**, *11* (4), 251-257.
27. Cherian, J. J.; Kapadia, B. H.; Banerjee, S.; Jauregui, J. J.; Issa, K.; Mont, M. A., Mechanical, Anatomical, and Kinematic Axis in TKA: Concepts and Practical Applications. *Curr Rev Musculoskelet Med* **2014**, *7* (2), 89-95.
28. Karuppall, R., Kinematic alignment in total knee arthroplasty: Does it really matter? *Journal of Orthopaedics* **2016**, *13* (4), A1-A3.
29. Bergmann, G.; Bender, A.; Dymke, J.; Duda, G.; Damm, P., Standardized Loads Acting in Hip Implants. *PLOS ONE* **2016**, *11* (5), e0155612.
30. Bergmann, G.; Deuretzbacher, G.; Heller, M.; Graichen, F.; Rohlmann, A.; Strauss, J.; Duda, G. N., Hip contact forces and gait patterns from routine activities. *Journal of Biomechanics* **2001**, *34* (7), 859-871.
31. Dall'Ara, E.; Luisier, B.; Schmidt, R.; Kainberger, F.; Zysset, P.; Pahr, D., A nonlinear QCT-based finite element model validation study for the human femur tested in two configurations in vitro. *Bone* **2013**, *52* (1), 27-38.
32. Dall'Ara, E.; Luisier, B.; Schmidt, R.; Pretterklieber, M.; Kainberger, F.; Zysset, P.; Pahr, D., DXA predictions of human femoral mechanical properties depend on the load configuration. *Medical Engineering & Physics* **2013**, *35* (11), 1564-1572.
33. Bousson, V.; Le Le Bras, A.; Roqueplan, F.; Kang, Y.; Mitton, D.; Kolta, S.; Bergot, C.; Skalli, W.; Vicaut, E.; Kalender, W.; Engelke, K.; Laredo, J. D., Volumetric quantitative computed tomography of the proximal femur: relationships linking geometric and densitometric variables to bone strength. Role for compact bone. *Osteoporosis International* **2006**, *17* (6), 855-864.
34. Cody, D. D.; Gross, G. J.; J. Hou, F.; Spencer, H. J.; Goldstein, S. A.; P. Fyhrie, D., Femoral strength is better predicted by finite element models than QCT and DXA. *Journal of Biomechanics* **1999**, *32* (10), 1013-1020.

35. Holzer, G.; von Skrbensky, G.; Holzer, L. A.; Pichl, W., Hip Fractures and the Contribution of Cortical Versus Trabecular Bone to Femoral Neck Strength. *Journal of Bone and Mineral Research* **2009**, *24* (3), 468-474.
36. Kukla, C.; Gaebler, C.; Pichl, R. W.; Prokesch, R.; Heinze, G.; Heinz, T., Predictive geometric factors in a standardized model of femoral neck fracture: Experimental study of cadaveric human femurs. *Injury* **2002**, *33* (5), 427-433.
37. Link, T. M.; Vieth, V.; Langenberg, R.; Meier, N.; Lotter, A.; Newitt, D.; Majumdar, S., Structure Analysis of High Resolution Magnetic Resonance Imaging of the Proximal Femur: In Vitro Correlation with Biomechanical Strength and BMD. *Calcified Tissue International* **2003**, *72* (2), 156-165.
38. Lochmüller, E. M.; Miller, P.; Bürklein, D.; Wehr, U.; Rambeck, W.; Eckstein, F., In Situ Femoral Dual-Energy X-ray Absorptiometry Related to Ash Weight, Bone Size and Density, and its Relationship with Mechanical Failure Loads of the Proximal Femur. *Osteoporosis International* **2000**, *11* (4), 361-367.
39. Bouxsein, M. L.; Coan, B. S.; Lee, S. C., Prediction of the strength of the elderly proximal femur by bone mineral density and quantitative ultrasound measurements of the heel and tibia. *Bone* **1999**, *25* (1), 49-54.
40. Cheng, X. G.; Nicholson, P. H. F.; Boonen, S.; Brys, P.; Lowet, G.; Nijs, J.; Dequeker, J., Effects of anteversion on femoral bone mineral density and geometry measured by dual energy X-ray absorptiometry: A cadaver study. *Bone* **1997**, *21* (1), 113-117.
41. Dragomir-Daescu, D.; Op Den Buijs, J.; McEligot, S.; Dai, Y.; Entwistle, R. C.; Salas, C.; Melton, L. J.; Bennet, K. E.; Khosla, S.; Amin, S., Robust QCT/FEA Models of Proximal Femur Stiffness and Fracture Load During a Sideways Fall on the Hip. *Annals of Biomedical Engineering* **2011**, *39* (2), 742-755.
42. Hansen, S.; Jensen, J.-E. B.; Ahrberg, F.; Hauge, E. M.; Brixen, K., The Combination of Structural Parameters and Areal Bone Mineral Density Improves Relation to Proximal Femur Strength: An In Vitro Study with High-Resolution Peripheral Quantitative Computed Tomography. *Calcified Tissue International* **2011**, *89* (4), 335.
43. Le Corroller, T.; Halgrin, J.; Pithioux, M.; Guenoun, D.; Chabrand, P.; Champsaur, P., Combination of texture analysis and bone mineral density improves the prediction of fracture load in human femurs. *Osteoporosis International* **2012**, *23* (1), 163-169.
44. Manske, S. L.; Liu-Ambrose, T.; Cooper, D. M. L.; Kontulainen, S.; Guy, P.; Forster, B. B.; McKay, H. A., Cortical and trabecular bone in the femoral neck both contribute to proximal femur failure load prediction. *Osteoporosis International* **2009**, *20* (3), 445-453.
45. Greenspan, S. L.; Myers, E. R.; Kiel, D. P.; Parker, R. A.; Hayes, W. C.; Resnick, N. M., Fall Direction, Bone Mineral Density, and Function: Risk Factors for Hip Fracture in Frail Nursing Home Elderly. *The American Journal of Medicine* **1998**, *104* (6), 539-545.
46. Kannus, P.; Leiponen, P.; Parkkari, J.; Palvanen, M.; Järvinen, M., A sideways fall and hip fracture. *Bone* **2006**, *39* (2), 383-384.
47. Schwartz, A. V.; Kelsey, J. L.; Sidney, S.; Grisso, J. A., Characteristics of Falls and Risk of Hip Fracture in Elderly Men. *Osteoporosis International* **1998**, *8* (3), 240-246.
48. Parkkari, J.; Kannus, P.; Palvanen, M.; Natri, A.; Vainio, J.; Aho, H.; Vuori, I.; Järvinen, M., Majority of Hip Fractures Occur as a Result of a Fall and Impact on the Greater Trochanter of the Femur: A Prospective Controlled Hip Fracture Study with 206 Consecutive Patients. *Calcified Tissue International* **1999**, *65* (3), 183-187.
49. Weigel, B.; Nerlich, M. L., *Praxisbuch Unfallchirurgie*. Springer-Verlag: 2011.
50. Fox, K. M.; Magaziner, J.; Hebel, J. R.; Kenzora, J. E.; Kashner, T. M., Intertrochanteric versus femoral neck hip fractures: differential characteristics, treatment, and sequelae. *The journals of gerontology. Series A, Biological sciences and medical sciences* **1999**, *54* (12), M635-40.

51. Vogl, W.; Mitchell, A. W.; Tibbitts, R.; Richardson, P., Grays Anatomie für Studenten. Elsevier GmbH, München: 2005.
52. Dimitriou, D.; Tsai, T.-Y.; Yue, B.; Rubash, H.; Kwon, Y. M.; Li, G., Side-to-side variation in normal femoral morphology: 3D CT analysis of 122 femurs. *Orthopaedics & Traumatology: Surgery & Research* **2016**, 102.
53. Shah, S.; Kim, S. Y.; Dubov, A.; Schemitsch, E. H.; Bougherara, H.; Zdero, R., The biomechanics of plate fixation of periprosthetic femoral fractures near the tip of a total hip implant: cables, screws, or both? *Proceedings of the Institution of Mechanical Engineers. Part H, Journal of engineering in medicine* **2011**, 225 (9), 845-56.
54. Grant, J. A.; Bishop, N. E.; Götzen, N.; Sprecher, C.; Honl, M.; Morlock, M. M., Artificial composite bone as a model of human trabecular bone: The implant–bone interface. *Journal of Biomechanics* **2007**, 40 (5), 1158-1164.
55. Zdero, R.; Elfallah, K.; Olsen, M.; Schemitsch, E. H., Cortical Screw Purchase in Synthetic and Human Femurs. *Journal of Biomechanical Engineering* **2009**, 131 (9).
56. Heiner, A. D., Structural properties of fourth-generation composite femurs and tibias. *Journal of Biomechanics* **2008**, 41 (15), 3282-3284.
57. Chong, A. C. M.; Miller, F.; Buxton, M.; Friis, E. A., Fracture Toughness and Fatigue Crack Propagation Rate of Short Fiber Reinforced Epoxy Composites for Analogue Cortical Bone. *Journal of Biomechanical Engineering* **2007**, 129 (4), 487-493.
58. Chong, A. C. M.; Friis, E. A.; Ballard, G. P.; Czuwala, P. J.; Cooke, F. W., Fatigue Performance of Composite Analogue Femur Constructs under High Activity Loading. *Annals of Biomedical Engineering* **2007**, 35 (7), 1196-1205.
59. Gardner, M. P.; Chong, A. C. M.; Pollock, A. G.; Wooley, P. H., Mechanical Evaluation of Large-Size Fourth-Generation Composite Femur and Tibia Models. *Annals of Biomedical Engineering* **2010**, 38 (3), 613-620.
60. Hein, T. J.; Hotchkiss, R.; Perissinotto, A.; Chao, E. Y., Analysis of bone model material for external fracture fixation experiments. *Biomedical sciences instrumentation* **1987**, 23, 43-8.
61. Szivek, J. A.; Thomas, M.; Benjamin, J. B., Technical note. Characterization of a synthetic foam as a model for human cancellous bone. *Journal of Applied Biomaterials* **1993**, 4 (3), 269-272.
62. Szivek, J. A.; Thompson, J. D.; Benjamin, J. B., Characterization of three formulations of a synthetic foam as models for a range of human cancellous bone types. *Journal of applied biomaterials : an official journal of the Society for Biomaterials* **1995**, 6 (2), 125-8.
63. Thompson, M. S.; McCarthy, I. D.; Lidgren, L.; Ryd, L., Compressive and Shear Properties of Commercially Available Polyurethane Foams. *Journal of Biomechanical Engineering* **2003**, 125 (5), 732-734.
64. Patel, P. S. D.; Shepherd, D. E. T.; Hukins, D. W. L., Compressive properties of commercially available polyurethane foams as mechanical models for osteoporotic human cancellous bone. *BMC Musculoskeletal Disorders* **2008**, 9 (1), 137.
65. Carew, R. M.; Morgan, R. M.; Rando, C., A Preliminary Investigation into the Accuracy of 3D Modeling and 3D Printing in Forensic Anthropology Evidence Reconstruction. *Journal of Forensic Sciences* **2019**, 64 (2), 342-352.
66. Bartikian, M.; Ferreira, A.; Gonçalves-Ferreira, A.; Neto, L. L., 3D printing anatomical models of head bones. *Surgical and Radiologic Anatomy* **2019**, 41 (10), 1205-1209.
67. O'Reilly, M. K.; Reese, S.; Herlihy, T.; Geoghegan, T.; Cantwell, C. P.; Feeney, R. N. M.; Jones, J. F. X., Fabrication and assessment of 3D printed anatomical models of the lower limb for anatomical teaching and femoral vessel access training in medicine. *Anatomical Sciences Education* **2016**, 9 (1), 71-79.
68. AbouHashem, Y.; Dayal, M.; Savanah, S.; Štrkalj, G., The application of 3D printing in anatomy education. *Medical education online* **2015**, 20 (1), 29847.

69. Biebrich, K.-M. The mechanical behavior of simple and advanced FDM printed models of human femora. Wien, 2021.
70. Zdero, R.; Shah, S.; Mosli, M.; Schemitsch, E. H., The effect of load application rate on the biomechanics of synthetic femurs. *Proceedings of the Institution of Mechanical Engineers, Part H: Journal of Engineering in Medicine* **2009**, 224 (4), 599-605.
71. Tsuji, M.; Crookshank, M.; Olsen, M.; Schemitsch, E. H.; Zdero, R., The biomechanical effect of artificial and human bone density on stopping and stripping torque during screw insertion. *Journal of the Mechanical Behavior of Biomedical Materials* **2013**, 22, 146-156.
72. Zdero, R.; Olsen, M.; Bougherara, H.; Schemitsch, E. H., Cancellous bone screw purchase: A comparison of synthetic femurs, human femurs, and finite element analysis. *Proceedings of the Institution of Mechanical Engineers, Part H: Journal of Engineering in Medicine* **2008**, 222 (8), 1175-1183.
73. Gebhardt, A., *Generative Fertigungsverfahren : Additive Manufacturing und 3D Drucken für Prototyping, Tooling, Produktion*. 4., neu bearb. und erw. Aufl.. ed.; München : Hanser: München, 2013; p XXIV, 637 S., zahlr. Ill., graph. Darst.
74. Standard, A., F2792-12a. *Standard terminology for additive manufacturing technologies ASTM International, West Conshohocken* **2012**.
75. Thompson, A.; McNally, D.; Maskery, I.; Leach, R. K., X-ray computed tomography and additive manufacturing in medicine: a review. *International Journal of Metrology and Quality Engineering* **2017**, 8, 17.
76. Igami, T.; Nakamura, Y.; Hirose, T.; Ebata, T.; Yokoyama, Y.; Sugawara, G.; Mizuno, T.; Mori, K.; Nagino, M., Application of a Three-dimensional Print of a Liver in Hepatectomy for Small Tumors Invisible by Intraoperative Ultrasonography: Preliminary Experience. *World Journal of Surgery* **2014**, 38 (12), 3163-3166.
77. Huang, H.; Hsieh, M.-F.; Zhang, G.; Ouyang, H.; Zeng, C.; Yan, B.; Xu, J.; Yang, Y.; Wu, Z.; Huang, W., Improved accuracy of 3D-printed navigational template during complicated tibial plateau fracture surgery. *Australasian Physical & Engineering Sciences in Medicine* **2015**, 38 (1), 109-117.
78. Takemoto, M.; Fujibayashi, S.; Ota, E.; Otsuki, B.; Kimura, H.; Sakamoto, T.; Kawai, T.; Futami, T.; Sasaki, K.; Matsushita, T.; Nakamura, T.; Neo, M.; Matsuda, S., Additive-manufactured patient-specific titanium templates for thoracic pedicle screw placement: novel design with reduced contact area. *European Spine Journal* **2016**, 25 (6), 1698-1705.
79. Kenngott, H. G.; Wünscher, J. J.; Wagner, M.; Preukschas, A.; Wekerle, A. L.; Neher, P.; Suwelack, S.; Speidel, S.; Nickel, F.; Oladokun, D.; Maier-Hein, L.; Dillmann, R.; Meinzer, H. P.; Müller-Stich, B. P., OpenHELP (Heidelberg laparoscopy phantom): development of an open-source surgical evaluation and training tool. *Surgical Endoscopy* **2015**, 29 (11), 3338-3347.
80. Gopakumar, S., RP in medicine: a case study in cranial reconstructive surgery. *Rapid Prototyping Journal* **2004**.
81. Winder, J.; Bibb, R., Medical Rapid Prototyping Technologies: State of the Art and Current Limitations for Application in Oral and Maxillofacial Surgery. *Journal of Oral and Maxillofacial Surgery* **2005**, 63 (7), 1006-1015.
82. Kumar, S., *Additive Manufacturing Processes*. 1st ed. 2020. ed.; Cham : Springer International Publishing : Imprint: Springer: Cham, 2020; p 1 Online-Ressource (XIII, 205 Seiten), 95 Illustrationen, 62 Illustrationen.
83. Bibb, R.; Sias, G., Bone structure models using stereolithography: a technical note. *Rapid Prototyping Journal* **2002**.
84. Petzold, R.; Zeilhofer, H. F.; Kalender, W. A., Rapid prototyping technology in medicine—basics and applications. *Computerized Medical Imaging and Graphics* **1999**, 23 (5), 277-284.

85. Raut, S.; Jatti, V. S.; Khedkar, N. K.; Singh, T. P., Investigation of the Effect of Built Orientation on Mechanical Properties and Total Cost of FDM Parts. *Procedia Materials Science* **2014**, *6*, 1625-1630.
86. Warnung, L.; Estermann, S.-J.; Reisinger, A., Mechanical Properties of Fused Deposition Modeling (FDM) 3D Printing Materials. *RTEjournal - Fachforum für Rapid Technologien* **2018**, *2018* (1).
87. Griffiths, C. A.; Howarth, J.; Rowbotham, G. d.-A.; Rees, A., Effect of Build Parameters on Processing Efficiency and Material Performance in Fused Deposition Modelling. *Procedia CIRP* **2016**, *49*, 28-32.
88. Hutmacher, D. W.; Schantz, T.; Zein, I.; Ng, K. W.; Teoh, S. H.; Tan, K. C., Mechanical properties and cell cultural response of polycaprolactone scaffolds designed and fabricated via fused deposition modeling. *Journal of Biomedical Materials Research* **2001**, *55* (2), 203-216.
89. van Uden, S.; Silva-Correia, J.; Correlo, V. M.; Oliveira, J. M.; Reis, R. L., Custom-tailored tissue engineered polycaprolactone scaffolds for total disc replacement. *Biofabrication* **2015**, *7* (1), 015008.
90. Xu, N.; Ye, X.; Wei, D.; Zhong, J.; Chen, Y.; Xu, G.; He, D., 3D Artificial Bones for Bone Repair Prepared by Computed Tomography-Guided Fused Deposition Modeling for Bone Repair. *ACS Applied Materials & Interfaces* **2014**, *6* (17), 14952-14963.
91. Swetham, T.; Reddy, K. M. M.; Huggi, A.; Kumar, M., A Critical Review on of 3D Printing Materials and Details of Materials used in FDM. *Int J Sci Res Sci Eng* **2017**, *3* (2), 353-361.
92. Kaiser, W., *Kunststoffchemie für Ingenieure : von der Synthese bis zur Anwendung*. 3. Aufl. ed.; München : Hanser: München, 2011; p XXXII, 575 S., Ill., graph. Darst, 25 cm.
93. Rodríguez-Panes, A.; Claver, J.; Camacho, A. M., The Influence of Manufacturing Parameters on the Mechanical Behaviour of PLA and ABS Pieces Manufactured by FDM: A Comparative Analysis. *Materials* **2018**, *11* (8), 1333.
94. Mercado-Colmenero, J. M.; La Rubia, M. D.; Mata-Garcia, E.; Rodriguez-Santiago, M.; Martin-Doñate, C., Experimental and Numerical Analysis for the Mechanical Characterization of PETG Polymers Manufactured with FDM Technology under Pure Uniaxial Compression Stress States for Architectural Applications. *Polymers* **2020**, *12* (10), 2202.
95. Salzer, R., *Biomedical Imaging: Principles and Applications*. 1. Aufl. 1 ed.; Hoboken: Wiley: Hoboken, 2012.
96. Friess, M., Scratching the Surface? The use of surface scanning in physical and paleoanthropology. *Journal of anthropological sciences = Rivista di antropologia : JASS* **2012**, *90*, 7-31.
97. Orhan, K., *Micro-computed Tomography (micro-CT) in Medicine and Engineering*. 2020.
98. Mankovich, N. J.; Cheeseman, A. M.; Stoker, N. G., The display of three-dimensional anatomy with stereolithographic models. *Journal of Digital Imaging* **1990**, *3* (3), 200.
99. Fahrni, S.; Campana, L.; Dominguez, A.; Uldin, T.; Dedout, F.; Delémont, O.; Grabherr, S., CT-scan vs. 3D surface scanning of a skull: first considerations regarding reproducibility issues. *Forensic Sci Res* **2017**, *2* (2), 93-99.
100. Telfer, S.; Woodburn, J., The use of 3D surface scanning for the measurement and assessment of the human foot. *Journal of Foot and Ankle Research* **2010**, *3* (1), 19.
101. Thomas, D. B.; Hiscox, J. D.; Dixon, B. J.; Potgieter, J., 3D scanning and printing skeletal tissues for anatomy education. *Journal of Anatomy* **2016**, *229* (3), 473-481.
102. Katharina, N., Compression Test of 3D printed Cubes varying in Infill density. **2020**.
103. Switzerland, A. F., AO/OTA Fracture and Dislocation Classification: Long bone fractures. **2018**.

104. Brzobohatá, H.; Prokop, J.; Horák, M.; Jancárek, A.; Velemínská, J., Accuracy and benefits of 3D bone surface modelling: a comparison of two methods of surface data acquisition reconstructed by laser scanning and computed tomography outputs. *Collegium antropologicum* **2012**, 36 (3), 801-6.
105. Nicayenzi, B.; Shah, S.; Schemitsch, E. H.; Bougherara, H.; Zdero, R., The biomechanical effect of changes in cancellous bone density on synthetic femur behaviour. *Proceedings of the Institution of Mechanical Engineers, Part H: Journal of Engineering in Medicine* **2011**, 225 (11), 1050-1060.
106. Zdero, R.; Bougherara, H.; Dubov, A.; Shah, S.; Zalzal, P.; Mahfud, A.; Schemitsch, E. H., The effect of cortex thickness on intact femur biomechanics: a comparison of finite element analysis with synthetic femurs. *Proceedings of the Institution of Mechanical Engineers. Part H, Journal of engineering in medicine* **2010**, 224 (7), 831-40.
107. Zdero, R.; Shah, S.; Mosli, M.; Schemitsch, E. H., The effect of load application rate on the biomechanics of synthetic femurs. *Proceedings of the Institution of Mechanical Engineers, Part H: Journal of Engineering in Medicine* **2010**, 224 (4), 599-605.
108. Wu, S.-C.; Rau, C.-S.; Kuo, S. C. H.; Chien, P.-C.; Hsieh, C.-H., The influence of ageing on the incidence and site of trauma femoral fractures: a cross-sectional analysis. *BMC Musculoskeletal Disorders* **2019**, 20 (1), 413.

Appendix

μ-CT measurements:

```
[System]
Scanner=SkyScan1173
Instrument S/N=16N05067
Hardware version=A
Software=Version 1. 6 (build 24)
Home directory=C:\Skyscan
Source Type=Hamamatsu 130/300
Camera=FlatPanel Sensor
Camera Pixel Size (um)=50.0
CameraXYRatio=1.0000
Incl.in lifting (um/mm)=-0.2710
[Acquisition]
Data directory=D:\SCAN\00315
Filename Prefix=Arti_Bone
Number of Files= 900
Source Voltage (kV)= 65
Source Current (uA)= 75
Number of Rows= 2240
Number of Columns= 4224
Image crop origin X= 0
Image crop origin Y=0
Camera binning=1x1
Image Rotation=0.0100
Gantry direction=CC
Number of connected scans=3
Number of lines to be reconstructed=1415
Image Pixel Size (um)=35.329911
Scaled Image Pixel Size (um)=35.329911
Object to Source (mm)=256.924
Camera to Source (mm)=364.000
Vertical Object Position (mm)=15.450
Optical Axis (line)=1105
Filter=No Filter
Image Format=TIF
Depth (bits)=16
Screen LUT=0
Exposure (ms)= 650
Rotation Step (deg)=0.400
Frame Averaging=ON (2)
Random Movement=OFF (8)
Use 360 Rotation=YES
Partial width=100
FF updating interval=451
Geometrical Correction=OFF
Camera Offset=ON
Median Filtering=OFF
Flat Field Correction=OFF
Rotation Direction=CC

Scanning Trajectory=ROUND
Type Of Motion=STEP AND SHOOT
Study Date and Time=Nov 19, 2020 11:08:17
Scan duration=01:00:28
Maximum vertical TS=5.0
[Reconstruction]
Reconstruction Program=NRecon
Program Version=Version: 1.7.4.6
Program Home Directory=C:\Skyscan
Reconstruction engine=GPUReconServer
Engine version=Version: 1.7.4
Reconstruction from batch=No
Postalignment Applied=1
Connected Reconstruction (parts)=3
Sub-scan post alignment [0]=-4.000000
Sub-scan post alignment [1]=-5.000000
Sub-scan post alignment [2]=-1.000000
Sub-scan scan length [0]=1415
Sub-scan scan length [1]=1184
Sub-scan scan length [2]=1184
Reconstruction servers= DESKTOP-8R3R8DL
Dataset Origin=SkyScan1173
Dataset Prefix=Arti_Bone-00
Dataset Directory=D:\SCAN\00315
Output Directory=D:\RECON\00315
Time and Date=19 Nov 2020 12h:59m:03s
First Section=308
Last Section=4699
Reconstruction duration per slice (seconds)=0.813953
Total reconstruction time (1505 slices) in seconds=1225.000000
Section to Section Step=1
Sections Count=4392
Result File Type=TIF
Result File Header Length (bytes)=12
Result Image Width (pixels)=3572
Result Image Height (pixels)=3572
Pixel Size (um)=35.32991
Reconstruction Angular Range (deg)=360.00
Use 180+=OFF
Angular Step (deg)=0.4000
Smoothing=4
Smoothing kernel=2 (Gaussian)
Ring Artifact Correction=15
Draw Scales=OFF
Object Bigger than FOV=OFF
Reconstruction from ROI=ON_ROUND
ROI Top (pixels)=3729
ROI Bottom (pixels)=157

ROI Left (pixels)=266
ROI Right (pixels)=3838
ROI reference length=4224
Filter cutoff relative to Nyquist frequency=100
Filter type=0
Filter type description=Hamming (Alpha=0.54)
Undersampling factor=1
Threshold for defect pixel mask (%)=0
Beam Hardening Correction (%)=25
CS Static Rotation (deg)=0.00
CS Static Rotation Total(deg)=0.00
Minimum for CS to Image Conversion=0.000000
Maximum for CS to Image Conversion=0.008768
HU Calibration=OFF
BMP LUT=0
Cone-beam Angle Horiz.(deg)=32.389084
Cone-beam Angle Vert.(deg)=17.510942
[File name convention]
Filename Index Length=4
Filename Prefix=Arti_Bone_rec
```

Figure 65: Measurement protocol OBS_1K

```

[System]
Scanner=SkyScan1173
Instrument S/N=16N05067
Hardware version=A
Software=Version 1. 6 (build 24)
Home directory=C:\Skyscan
Source Type=Hamamatsu 130/300
Camera=FlatPanel Sensor
Camera Pixel Size (um)=50.0
CameraXYRatio=1.0000
Incl.in lifting (um/mm)=-0.2710
[Acquisition]
Data directory=D:\SCAN\00327
Filename Prefix=synbone_2_v2
Number of Files= 600
Source Voltage (kV)= 65
Source Current (uA)= 75
Number of Rows= 1120
Number of Columns= 2112
Image crop origin X= 0
Image crop origin Y=0
Camera binning=2x2
Image Rotation=0.0100
Gantry direction=CC
Number of connected scans=3
Number of lines to be reconstructed=751
Image Pixel Size (um)=70.659821
Scaled Image Pixel Size (um)=70.659821
Object to Source (mm)=256.924
Camera to Source (mm)=364.000
Vertical Object Position (mm)=7.765
Optical Axis (line)= 552
Filter=No Filter
Image Format=TIFF
Depth (bits)=16
Screen LUT=0
Exposure (ms)= 250
Rotation Step (deg)=0.400
Frame Averaging=ON (2)
Random Movement=ON (8)
Use 360 Rotation=NO
Partial width=100
FF updating interval=0
Geometrical Correction=OFF
Camera Offset=ON
Median Filtering=OFF
Flat Field Correction=ON
Rotation Direction=CC

Scanning Trajectory=ROUND
Type Of Motion=STEP AND SHOOT
Study Date and Time=Jan 20, 2021 12:43:19
Scan duration=00:27:54
Maximum vertical TS=5.0
[Reconstruction]
Reconstruction Program=NRecon
Program Version=Version: 1.7.4.6
Program Home Directory=C:\Skyscan
Reconstruction engine=GPUReconServer
Engine version=Version: 1.7.4
Reconstruction from batch=No
Postalignment Applied=1
Connected Reconstruction (parts)=3
Sub-scan post alignment [0]=0.000000
Sub-scan post alignment [1]=-0.500000
Sub-scan post alignment [2]=0.500000
Sub-scan scan length [0]=751
Sub-scan scan length [1]=657
Sub-scan scan length [2]=657
Reconstruction servers= DESKTOP-8R3R8DL
Dataset Origin=SkyScan1173
Dataset Prefix=synbone_2_v2-00
Dataset Directory=D:\SCAN\00327
Output Directory=D:\RECON\00327
Time and Date=21 Jan 2021 13h:19m:30s
First Section=207
Last Section=2527
Reconstruction duration per slice (seconds)=0.267684
Total reconstruction time (721 slices) in seconds=193.000000
Section to Section Step=1
Sections Count=2321
Result File Type=TIF
Result File Header Length (bytes)=12
Result Image Width (pixels)=2020
Result Image Height (pixels)=2020
Pixel Size (um)=70.65982
Reconstruction Angular Range (deg)=240.00
Use 180=OFF
Angular Step (deg)=0.4000
Smoothing=0
Ring Artifact Correction=8
Draw Scales=OFF
Object Bigger than FOV=OFF
Reconstruction from ROI=ON_ROUND
ROI Top (pixels)=2053
ROI Bottom (pixels)=31
ROI Left (pixels)=34
ROI Right (pixels)=2056
ROI reference length=2112
Filter cutoff relative to Nyquist frequency=100
Filter type=0
Filter type description=Hamming (Alpha=0.54)
Undersampling factor=1
Threshold for defect pixel mask (%)=0
Beam Hardening Correction (%)=40
CS Static Rotation (deg)=0.00
CS Static Rotation Total(deg)=0.00
Minimum for CS to Image Conversion=0.000000
Maximum for CS to Image Conversion=0.007007
HU Calibration=OFF
BMP LUT=0
Cone-beam Angle Horiz.(deg)=32.389084
Cone-beam Angle Vert.(deg)=17.510942
[File name convention]
Filename Index Length=4
Filename Prefix=synbone_2_v2_rec
    
```

Figure 66: Measurement protocol SYN_1K

```

[System]
Scanner=SkyScan1173
Instrument S/N=16N05067
Hardware version=A
Software=Version 1. 6 (build 24)
Home directory=C:\Skyscan
Source Type=Hamamatsu 130/300
Camera=FlatPanel Sensor
Camera Pixel Size (um)=50.0
CameraXYRatio=1.0000
Incl.in lifting (um/mm)=-0.2710
[Acquisition]
Data directory=D:\SCAN\00328
Filename Prefix=sawbone_1
Number of Files= 600
Source Voltage (kV)= 65
Source Current (uA)= 75
Number of Rows= 1120
Number of Columns= 2112
Image crop origin X= 0
Image crop origin Y=0
Camera binning=2x2
Image Rotation=0.0100
Gantry direction=CC
Number of connected scans=3
Number of lines to be reconstructed=772
Image Pixel Size (um)=70.659821
Scaled Image Pixel Size (um)=70.659821
Object to Source (mm)=256.924
Camera to Source (mm)=364.000
Vertical Object Position (mm)=4.053
Optical Axis (line)= 552
Filter=No Filter
Image Format=TIFF
Depth (bits)=16
Screen LUT=0
Exposure (ms)= 250
Rotation Step (deg)=0.400
Frame Averaging=ON (2)
Random Movement=ON (8)
Use 360 Rotation=NO
Partial width=100
FF updating interval=0
Geometrical Correction=OFF
Camera Offset=ON
Median Filtering=OFF
Flat Field Correction=ON
Rotation Direction=CC

Scanning Trajectory=ROUND
Type Of Motion=STEP AND SHOOT
Study Date and Time=Jan 27, 2021 15:00:29
Scan duration=00:27:41
    
```

Figure 67: Measurement protocol SAW

Changes in g-codes of the printed bones compared to standard settings:

ORTHOBone Standard:

- ; external perimeters extrusion width = 0.60mm
- ; perimeters extrusion width = 0.60mm
- ; infill extrusion width = 0.45mm
- ; solid infill extrusion width = 0.60mm
- ; top infill extrusion width = 0.60mm
- ; support material extrusion width = 0.35mm

- ; first layer extrusion width = 0.42mm
- ; external perimeters extrusion width = 0.45mm
- ; perimeters extrusion width = 0.45mm
- ; infill extrusion width = 0.45mm
- ; solid infill extrusion width = 0.45mm
- ; top infill extrusion width = 0.40mm
- ; support material extrusion width = 0.35mm
- ; first layer extrusion width = 0.42mm

- ; filament used [mm] = 84762.4
- ; filament used [cm³] = 203.9
- ; filament used [g] = 252.8
- ; filament cost = 6.3
- ; total filament used [g] = 252.8
- ; total filament cost = 6.3
- ; estimated printing time (normal mode) = 19h 24m 21s
- ; estimated printing time (silent mode) = 19h 36m 38s

ORTHOBone:

- ; external perimeters extrusion width = 0.60mm
- ; perimeters extrusion width = 0.60mm
- ; infill extrusion width = 0.45mm
- ; solid infill extrusion width = 0.60mm
- ; top infill extrusion width = 0.60mm
- ; support material extrusion width = 0.35mm
- ; first layer extrusion width = 0.42mm

- ; external perimeters extrusion width = 0.45mm
- ; perimeters extrusion width = 0.45mm
- ; infill extrusion width = 0.45mm
- ; solid infill extrusion width = 0.45mm
- ; top infill extrusion width = 0.40mm
- ; support material extrusion width = 0.35mm
- ; first layer extrusion width = 0.42mm
- ; filament used [mm] = 87790.2
- ; filament used [cm³] = 211.2
- ; filament used [g] = 261.8
- ; filament cost = 6.5

- ; total filament used [g] = 261.8
- ; total filament cost = 6.5
- ; estimated printing time (normal mode) = 20h 20m 13s
- ; estimated printing time (silent mode) = 20h 32m 24s

SYNBONE:

- ; external perimeters extrusion width = 0.60mm
- ; perimeters extrusion width = 0.60mm
- ; infill extrusion width = 0.45mm
- ; solid infill extrusion width = 0.60mm
- ; top infill extrusion width = 0.60mm
- ; support material extrusion width = 0.35mm
- ; first layer extrusion width = 0.42mm

- ; external perimeters extrusion width = 0.45mm
- ; perimeters extrusion width = 0.45mm
- ; infill extrusion width = 0.45mm
- ; solid infill extrusion width = 0.45mm
- ; top infill extrusion width = 0.40mm
- ; support material extrusion width = 0.35mm
- ; first layer extrusion width = 0.42mm

- ; filament used [mm] = 88267.2
- ; filament used [cm³] = 212.3
- ; filament used [g] = 263.3
- ; filament cost = 6.6

- ; total filament used [g] = 263.3
- ; total filament cost = 6.6
- ; estimated printing time (normal mode) = 20h 45m 16s
- ; estimated printing time (silent mode) = 20h 57m 19s

SAWBONE:

- ; external perimeters extrusion width = 0.60mm
- ; perimeters extrusion width = 0.60mm
- ; infill extrusion width = 0.45mm
- ; solid infill extrusion width = 0.60mm
- ; top infill extrusion width = 0.60mm
- ; support material extrusion width = 0.35mm
- ; first layer extrusion width = 0.42mm

- ; external perimeters extrusion width = 0.45mm
- ; perimeters extrusion width = 0.45mm
- ; infill extrusion width = 0.45mm
- ; solid infill extrusion width = 0.45mm
- ; top infill extrusion width = 0.40mm
- ; support material extrusion width = 0.35mm
- ; first layer extrusion width = 0.42mm

- ; filament used [mm] = 84486.8
- ; filament used [cm³] = 203.2
- ; filament used [g] = 252.0
- ; filament cost = 6.3

- ; total filament used [g] = 252.0
- ; total filament cost = 6.3
- ; estimated printing time (normal mode) = 22h 17m 5s
- ; estimated printing time (silent mode) = 22h 29m 22s